United States Military Academy

Photonics Research Center

$$h(n_1, n_2) = \frac{f_c}{2\pi} \frac{J_1\left(f_c\sqrt{n_1^2 + n_2^2}\right)}{\sqrt{n_1^2 + n_2^2}}$$

$$w_\lambda(n_1, n_2) = \begin{cases} \dfrac{I_0\left[\alpha\sqrt{1 - \dfrac{n_1^2 + n_2^2}{M^2}}\right]}{I_0^2[\alpha]} & n_1^2 + n_2^2 \leq M^2 \\ 0 & \text{otherwise} \end{cases}$$

2000 Program Review

**Photonics Research Center
United States Military Academy
West Point, New York
10996**

20010222 043

REPORT DOCUMENTATION PAGE

Form Approved
OMB NO. 0704-0188

1. AGENCY USE ONLY (Leave Blank)	2. REPORT DATE 001218	3. REPORT TYPE AND DATES COVERED Technical Report (May 1998 - May 2000)

4. TITLE AND SUBTITLE
Photonics Research and Education at the United States Military Academy

5. FUNDING NUMBERS
MIPROFUSMAR037

6. AUTHOR(S)
MAJ Augustus W. Fountain III and LTC Barry L. Shoop

7. PERFORMING ORGANIZATION NAME(S) AND ADDRESS(ES)
Photonics Research Center
United States Military Academy
West Point, NY 10996

8. PERFORMING ORGANIZATION REPORT NUMBER
ARO Proposal 40156-PH

9. SPONSORING / MONITORING AGENCY NAME(S) AND ADDRESS(ES)

U. S. Army Research Office
P.O. Box 12211
Research Triangle Park, NC 27709-2211

10. SPONSORING / MONITORING AGENCY REPORT NUMBER

ARO 40156.1 -PH

11. SUPPLEMENTARY NOTES
The views, opinions and/or findings contained in this report are those of the author(s) and should not be construed as an official Department of the Army position, policy or decision, unless so designated by other documentation.

12 a. DISTRIBUTION / AVAILABILITY STATEMENT

Approved for public release; distribution unlimited.

12 b. DISTRIBUTION CODE

13. ABSTRACT (Maximum 200 words)

The Photonics Research Center was established at the United States Military Academy, in May of 1987 through a Memorandum of Understanding between the Superintendent of the United States Military Academy and the Vice Chief of Staff of the Army. The Center's three principle missions focus on education of both cadets and officers, the conduct of basic and applied research, and support to the Army and DoD in the area of lasers and photonics. The Center's proven record in producing world-class research has played a significant role in past Academy accreditation visits. Each year, educational programs associated with the Center introduce over 1000 cadets to a general familiarity with laser technology, provide over 50 cadets with an in-depth understanding of lasers and laser technology, and returns officers to the field Army who are now considered experts in developing and applying laser technologies. The Center is also approved by the National Research Council as a research site for their postdoctoral associateship program. The Center's faculty come from the Departments of Chemistry, Electrical Engineering and Computer Science, and Physics who conduct basic and applied research in the Center using laser technology.

20010222 043

14. SUBJECT TERMS Photonics, Spectroscopy, Error Diffusion, Non-linear Optics			**15. NUMBER OF PAGES** 96
			16. PRICE CODE

17. SECURITY CLASSIFICATION OR REPORT UNCLASSIFIED	18. SECURITY CLASSIFICATION ON THIS PAGE UNCLASSIFIED	19. SECURITY CLASSIFICATION OF ABSTRACT UNCLASSIFIED	20. LIMITATION OF ABSTRACT UL

The Photonics Research Center

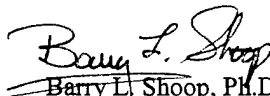## Bi-Annual Research Progress Review

1998 -- 2000

The Photonics Research Center was established in 1987 to fulfill three principal missions for the United States Army: educate future Army leaders, conduct basic research, and support the Army and Department of Defense, all in the area of lasers and photonics technologies. This report highlights the progress of the research and educational programs in the Photonics Research Center over the period of May 1998 through April 2000. This progress report is produced in partial fulfillment of a bi-annual program review conducted by the Army Research Office, the Center's major funding agency.

Over the past two-years, the Center has continued to grow and mature, making significant contributions to the academic curriculum, faculty professional growth and development, the Army, and the research community as a whole. Our research faculty continue to engage our cadets both in the classroom and in the laboratory. The Center continues to contribute to the educational development of Army leaders both at the entry-level and mid-career-level. The two-day short-course the Center supports at Ft. Leavenworth has become an integrated part of the Advanced Warfighting curriculum, impacting over 160 mid-career officers each year. Several military and civilian faculty promotions to Associate Professor and Professor have been supported in part by research conducted in the Center. Our researchers continue to have strong collaborative ties with the Army Research Laboratory as well as other Army agencies and program managers. The research projects that our faculties are engaged -in continue to be leading-edge research, receiving many invitations for invited and plenary presentations and papers. During this period our researchers have significantly increased the level project-specific funding which is a tribute to our researchers and an indication of the quality of the research. Our researchers are also very active in the leadership of both local and national level professional societies.

During this period, we have made substantial improvements to the infrastructure of the Center including the administration and cadet study areas, the instructional laboratories, and the research laboratory. In the summer of 1999, the carpet throughout the entire administration area was replaced and we moved the cadet study area into a new room adjacent to the Center's administration area. This allowed for the development of a library area adjoining the conference room. The conference room has been upgraded to include a multi-media projection and sound system to support cadet presentations, research colloquia, and meetings. In the Spring of 1999, we established a new laser instructional laboratory which will provide access to a wide-range of different types of lasers. Also in 1999, USMA provided over $125k for the upgrade of both instructional labs including water, power, and new non-skid floors. The research laboratory upgrade included the installation of an uninterrupted power supply (UPS) to protect all of the laser water chillers as well as some of the sensitive electronic measurement equipment used on our experiments.

This two-year period also marks several firsts for the Center. This year we will have our first researcher elected to the grade of Fellow and we will have our first patent, both indicators of a healthy and mature research program. One of our cadets received the Phi Kappa Phi Scholastic Achievement Award and another received the Mid-Hudson American Chemical Society Research Award, additional indicators of the quality of our program.

The research accomplishments highlighted in this report represent the products of a healthy, mature research organization. They are the result of and a tribute to those extremely talented researchers and cadets who conduct the day-to-day research and education on which the Center's reputation has been built.

Barry L. Shoop, Ph.D.
Lieutenant Colonel, Signal Corps
Director

The cover photograph shows the Photonic A/D Converter and Smart Pixel experiment with Cadet Michael J. Sullivan Jr. (left), LTC Barry L. Shoop (center), and Cadet Zachariah G. Morford (right). Both Cadet Sullivan and Cadet Morford are USMA Class of 2000.

THE PHOTONICS RESEARCH CENTER

The Photonics Research Center was established at the United States Military Academy, West Point, New York in May of 1987 through a Memorandum of Understanding between the Superintendent of the United States Military Academy and the Vice Chief of Staff of the Army. An excerpt from this memorandum provides some insight into the charter of the Center:

"As the Army modernizes in an increasingly complex technological environment, it is essential that Army officers understand the advanced technologies which form critical elements of our evolving weapons systems. One technology field which is already exerting a major influence on force planning, and whose impact is certain to grow over the next two decades, is the physics and engineering of lasers, and the technologies associated with their development and applications. The Army needs a strong base of research and development in laser-related fields. It also needs an officer corps generally familiar with laser technologies and a subset of that officer corps whose members are experts in developing and applying those technologies."

The Photonics Research Center is comprised of researchers from the Departments of Chemistry, Electrical Engineering and Computer Science, and Physics who conduct basic and applied research using lasers and laser technology. The Center's three primary missions focus on *education* of both cadets and officers, the conduct of basic and applied *research*, and *support to the Army* in the area of lasers and photonics. Funding support for the Center is provided through the Physics Division of the Army Research Office.

Each year, educational programs associated with the Photonics Research Center introduce over 1000 cadets to a general familiarity with laser technology, provide over 50 cadets with an in-depth understanding of lasers and laser technology, and returns several officers to the Army who are now considered experts in developing and applying laser technologies. In the area of basic and applied research, the Center maintains upwards of eight active research experiments producing both faculty and student conference presentations and technical journal articles. Specific research areas include laser spectroscopy, laser induced carbonization of polymers, applications of photorefractive devices, ultrafast optoelectronics and switching, optical information processing, stimulated rotational Raman scattering, and remote sensing. Over the past four years, we have developed a mid-career officer education program called *Visualizing the Digitized Battlefield*. This two-day short course has been taught to four consecutive classes of mid-career officers at the U.S. Army Command and General Staff Officer Course, Ft. Leavenworth, Kansas and covers some of the fundamental science that shapes the modern battlefield. Over this same period, the Center's support mission has provided direct support to the Army in the form of Army Research Office technical evaluations of their University Research Initiatives; technical support to the Program Manager of Project SAFEGUARD in the area of Mid-Infrared Imaging and Fourier Transform Spectroscopy for the detection and quantification of chemical warfare agents; technical support to the Program Manager, Defense Threat Reduction Agency and in the area of Passive Gas Phase Infrared Spectroscopy of Chemical Warfare Simulants. Center personnel are also participants in several Defense Advanced Research Projects Agency (DARPA) programs, namely the Photonic Analog-to-Digital Converter Technology (PACT) Program, the Solar Blind Detector (SBD) Program, and the Wavelength and Spatial Signal Processing (WASSP) Program.

Photonics Research Center Staff and Faculty 1998 - 2000

Board of Directors
COL David C. Allbee, Ph.D. in Physical Chemistry, Pennsylvania State University, 1985,
Professor and Head, Department of Chemistry.
COL Andre H. Sayles, Ph.D. in Electrical Engineering, Georgia Institute of Technology, 1990, Professor and
Head, Department of Electrical Engineering and Computer Science.
COL Raymond J. Winkel, Jr., Ph.D. in Physics, University of California at Berkeley, 1984,
Professor and Head, Department of Physics.

Academy Professors
COL Bruce G. Oldaker, Ph.D. in Physics, Massachusetts Institute of Technology, 1990, Associate Professor
(Photonics), Department of Physics.
LTC Barry L. Shoop, Ph.D. in Electrical Engineering, Stanford University, 1992, Associate Professor
(Photonics), Department of Electrical Engineering and Computer Science.
MAJ Augustus W. Fountain, III, Ph.D. in Analytical Chemistry, Florida State University, 1997, Associate
Professor (Photonics), Department of Chemistry.

Title X Civilians
Timothy Pritchett, Ph.D. in Physics, University of California at Berkeley, 1990.
Timothy Talty, Ph.D.,Electrical Engineering, University of Toledo, 1996.
Thomas D. Wagner, Ph.D. in Computer Science, Vanderbilt University, 1993.
Jean R. S. Blair, Ph.D. in Computer Science, University of Pittsburgh, 1986.
Timothy Bays, Ph.D. in Inorganic Chemistry, University of Idaho, 1997.

Rotating Military Faculty
LTC John C. Carrano, Ph.D. in Electrical Engineering, University of Texas at Austin, 1999.
LTC Michael E. Donovan, Ph.D. (ABD) in Optics, University of Arizona, 1999.
MAJ Dennis A. Card, Ph.D. in Physical Chemistry, Pennsylvania State University, 2000.
MAJ Robert P. Fabrizzio, MS in Optics, University of Rochester, 1998.
CPT Raymond L. Wagner, MS in Physical Chemistry, Pennsylvania State University, 1997.
CPT John M. Ingram, MS in Physical Chemistry, University of Idaho, 1999.

*Names in **bold** represent those individuals formally assigned to one of the Table of Distribution and Allowances
(TDA) positions in the Photonics Research Center during the 1996-1998 Academic Year.*

Administration
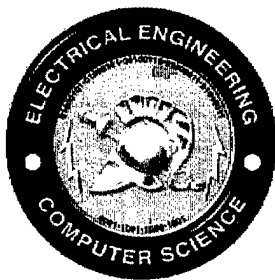Telephone numbers: (prefix: Commercial (914)-938- or DSN 688-)

Director	LTC Barry L. Shoop
Associate Director	MAJ Augustus W. Fountain III
Laboratory Facilities Manager	Mrs. Andrea E. Sanborn
Budget Assistant:	Mrs. JoAnn French

Photonics Research Center
Bartlett Hall, Building 753, Room B21
MADN-PRC
West Point, New York 10996

General Information	x-3739
Facsimile	x-3062
Director	x-5567
Facilities Manager	x-5812
Budget Assistant	x-2624

TABLE OF CONTENTS

EDUCATING ARMY LEADERS FOR THE 21ST CENTURY

COL BRUCE G. OLDAKER, LTC BARRY L. SHOOP,
MAJ AUGUSTUS W. FOUNTAIN III, MAJ ROBERT P. FABRIZZIO II,
LTC THOMAS R. MOORE, AND MAJ WILLIAM W. PRIOR

Photonics Research Center, United States Military Academy, West Point, New York

Since 1997, the Photonics Research Center (PRC) has presented a course to students enrolled in the Advanced Warfighting Course, at the U.S. Army Command and General Staff College (CGSC) at Fort Leavenworth, Kansas. The most recent version of this course, Visualizing a Digitized Battlefield, consists of four hours of instruction taught over two days concluded with three capstone practical exercises.

1 Introduction

The United States Army is arguably in the midst of a revolution in military affairs. This revolution involves the concept of information dominance and the tremendous advantage it affords the force that possesses and most effectively employs it on the modern battlefield [1]. Dramatic developments in advanced technologies have spawned several new combat systems and resulted in extensive modifications to existing equipment. Perhaps more importantly, commensurate changes in Army doctrine and force structure are planned to leverage these new systems with the goal to make the U.S. Army faster, smarter, and more lethal [1]. Training soldiers and leaders to most effectively employ advanced technologies on the battlefield is, as it has always been, central to realizing this goal. Far beyond simple operating instructions, leaders must become subject matter experts on their equipment. They must understand how and why it works at the most fundamental levels. As technological advances are introduced into modern weapon systems, this task becomes more difficult to accomplish with soldiers of diverse educational and cultural backgrounds.

The United States Military Academy Photonics Research Center (PRC) at West Point has been educating both entry-level and mid-career Army leaders for over ten years. In 1996, they undertook a new educational project to introduce mid-career Army officers to science and technology issues that effect the modern battlefield. The purpose of the course was to address a growing need for technical education of leaders as the U.S. Army undergoes a substantial modernization program.
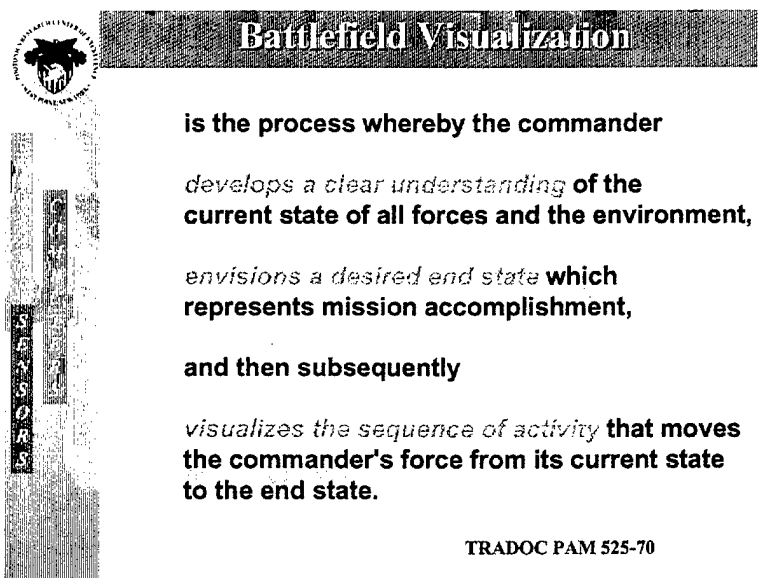
In January of 1997, the first short-course, entitled Science and Technology for Leaders of the 21st Century, was presented to students enrolled in the Advanced Warfighting Course, at the U.S. Army Command and General Staff College (CGSC) at Fort Leavenworth, Kansas. This original version of the course, also presented in January 1998, covered topics including fundamentals of electromagnetic and acoustic waves, reflection and absorption, digitization and networks, power technology, and implications of science and technology to military operations. Following the 1998 iteration, the course was restructured to focus on a single, central theme as well as incorporate elements of Peer Instruction [2] and a major practical

exercise. Over the past four years, over 500 field-grade officers attending CGSC have taken the course in preparation for duty with the Army's newest digitized units.

2 Conduct of the Course

The most recent version of this course, Visualizing a Digitized Battlefield, consists of four hours of instruction taught over two days concluded with three capstone practical exercises.

Faculty from the PRC comprising expertise from the Departments of Chemistry, Electrical Engineering and Computer Science, and Physics participated in the preparation and execution of the course. In order to ensure that the presentation was relevant and familiar to this specific audience, TRADOC PAM 525-70: Battlefield Visualization Concept was used as the framework for all discussions of science on the modern battlefield.

Battlefield Visualization

is the process whereby the commander

develops a clear understanding of the current state of all forces and the environment,

envisions a desired end state which represents mission accomplishment,

and then subsequently

visualizes the sequence of activity that moves the commander's force from its current state to the end state.

TRADOC PAM 525-70

Most of the student officers in attendance were Majors in the U.S. Army, had approximately 12 years of military experience, and had very little formal education in science. All were military professionals who generally understood and appreciated the importance of new technologies as related to classic military theory. They all recognized that effective battlefield visualization is an important prerequisite for information dominance and is one of the military processes most affected by the recent rapid growth of information technology [3].

Rather than divide the course subjects by scientific discipline, a simple model of the tools of battlefield visualization was presented consisting of signals, sensors, computers and displays.

The Tools of Battlefield Visualization

Electromagnetic, acoustical, olfactory

SENSORS

Eyes, ears, nose, machines

Human brain, machines

Human mind, sketch, maps, flat-panel displays...

The basic science of these four components was first introduced and then reinforced by providing specific examples of applications to U.S. Army equipment, some of which were brought to Fort Leavenworth for the students to handle. This new course included instruction on electromagnetic and acoustic waves, emission and reflection, absorption and scattering, and digitization and display technology. The following is an example slide from the digitization sub-course.
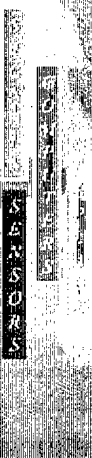
How Do We Digitize A Signal?

Threshold 0

Digital Data Stream
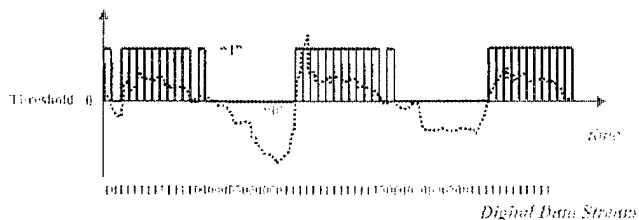
1, 0 - 1-bit (binary digit)

1-bit of resolution -- you know that the original signal was either above threshold or below threshold -- nothing else.
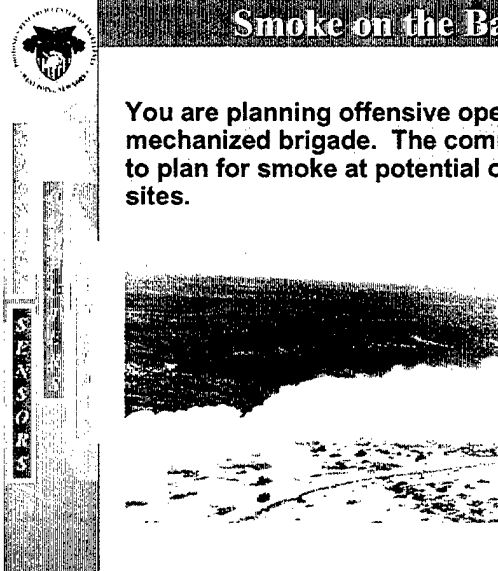
00 (0), 01 (1), 10 (2), 11 (3)   -- 2-bit digital word
000, 001, 010, 011, 100, 101, 110, 111 -- 3-bit digital word

Some have heard of 8-bit digital words

The breadth of coverage of this latest version was reduced to include time for practical exercises. In order to ensure the instruction was student-centered and relevant, several tactical scenarios were presented which required the students to apply the course material to a specific military situation. These scenarios were designed specifically to reinforce the concepts presented earlier in the course. The following example is the exercise that

concluded the first hour of instruction. It integrated traditional military planning considerations with more scientific factors, such as sensor technology and spectral bands.

Smoke on the Battlefield

You are planning offensive operations for a mechanized brigade. The commander directs you to plan for smoke at potential obstacle breach sites.

Assets available include your vehicle on-board smoke generators, an OPCON smoke company, and indirect fires.

List factors you must consider in establishing an effective smoke screen.

Three practical exercises served to capstone the event and were designed to actively involve the students with the subject and to synthesize the information presented over the previous two days of instruction. The large class of 180 students was divided into 10 smaller sections to accomplish these exercises. In the first exercise, students completed a matrix in which they listed tactical and operational considerations for various military terms and definitions in relation to specific wavelength regions. This led into a discussion on how operating in various wavelengths changes tactics as well as training. The second exercise, on digitization and bandwidth, called upon students to make actual calculations of how long it takes to transmit various images using known data transfer rates of common military communication means.

Finally, students were required to analyze a futuristic combat scene and subsequently brief their contemporaries on a specific aspect of technology and its impact on battlefield visualization. A 20-minute segment from the Twentieth Century Fox film *Predator 2* was used as the basis for the practical exercise. While truly science fiction, the film's depiction of many scientific concepts in the context of a military operation was quite accurate and effective for the purposes of this instruction. The practical exercise resulted in lively debate and cogent presentations on the analysis and application of the scientific concepts presented earlier in class to a real military scenario.

At the beginning of the instruction, students were provided two documents intended to facilitate future self-study. The first was a text containing copies of all slides presented. This document served as a note taking device and reference. The second was a manual entitled Directory of U.S. Army Equipment in Support of Digitized Battlefield Visualization. The directory is a detailed guide to many of the current and future U.S. Army systems that will help the commanders of Army XXI visualize the battlefield

Following the course, students have traditionally completed a web-based critique. Responses indicated that the course was one of the best in the CGSC curriculum and that the students were very pleased with the professionalism of the instructors and the course content. Reactions to the practical exercise were positive but with several requests for an exercise involving actual Army equipment. Some of the most telling survey questions, however, showed a vast majority of the officers were convinced that such information was vital to their careers and that this course provided an approach to the subject material that was understandable yet challenging. The consensus was that instruction of this type will be in great demand in the future. As the Army continues to modernize and move toward Army XXI and Army After Next, an expanded battlefield science education program will become necessary.

This past year, in addition to a critique, students completed both a pre- and post-course survey, in which they responded to 20 questions covering material presented during the four hours of instruction. The intent of these surveys was twofold. First, it provided data useful in assessing the knowledge level of students enrolled in the course. Armed with the pre-test results, we were able to concentrate instruction on particular topics and concepts. Secondly, by correlating pre- and post-course results, we could quantify the effectiveness of the course by examining changes in achieved scores. Of the 45 students that we collected correlated data sets on, the average number of correct responses increased from 10.4 to 15.9, and all but two students improved their score by at least two correct responses.

3 Future Direction

In an effort to continue to improve the quality and effectiveness of this short-course, an annual assessment of the course objectives, outcomes, and feedback has been ongoing since the first presentation in 1997. Current plans for improving the course next year center mainly on improving the final practical exercise. This was the second year that the *Predator 2* exercise was included and although it provided a valuable tool for reinforcement of the fundamental scientific concepts, a realistic high-quality movie segment depicting soldiers and U.S. Army equipment is believed to be more applicable and relevant to the student population. A comprehensive textbook for the course is also being considered to provide the students with a more self-contained reference for future use.

Earlier this semester, an abridged one-hour version of this course was presented to approximately 85 USMA cadets enrolled in Physics I (PH201). This was the first time such an endeavor was offered at the undergraduate level and answered suggestions of extending our reach to a pre-commissioning audience.

compiling the equipment directory as well as making available equipment used during the course.

Dr. Frank Mabry (USMA's Department of Electrical Engineering and Computer Science) provided technical support in formatting, collecting, and analyzing the data obtained on the web-based surveys used during this course.

Finally, we would also like to acknowledge the continued support from CGSC's Army Warfighting Seminar as well as Night Vision Laboratory in Fort Belvoir, Virginia.

References

1. U. S. Army TRADOC PAM 525-5, Force XXI Operations, 1 August 1994.
2. E. Mazur, Peer Instruction: A User's Manual (Prentice Hall, Upper Saddle River, N.J., 1997.
3. U. S. Army TRADOC PAM 525-70, Battlefield Visualization Concept, 1 October 1995.

Selected Publications and Conference Presentations

1. Visualizing a Digitized Battlefield classroom text
2. Directory of U.S. Army Equipment to Support Digitized Battlefield Visualization reference book

Cadet Publications and Presentations

None

Cadet Involvement

None

Collaboration

1. PM/NVRSTA
2. NVL

John C. Carrano

Military Rank: Lieutenant Colonel   **Branch:** Armor/Army Acquisition Corps

Home Address: **Office Address:**
264B Beauregard Pl.   Department of EECS
West Point, NY 10996   United States Military Academy
(914) 446-1304   West Point, New York 10996
                                               (914) 938-5557
                                               (914) 938-3062 (FAX)

                                               Email: John-Carrano@usma.edu

EDUCATION:

Ph.D.	The University of Texas at Austin
	Major: Electrical Engineering, 1999
	Dissertation Advisor: Joe C. Campbell
	Dissertation Title: "High-Performance GaN Ultraviolet Photodiodes"
M.S.	The University of Texas at Austin
	Major: Electrical Engineering, 1990
	Thesis Advisor: Jack C. Lee
	Thesis Title: "The Electrical and Reliability Characteristics of PLZT Thin Films for DRAM Applications"
B.S.	United States Military Academy at West Point
	Area of Concentration, Electrical Engineering 1981

RESEARCH INTERESTS:

Primary interests are in semiconductor devices and optoelectronics. Specific research experience includes: thin film dielectrics for high-density CMOS processing; vertical-cavity surface emitting lasers for optical communications and signal processing; III-nitride based solar-blind ultraviolet photodetectors for military sensing and imaging applications; and, III-nitride based high-power electronics for high-temperature and microwave applications. LTC Carrano has co-authored over 35 refereed scholarly publications, and conference presentations.

DEVELOPMENT OF SOLAR-BLIND ULTRAVIOLET PHOTODETECTORS FABRICATED ON III-NITRIDE CRYSTALS FOR MILITARY SENSOR APPLICATIONS

LTC JOHN C. CARRANO

Department of Electrical Engineering and Computer Science, and Photonics Research Center
United States Military Academy, West Point, New York 10996
E-mail: John-Carrano@usma.edu

For decades, sensing and imaging in the infrared (IR) portion of the electromagnetic spectrum has been commonplace and cost-effective, owing largely to tremendous advances in semiconductor materials and optoelectronic devices that were designed to detect light at these wavelengths. Less well known is the fact that the ultraviolet (UV) portion of the spectrum is widely used for a variety of sensing and imaging applications. However, until very recently, with the advent of wide bandgap materials such as AlGaN, there have not been high-performance optoelectronic devices designed for optimal operation in the UV. Thus, the development of sophisticated detection applications in the UV has been limited by the existing technology. This paper outlines our recent advances in the development of high-quality ultraviolet photodetectors fabricated on III-nitride materials. Several specific device structures, and their performance characteristics, are also presented.

1 Introduction

The field of III-nitride ultraviolet photodetectors is the focus of intense research world-wide, owing to a wide range of practical device applications. With the breakthrough results of achieving *p*-type conductivity in epitaxial GaN grown by metal-organic chemical-vapor deposition (MOCVD) and the subsequent demonstration and commercialization of high efficiency light emitting diodes (LEDs), interest has heightened in short-wavelength nitride emitters, photodetectors, and electronic devices. However, despite the success of the GaN LEDs, several technology impediments, both in materials and device development, must be overcome before GaN photodetectors can fulfill their potential and be widely deployed. Novel photodetector designs remain unexplored, despite the importance of detection of ultraviolet wavelengths in solar-blind applications and chemical/biological sensors.

The ultraviolet portion of the electromagnetic spectrum is generally considered to consist of wavelengths from ~400 nm down to ~100 nm. The sun is a strong emitter of UV radiation; however, much of this, especially the dangerous UVC (280 nm and below), is absorbed by the earth's ozone layer. The ozone layer begins to absorb strongly at wavelengths < 290 nm. Thus, any detector capable of detecting only at wavelengths < 290 nm is referred to as a "solar-blind" detector. From a terrestrial location, such a photodetector would theoretically not detect any signal even if aimed directly at the sun. Likewise, a detector designed to detect only wavelengths shorter than ~400 nm is referred to as a "visible-blind" detector by analogy. The ability to detect UV radiation is important to a number of broad areas including scientific research, environmental monitoring, space research, military systems, and commercial applications. For such applications, the most common UV detectors currently in use today are the photomultiplier tube and the UV-enhanced Si photodetector. Both detector types have serious drawbacks. For operation in the deep UV, Si

photodiodes may suffer reduced quantum efficiency owing to a degradation of the SiO_2/Si interface after prolonged UV exposure. In addition, UV-enhanced Si photodetectors are not solar-blind devices. Photomultiplier tubes (PMT) are extremely sensitive UV photodetectors that are capable of achieving, through internal gain, responsivities of >600 A/W [1]. Although PMT's are very effective, they are bulky and require high voltages to operate (usually > 1kV). In addition, the PMT is a fragile device that is not suited for many military or space applications. Like the Si photodetector, it too is not solar-blind. Costly filters must be used to attenuate unwanted visible and IR radiation with the associated insertion loss. Thus, there is the need for a high-performance, solid-state, solar-blind ultraviolet photodetector that can be cost-effectively manufactured into high density arrays. One possible candidate for the construction of such a device is the direct bandgap semiconductor alloy, aluminum indium gallium nitride ($Al_xIn_yGa_{1-x-y}N$).

The $Al_xIn_yGa_{1-x-y}N$ material system is well suited as a photodetector material for operation from the visible to the deep UV. The AlInGaN quaternary alloys offer the advantage of independently selecting the lattice parameter and the band gap energy of the crystal. Potential uses of such UV semiconductor photodetectors include military, space-based, environmental, and some industrial applications for which older photomultiplier tube technology is inappropriate. Specifically, III-nitride based photodetectors could be fabricated into two-dimensional arrays that are suitable for army sensor fusion applications, as well as multi-spectral imaging systems. Furthermore, its wide bandgap and other material properties make it suitable for a variety of harsh environments. Because an AlInGaN UV photodetector allows for solar-blind operation, it can be designed to detect ultraviolet signatures against a warm background (such as from space looking back at the warm earth), or from a terrestrial (or airborne) position looking up at a target descending out of the sun.

Targets of military interest emit ultraviolet radiation from two primary sources. For the case of a missile in ascent, there is a UV signature associated with the missile plume that is very localized to the rocket engine (as opposed to the IR signal which may be spread out spatially). For hypervelocity missiles on final trajectory, there is a UV signature associated with the bow shock wave. For atmospheric detection one must achieve very high quantum efficiency and detectivity, since the typical signatures are known to be very weak, and UV propagation in the atmosphere is poor due to Rayleigh scattering at the shorter wavelengths. Therefore, one would like to use a *p-i-n* heterostructure photodetector due to its high sensitivity and potential for high speed.

A number of groups (including the USMA/UT collaboration) have reported on heterojunction *p-i-n* photodiodes with good performance characteristics. Additionally, our combined groups, and the MIT-LL group, have reported on low-gain GaN-based APDs [2]. Also, there have been some recent reports of solar-blind photodetectors [3]. On the other hand, high-quality truly solar-blind III-N advanced heterojunction photodetectors with fast response times, low noise, low dark currents, and high gains have not yet been demonstrated by any group.

The development of high-performance III-nitride based photodiodes has been constrained owing largely to limitations in crystal quality. Most GaN- and AlGaN-based devices are constructed of epitaxial layers grown on highly lattice mis-matched substrates such as sapphire. The resulting severe strain between layers causes an unusually high density of threading dislocations, routinely reported to be on the order of 10^7 cm^{-2} to 10^{10} cm^{-2} .

Moreover, the difficulty in growing nitride-based materials results in crystals fraught with a high density of native defects, and impurities. The trap states introduced by threading dislocations and other defects in GaN and AlGaN have been shown to have a deleterious impact on current transport, quantum efficiency, dark noise, and temporal behavior. Therefore, a major goal in the development of III-nitride based photodiodes must be the reduction of defects, and in particular, threading dislocations.

The goal of this research project is the development and comprehensive analysis of AlInGaN-based solar-blind ultraviolet photodetectors using advanced heterostructure devices. Specifically, we have been focusing on the design, simulation, fabrication, and characterization of solar-blind separate absorption, charge, and multiplication (SACM) avalanche photodiodes (APDs) constructed of epitaxial layers of the quaternary alloy AlInGaN. Performance has been evaluated in terms of critical device parameters, such as dark current, speed, bandwidth, noise, gain, and quantum efficiency. Models describing current transport, quantum efficiency, and temporal response are being developed in order to optimize device designs. This work has built upon our previous success with GaN and AlGaN based *p-i-n* ultraviolet photodetectors. Particular emphasis is being given to yield and uniformity issues across large wafers as evaluated by electrical and optical criteria. This research constitutes an important step in the development of III-nitride solid-state photodetector arrays suitable for DoD sensor applications.

2 Experimental Methods

Our approach involves three interwoven parallel efforts, namely: device design and simulation, electrical and optical characterization, and the construction of detailed device models. Knowledge of important device physics gained from analysis of the constructed models will, of course, be used to optimize new device designs. The devices to be measured and analyzed consist of photodiodes fabricated in AlInGaN using a variety of advanced heterostructure designs. Wafer level probing is performed on these devices using a low-noise test station. Data is obtained using a parameter analyzer for current-voltage, and current-time measurements, and an LCR-bridge for capacitance-voltage and conductance measurements. Large sample sets of the aforementioned devices are being tested in order to obtain statistical information on crystal growth and device fabrication uniformity. From the above electrical measurements, and using the appropriate physical relationships, one can extract important device parameters such as dark current level, magnitude of the photoresponse, depletion region punch-through voltage, total series resistance, ideality factor, intrinsic capacitance, breakdown voltage, doping levels, and gain. More importantly, using the appropriate mathematical models one can study the nature of current transport in the photodiodes, the electric field distribution within the device, and gain mechanisms.

Temporal and frequency response measurements are used to determine the highest speed (or largest bandwidth) that a photodetector can achieve. This is important for missile tracking and intercept applications in which high-speed is required. Using solid-state Q-switched lasers to produce UV pulse widths of ~1 nsec in a sophisticated experimental apparatus, we can measure the step response of a photodetector to UV excitation. The apparatus allows us to analyze device performance as a function of reverse bias level, excitation wavelength (we have two laser lines to choose from), and incident UV intensity.

Each of these parameters is critical to evaluating the potential of the devices to function in a practical UV sensor array.

Finally, by studying these devices over the entire area of a large wafer (note that for the nascent AlInGaN material system, a 2 inch wafer is large), we can learn important facts about the quality of our crystal growth techniques, and device fabrication processing procedures. This is important in order to eventually transition this technology to commercial industry for large scale production.

3   Results and Discussion

3.1   Carrier velocity and device temporal characteristics

The temporal and frequency domain characteristics of MSM devices have also been measured, the details of which have been reported elsewhere [4]. The 10%-90% rise-time is ~28 psec at 25 V reverse bias. Using the relation, $f_{3dB} \cdot \tau_{10\%-90\%} = 0.35$, the bandwidth is estimated to be ~12 GHz. f_{3dB} is the cut-off frequency and $\tau_{10\%-90\%}$ is the measured rise-time. Figure 1 is a summary of the speed results of our MSM photodetectors. We use the full-width-at-half-maximum (FWHM) as a figure-of-merit for comparison purposes. As can be seen, the FWHM decreases with increasing reverse bias for all three gap spacings. The FWHM also decreases with decreasing gap spacing.
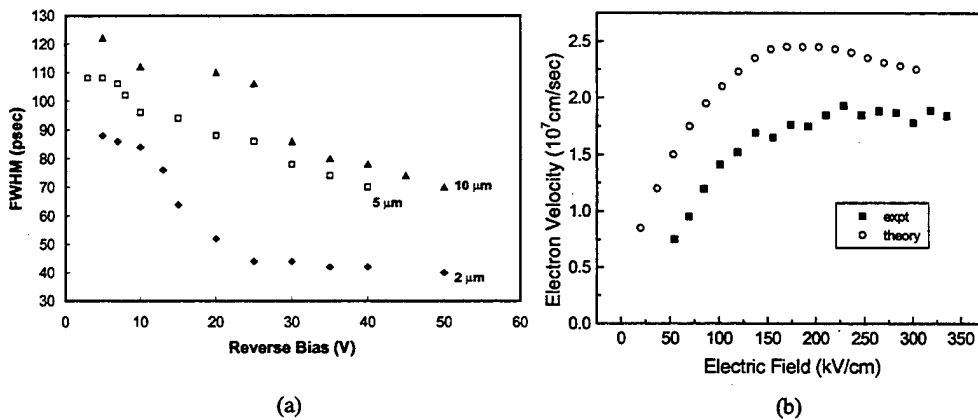
Figure 1. (a) A summary of the MSM speed results for devices with gap spacings of 2 μm, 5 μm, and 10 μm gap spacings using the FWHM versus reverse bias as a gauge for comparison. The devices scale with bias and gap spacing as expected for a transit-time limited case. (b) Electron transit time as a function of electric field.

The data presented in Fig. 1a, although representative of only course trends, clearly indicate that the FWHM scales with reverse bias and gap spacing as one would expect in a transit-time limited case. Indeed, the 2 μm device data does indicated a quasi-saturation in the FWHM for reverse bias >25 V. For this geometry, this saturation point corresponds to an electric field value of ~125 kV/cm. In order to better interpret this temporal data, we have measured the electron carrier velocity in GaN as a function of electric field. We have measured the electron time-of-flight using an electroabsorption technique, the details of which we have published elsewhere [5]. The results of this experiment are shown in Figure

3-4

1b along with recently published theoretical data for comparison purposes [6]. As can be seen in Figure 1b, the measured electron velocity is somewhat lower than that predicted by the simulation results. This is not surprising, considering that the measurements were performed on non-LEO GaN in which a relatively high defect density is expected. This defect density is not fully accounted for in the simulations. Also note that the electron velocity begins to saturate near 125 kV/cm. However, we find that based on the expected carrier transit time in these device structures (~13 psec), the predicted bandwidth is >30 GHz using the relation:

$$BW = \frac{2.8}{2\pi\tau_{tt}} \tag{1}$$

where, $B.W.$ is the 3 dB bandwidth, and τ_{tt} is the transit-time of the respective carriers. Thus, other effects must play an important role in the overall device time response.

We believe that the slow component tail evident in the pulse response data can account for the apparent discrepancies. A fit of a representative transient response curve to a model that accounts for the independent collection of electrons and holes has been reported elsewhere [7]. Using the pulse associated with hole collection we obtain a rise-time of ~90 psec, which corresponds to a bandwidth of ~3.8 GHz, and is in very close agreement with both the measured and the calculated frequency response. We have also taken the FFT on the –25V time domain pulse and obtained $f_{3dB} \approx 3.5$ GHz. This is further indication that the true bandwidth is dominated by the slower collection time of holes. Using Eqn (1), this implies a hole transit time of ~117 psec. Based on the hole transit time and the device geometry, we obtained a calculated hole carrier velocity of ~1.7 x 10^6 cm/sec. Although we have not yet directly measured the hole velocity in GaN, some published theoretical data based on Monte Carlo simulations exists in the literature [6]. This data predicts a hole velocity of ~4 x 10^6 cm/sec at the reverse bias level used in our speed measurement. Since, we have found the measured electron velocity to be less than the theoretical electron velocity, we conclude that our calculated hole velocity is reasonable.

3.2 Avalanche Photodiodes

As alluded to earlier, UV photodetectors fabricated in AlInGaN are attractive alternatives to the aging vacuum-tube-based technology of photomultiplier tubes (PMTs). However, in order that GaN-based photodiodes be considered as viable PMT replacements, they must be able to achieve high sensitivity. For the case of the MSM photodiodes, there is a significant tradeoff between gain, bandwidth, and noise. An attractive alternative for achieving high gain at high speed is the avalanche photodiode (APD).

To date, there have been few reports of the observation of avalanche gain in a GaN-based photodiode; for those devices that have been described, microplasmic effects were a dominant factor in the performance [8]. The existence of microplasmas in GaN-based photodiodes biased at high reverse voltages comes as no surprise. We have fabricated GaN-based APD's that show modest gain in the absence of microplasma emissions. In order to achieve appreciable avalanche gain, the peak electric field intensity in the gain region must be close to the critical field, E_{cr}. One signature of avalanche gain is that, near breakdown, the current-voltage characteristics exhibit a soft-breakdown response, i.e., the second derivative of the I-V curve is positive. Figure 2a shows the UV photoresponse to excitation with 363 nm light, and the associated dark current of a 25 µm-diameter APD. Both I-V curves show

the requisite shape at high electric fields. A plot of the current multiplication is shown on the right axis; near breakdown the gain is > 25. This value is commensurate with that reported by Verghese, et al. [9], and significantly higher than that reported by Osinsky, et al. [8]. At very high electric fields, the large-area devices (mesa diameter > 50 μm) show an abrupt breakdown, which is characteristic of microplasma formation. When these devices are biased at high reverse voltage, small, point-like light-emitting regions, which are characteristic microplasma emissions, are observed scattered across the device mesa (Fig. 2b). In contrast, many of the small-area devices exhibit a smooth gain curve (Fig. 2a), and no microplasma emissions are observed, even at very high electric field. We speculate that reducing the area of the mesa enhances the chances of obtaining relatively defect free regions that show stable avalanche gain. We note that the magnitude of the electric field at breakdown corresponds to ~3.5 MV/cm. This value agrees well with published simulation data of electron initiated impact ionization in GaN. When microplasmas are first observed, they appear at electric field levels well below the critical field.

Another indicator of avalanche gain is a positive temperature coefficient of the breakdown field. As the temperature increases, so does carrier scattering, owing to carrier-phonon interaction [10]. Therefore, a higher electric field intensity value is required to

(a)   (b)
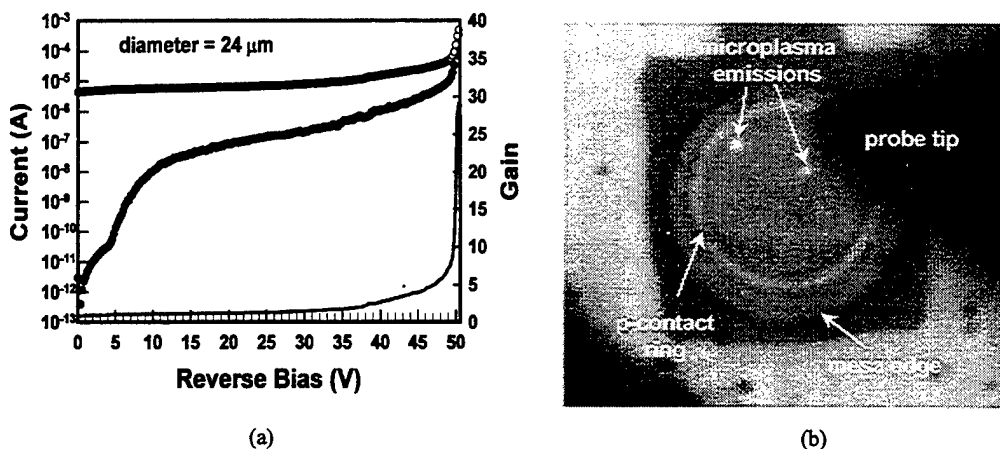
Figure 2. (a) Reverse I-V characteristics in the dark and with UV illumination. The right hand axis indicates the multiplication. (b) Microplasma emissions from a large area APD.

accelerate the carriers to sufficient kinetic energy to initiate impact ionization; this results in a positive temperature coefficient. We obtained a positive temperature coefficient of 2.2 mV/°K. This value agrees well with that reported by Osinsky et al. [8] However, with so little data available on this parameter, there is still a great deal of uncertainty.

4 Conclusion

We have constructed high-performance III-nitride based photodiodes operating in the visible-blind portion of the ultraviolet spectrum. We expect that the progress made to date will enhance our success at developing truly solar-blind high-density arrays for military uses.

5 Acknowledgements

References

1. H. Morkoç, "Wurtzite GaN-Based Heterostructures by Molecular Beam Epitaxy," *IEEE J. of Selected Topics in Quantum Elec.,* 4 (3), 537 (1998).
2. McIntosh, K. A., Molnar, R. J., Mahoney, L. J., Lightfoot, A., Geis, M. W., Molvar, K. M., Melngailis, I., Aggarwal, R. L., Goodhue, W. D., Choi, S. S., Spears, D. L., and Verghese, S. (1999). GaN avalanche photodiodes grown by hydride vapor-phase epitaxy, *Appl. Phys. Lett.* **75** (22), 3485.
3. Parish, G., Keller, S., Kozodoy, P., Ibbetson, J. P., Marchand, H., Fini, P. T., Speck, J. S., DenBaars, S. P., and Mishra, U. K. (1998). High-performance (Al, Ga)N-based solar-blind ultraviolet *p-i-n* detectors on laterally epitaxially overgrown GaN, *Appl. Phys. Lett.,* **75** (2) 247.
4. J. C. Carrano, T. Li, C. J. Eiting, R. D. Dupuis, and J. C. Campbell, "Very High-Speed Ultraviolet Photodetectors Fabricated on GaN," *J. Elec. Mat.,* **28** (3) 323 (1999).
5. M. Wraback, H. Shen, J. C. Carrano, T. Li, and J.C. Campbell, M. J. Schurman, and I. T. Ferguson, "Time-Resolved Electroabsorption Measurement of the Electron Velocity-Field Characteristic in GaN," *Appl. Phys. Lett.,* submitted for publication (1999).
6. Kolnik, I.H. Oğuzman, K.F. Brennan, R. Wang, P.P. Ruden, and Y. Wang, J. Appl. Phys. **78**, 1033 (1995).
7. J. B. D. Soole, and H. Schumacher, IEEE Trans. Elec. Dev., **37** (11), 2285 (1990).
8. A. Osinsky, M. S. Shur, R. Gaska, and Q. Chen, *Electron. Lett.,* 34 (7), 691 (1998).
9. S. Verghese, K. A. McIntosh, R. J. Molnar, C.-L. Chen, K. M. Molvar, I. Melngailis, and R. L. Aggarwal, *Proc. 56th IEEE Device Research Conf.,* p. 54, Charlottesville, VA (1999).
10. T. Kaneda, "Silicon and Germanium Avalanche Photodiodes," in *Semiconductors and Semimetals,* Vol. 22, W. T. Tsang, editor, Academic Press, Orlando, FL.

Future Direction

Our future research will focus on the construction of backside illuminated solar-blind photodiodes that meet the rigorous specifications for military applications.

Selected Recent Publications and Conference Presentations

1. J. C. Carrano, "III-Nitride Ultraviolet Photodetectors," invited book chapter in *III-V Nitride Semiconductors: Applications and Devices* edited by Omar Manasreh, and Ed. T. Yu (Gordon and Breach: 2000)
2. J. C. Carrano, T. Li, B. Yang, C. Collins, S. Wang, A. L. Beck, R. D. Dupuis, J. C. Campbell, M. Wraback, P. Shen, M. J. Schurman, I. A. Ferguson, "High-Performance GaN/AlGaN-Based Ultraviolet Photodetectors" invited talk at *SPIE 2000,* San Jose, CA, Jan 2000.

3. M. Wraback, H. Shen, J. C. Carrano, T. Li, and J.C. Campbell, M. J. Schurman, and I. T. Ferguson, "Time-Resolved Electroabsorption Measurement of the Electron Velocity-Field Characteristic in GaN," invited paper at *Materials Research Society*, Spring 2000 Meeting.
4. J. C. Carrano, C. Collins, T. Li, S. Wang, B. Yang, A. L. Beck, D. Lambert, C. Eiting, R. D. Dupuis, and J. C. Campbell "GaN Avalanche Photodiodes," *Appl. Phys. Lett.*, **76** (7), 924. (2000).
5. J. C. Carrano, T. Li, P. A. Grudowski, R. D. Dupuis, and J. C. Campbell, "Improved Detection of the Invisible: High-Performance AlGaN-based Photodiodes Provide Alternatives in Ultraviolet Light Detection," invited paper in *IEEE Circuits and Devices Magazine*, Vol. 15 (5), Sep (1999).
6. M. Wraback, H. Shen, J. C. Carrano, C. J. Eiting, and R. D. Dupuis, "Picosecond Photoinduced Reflectivity Studies of GaN Prepared by Lateral Epitaxial Overgrowth," invited talk at *SPIE 2000*, San Jose, CA, Jan 2000.
7. M. Wraback, H. Shen, J. C. Carrano, T. Li, and J.C. Campbell, M. J. Schurman, and I. T. Ferguson, "Time-Resolved Electroabsorption Measurement of the Electron Velocity-Field Characteristic in GaN," *Appl. Phys. Lett.*, 75 () (2000).

Collaboration

1. Professor Joe C. Campbell, The University of Texas at Austin.
2. Professor Russell D. Dupuis, The University of Texas at Austin.
3. Dr. Michael Wraback, Army Research Laboratory, Adelphi, MD.

Michael E. Donovan

Military Rank: Lieutenant Colonel

Branch: Field Artillery/Nuclear Research and Operations

Home Address:
235-B Barnard Loop
West Point, NY 10996
(914) 446-4215

Office Address:
Photonics Research Center, Bldg. 753, Rm. B21
United States Military Academy
West Point, New York 10996-5000
(914) 938-5810
(914) 938-3062 (FAX)

Email: hm6688@usma.edu

EDUCATION:

Ph.D. (ABD) Optical Sciences Center, University of Arizona, Tucson, AZ
Major: Optical Sciences
Dissertation Advisor: Nasser Peyghambarian
Dissertation Title: "Experimental Observation of Excitonic Rabi Oscillations and Dark States in Semiconductors"

M.S. Optical Sciences Center, University of Arizona, Tucson, AZ
Major: Optical Sciences, 1998

M.S. Massachusetts Institute of Technology, Cambridge, MA
Major: Physics, 1990
Thesis Advisor: Michael Feld
Thesis Title: "Velocity Selection to Enable Direct Observation of Single Atom-Optical Cavity Vacuum Rabi Splitting"

B.S. United States Military Academy, West Point, NY
No major, 1981

RESEARCH INTERESTS:

Optical physics: Quantum and nonlinear aspects of the light-matter interaction, femtosecond and picosecond spectroscopy. Applied optics: Beam propagation and interferometric imaging.

CONSTRUCTION OF A TEM$_{00}$, NARROW-BANDWIDTH, PASSIVELY Q-SWITCHED Nd:YAG LASER

LTC MICHAEL E. DONOVAN AND CAPT LEANNE HENRY

Department of Physics and Photonics Research Center
United States Military Academy, West Point, New York 10996
E-mail: hm6688@usma.edu

We have constructed a passively Q-switched Nd:YAG laser that meets the requirements for seeded rotational Raman scattering experiments. The laser incorporates a telescope that increases the cavity mode volume in the gain crystal, increasing the power without the instabilities associated with a long cavity. Output pulse energy is limited to about 27 mJ by multiple Q-switching behavior above a certain pumping threshold, but a chain of three Nd:YAG amplifiers increases the output to 550 mJ/pulse. Frequency doubled pulses are 60 ns in duration with an energy of 120 mJ, a factor of seven better than achieved without the telescopic resonator. Design methods, cavity construction, and operating characteristics are discussed.

1 Introduction

The Photonics Research Center has experimented off and on with stimulated rotational Raman scattering (SRRS) over the last decade [1-6]. To date, the experiments have used unseeded hydrogen cells, meaning that SRRS has been initiated stochastically from the spontaneous Raman effect. Some of these experiments have used frequency-doubled picosecond pulses from a mode-locked Nd:YAG laser, but in order to more accurately apply a steady state model to the SRRS process the researchers decided to use a nanosecond pulse laser. An active Pockels cell Q-switch was use to produce 10 ns pulses, but was later replaced by a passive Q-switch which produced 20-30 ns pulses and a narrower output bandwidth while eliminating troublesome r.f. noise. The 17-mJ pulses achieved with this laser were 1.6 times the SRRS threshold [4], sufficient for the unseeded experiments. For seeded Stokes component experiments, however, approximately 50-100 mJ pulses are needed and this became the objective of a resonator redesign incorporating a telescope. The objective of the work this year was to rebuild the laser in the new design.

Many high-powered lasers use unstable resonators to avoid the small mode-volume of a short-cavity stable configuration [7]. However, an unstable cavity cannot in principle produce the TEM$_{00}$ mode that our SRRS model is based on, so it was not an option [8]. Longer stable cavities can have a relatively large mode volume if the gain crystal is near a mirror,[1] but are often avoided because they can magnify the effects of thermal fluctuations and because of practical space considerations. A stable, telescopic resonator produces the larger mode volume of a long cavity without the accompanying environmental sensitivity [9,10], and so it was adopted for our laser. In essence, the telescope acts as a beam expander with a smaller waisted Gaussian beam on the output side and a larger waisted Gaussian beam on the gain and high-reflector side.

A further consideration for our laser design was that the SRRS theory assumes monochromaticity. To this end, we sought to achieve single longitudinal mode output.

---

[1] Actually a short cavity can have a large mode volume if the gain medium is near one of the mirrors, but only by having a pinpoint beam at the other mirror. A pinpoint beam is unacceptable for a high-power laser.

Spreadsheet optimizer routines (on Excel) were used to optimize the spot size and minimize the bandwidth. As shown by Steffen *et al.* [11], small changes in the separation of the lenses in the telescope can correct for the thermal lensing of the Nd:YAG rod. We found it necessary to use an intracavity etalon and resonant reflector output coupler to narrow the gain to only a few lasing modes. The passive saturable absorber Q-switch further discriminates among modes since about 4000 passes through the resonator are required to bleach the absorber. A small gain differential between modes becomes a very large difference in the relative contributions to the output pulses.

2 Cavity Design Model

The cavity design was essentially completed in AY 97-98 by the team of Cadet Chapman, Cadet Rohrbough, and Colonel Oldaker. Unfortunately, that team was unable to adjust the intracavity telescope with enough precision to stabilize the output. We have corrected that deficiency with a redesign of the telescope hardware, a photograph of which is shown as Figure 1.
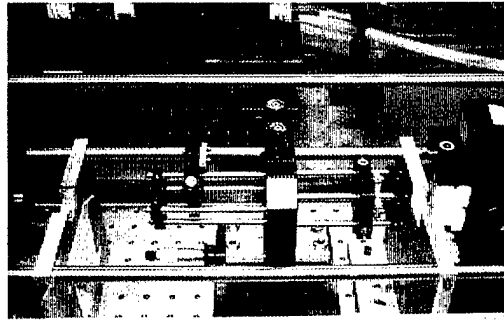
Figure 1. A photograph of the laser intracavity Galilean telescope. Four rods hold the positive and negative lenses on either end. The hardware allows adjustment in every direction (ten degrees of freedom). On the right side of the photograph the laser head is visible. The structure that supports the laser is also visible.

A schematic of the final laser design is shown in Figure 2. The laser cavity is formed by a concave high reflector mirror with a radius of curvature of 500 cm and a planar output coupler. The output coupler is an uncoated Fabry-Perot etalon with a maximum reflectance of about 18%. The multiple beam interference in the output coupler plays a role in longitudinal mode selection along with a linear polarizer and intracavity Fabry-Perot etalon.

The optics of the resonator is designed to put the laser well within the theoretical stability region (low geometric losses). Furthermore, the laser is dynamically stable (insensitive to pump fluctuations) because of the telescope. The Nd:YAG crystal exhibits thermal lensing, with a pump power dependent focal length. The telescope helps again in this regard, as the space between the telescope lenses can be adjusted to compensate for the thermal lensing. (See reference [10] for a detailed discussion of the telescopic resonator.) We have tried to achieve mechanical stability of the laser by building a sturdy frame holding three invar rods with five supports and shielding the laser from air currents with a Plexiglas cover.

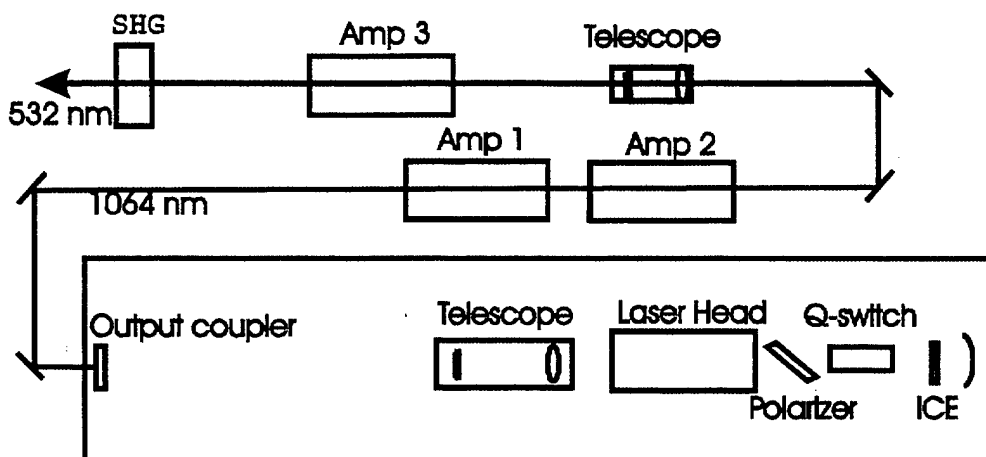**Figure 2.** Schematic of laser and amplifiers. The ICE is the intracavity etalon. The laser head and amplifiers each consist of two flashlamps in a double elliptical reflector, a 7 mm x 115 mm Nd doped YAG rod, power to the flashlamps, and water cooling lines. The Q-switch is a rectangular LiF rod with color centers created by irradiation. The polarizer is a plate at Brewster's angle. The intracavity telescope creates a larger beam in the gain medium. The extra-cavity telescope compensates for beam divergence and increases intensity in the KD*P doubling crystal.

Both the intracavity and output coupler etalons narrow the bandwidth of the laser output. The 10 mm thick intracavity etalon has a 35% reflectance on both faces, resulting in a free spectral range of 10.0 GHz and a transmission linewidth (FWHM) of 3.5 GHz versus the 120 GHz (homogeneously broadened) gain bandwidth of the Nd:YAG crystal. We measured the delay of the Q-switched pulse relative to the onset of pumping and determined that a pulse makes about 4000 trips through the resonator before the Q-switch opens. For one mode to be suppressed by a factor of 100 over another mode, it is necessary that the difference in gain coefficient minus logarithmic loss ($g - \gamma$) between the modes be only 0.0012.[2] This corresponds to being off-center of the central etalon transmission peak by 54 MHz, somewhat less than half the longitudinal mode spacing of the laser (125 MHz).[3] Adjacent transmission maxima of the Fabry-Perot etalon are suppressed by 2% due to the gain curve; this is more than enough to ensure they do not lase. The output coupler, also a Fabry-Perot etalon but in the reflection mode with regards to the laser cavity, also tends to discriminate among modes. We thus conclude that the laser is operating in a single longitudinal mode, and have no contradictory experimental evidence.

Dr. Thom Moore added the passive Q-switch, a color-center LiF:F_2^- crystal saturable absorber, to the laser design. We measured the unsaturated transmission of this crystal to be 50%. It is well known that color centers decay with time, particularly when exposed to ultraviolet light [13]. One of our color center crystals seems to have become ineffective, perhaps due to the decay of its color centers, although there is no visible change. The spontaneous decay time of the Q-switch crystal (54 ns [14], 105 ns [15], 100 ns [16]) is comparable to the pulse duration (60 ns), which is well known to lead to multiple Q-switching [17]. We are only able to avoid the multiple pulses by limiting the pump energy to well below the capability of the flashlamps. Regardless of the pump energy, the energy per

---

[2] These astounding numbers are due to exponential gain, as described in reference [12].

[3] This estimate assumes equal gain in both modes in the absence of the etalon, which is reasonable considering that about 1000 laser lines fall within the FWHM of the laser gain curve.

pulse seems to be limited to about 30 mJ. With higher pump powers the energy is divided among several pulses.

3 Laser Operating Characteristics

3.1 Single Q-switched Pulses

Our laser typically emits 60 ns, 27 mJ pulses at a repetition rate of 10 Hz. The pulse energy can be amplified up to 550 mJ by a chain of three Nd:YAG amplifiers and frequency doubled by a KD*P crystal. The 532 nm wavelength, frequency doubled pulses have a pulse energy of up to 120 mJ. We are confident that we could further increase the pulse energy since the amplifiers and frequency doubling are not optimized. The amplitude is stable to about ± 10% between consecutive pulses and the pulse duration is stable to about ± 1 ns. Jitter is on the order of 3 µs from pulse to pulse and output power can fluctuate 10% over several seconds.
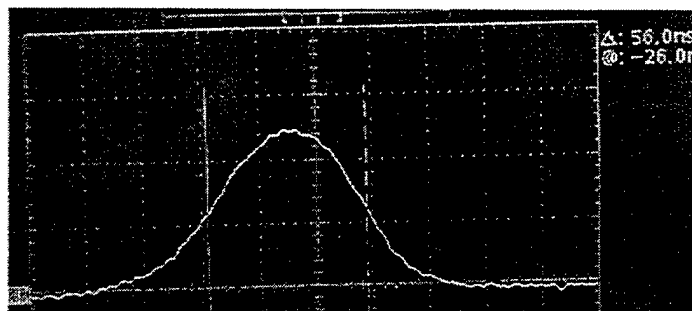
Figure 3. Oscilloscope trace of an amplified, frequency doubled (532 nm wavelength) output pulse. The pulse width is 56 ns (FWHM). This pulse has about 80 mJ of energy and a TEM_{00} beam profile. The detector is a 2 ns rise time silicon photodiode. The oscilloscope has a 500 MHz bandwidth, and in this figure shows 20 ns per major division.

The transverse beam profile matches the fundamental Gaussian mode with a fit coefficient of 90%-94% when optimized. Higher order modes appear when the laser is misaligned. The amplification process is linear in input beam intensity, so it does not affect the profile, but the second harmonic generation is not. The green (532 nm) pulse, however, still has a smooth near-Gaussian profile.

The high voltage to the flashlamps is adjustable, allowing us to vary laser power. However, the cavity must be optimized for each particular flashlamp voltage due to thermal lensing of the Nd:YAG rod. Furthermore, the laser cannot be made to operate at more than about 30 mJ per pulse without multiple pulse output. Thus we find it preferable to adjust the amplification; two of the amplifiers are run off a high voltage source distinct from that which powers the laser head.

3.2 Multiple Q-switched Pulses

Multiple Q-switching behavior is shown in Figure 4. The number of pulses depends on the power to the flashlamps, but the first pulse is usually the largest. The average energy per pulse in a train is typically (20 ± 10) mJ regardless of the pump power. The spacing between consecutive pulses varies with pump power and can be uneven, but is generally around 10-20

μs. The time delay between pulses at a given pump power, however, is the same with every shot, and the pulse durations are similar. The amplitude of pulses other than the first varies more than 20% shot to shot.

|--50 μs--|
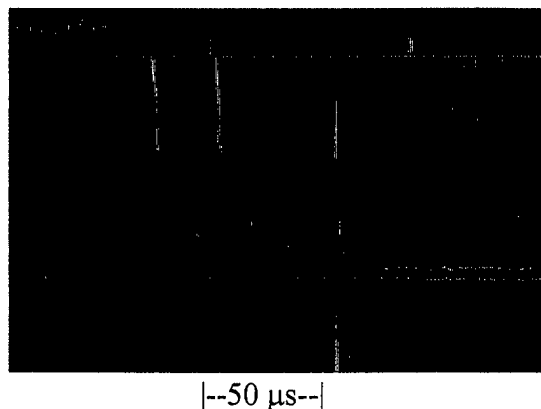
Figure 4. Oscilloscope trace of an output pulse train from multiple Q-switching. The major divisions are 50 μs, so the pulse widths are unresolvable on this scale. Likewise, the amplitudes are not meaningful. However, one can see that the laser has emitted six pulses spread over 75 μs. The pulse spacing is uneven, but it is the same for every shot and varies from about 10-20 μs.

3.3 Non Q-switched behavior

If the Q-switch is removed from the laser, the output exhibits spiking from relaxation oscillations [18] for the duration of the flashlamp flash. The spiking sometimes shows the exponential damping expected of relaxation oscillations, and sometimes shows an irregular behavior. The spikes typically have durations of 0.6 -1 μs, with 2 - 4 μs between spikes.
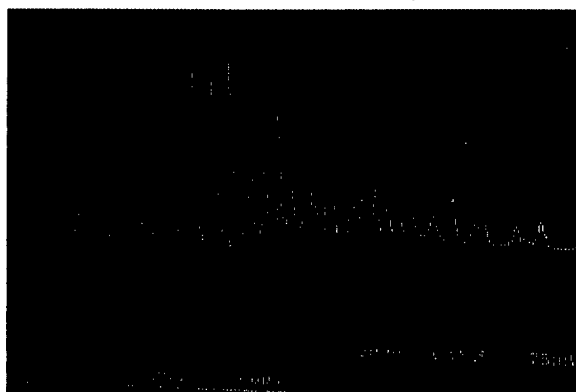
Figure 5. Damped relaxation oscillations from the laser with the Q-switch removed. The duration of the flashlamps is about 100 μs. The spikes are 0.6 – 1 μs, separated by 2-4 μs (slightly more at the end).

3.4 Output without the intracavity etalon

Before we added the intracavity etalon, the Q-switched laser pulses often exhibited a modulation at a period of 4 – 9 ns (see Figure 6). This modulation sometimes neared 100%, but was more typically 10% or less, depending on the laser alignment. Similar behavior is described in the 1996 ARO technical review report, which describes an short-cavity, planar-planar Nd:YAG laser with a LiF:F_2^- Q-switch. The modulation was attributed to interference

between longitudinal laser modes. The regular spacing and amplitudes of the modulation would imply a fixed phase relation between the modes. If this is all correct, then the modulation would be due to partial mode-locking, and we would expect a pulse separation of 9 ns (which we sometimes, but not always, saw).
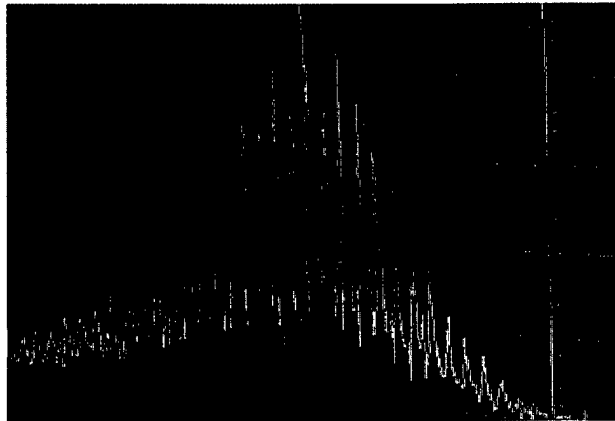
Figure 6. A single Q-switched pulse showing 9 ns modulation of undetermined origin. Such behavior was present to varying degrees without the intracavity etalon and has not been seen with the etalon. The major horizontal divisions are 50 ns.

It is unclear what mechanism could have caused mode-locking in our laser. We initially thought that the modulation could be an artifact of the measurement. We ran tests to ensure it was not a characteristic of the detector and that it was not due to impedance mismatch. We ensured that it was not r.f. pickup. Our 500 MHz digitizing, sampling oscilloscope will sometimes show 4 ns modulation when poorly triggered, but that did not seem to be the same as the modulation we were observing. To see if it was the digital scope, we used a fast (1 GHz) analog oscilloscope and sometimes saw modulation, but it was small and faster than what we saw with the digital oscilloscope. We did not make an exhaustive study with the analog scope since its triggering limitations made it very difficult to use. We believe the modulation is probably real, but we are working near the limits of our instruments.

If the modulation is from the laser, and longitudinal mode interference is its source, then we would not expect to see modulation in single mode operation. We have not seen modulation with the intracavity etalon. An interesting possibility is that, when the laser is multiply Q-switching, the first pulse could be modulated and the other ones smooth. We expect this because only the first pulse would arise from spontaneous emission. The other pulses, which are seeded, should better discriminate between longitudinal modes due to gain competition. We would like to investigate this idea when we next see pulse modulation.

4 Conclusions

We have succeeded in our primary objectives for this academic year: to construct a laser satisfactory for the SRRS experiments and to provide a valuable research experience for two talented cadets. Along the way, we observed some interesting laser phenomena that affected the way we built and characterized the laser. We do not fully understand the pulse modulation that we saw, but the modulation along with the passive Q-switching process could contain some interesting science. In any event, the current single pulse output appears

to be single mode and stable. The pulse power and pulse duration should be satisfactory for the seeded SRRS experiments.

5 Acknowledgements

We would like to thank Mr. George Geysen for assisting us with the electronics and Mr. Bud Warran for doing several machining projects and guiding the cadets in construction of the laser cover.

References

1. MAJ Leo Hergenroeder and LTC Bruce G. Oldaker, "Stimulated Rotational Raman Scattering," *Photonics Research Center 1990 Program Review*, pp. 20-21.
2. MAJ Marion Van Fossen and LTC Bruce G. Oldaker, "Polarization Effects in Stimulated Rotational Raman Scattering," *Photonics Research Center 1992 Program Review*, pp. 24-25.
3. MAJ Vern L. Davis, MAJ Marion Van Fossen and LTC Bruce G. Oldaker, "Polarization Dependence of Stimulated Rotational Raman Scattering in H_2," *Photonics Research Center 1992 Program Review*, pp. 48-52.
4. Lieutenant Colonel Thomas R. Moore and Lieutenant Colonel (P) Bruce G. Oldaker, "Polarization Dependence of Stimulated Rotational Raman Scattering in H_2," *Photonics Research Center 1996 Program Review*, pp. 81-85.
5. B. Oldaker, T. Pritchett and T.R. Moore, "Stimulated Rotational Raman Scattering in H_2," in *Nonlinear Frequency Generation and Conversion*, D. C. MacPherson, ed., (Society of Photo-Optical Instrumentation Engineers, Bellingham, WA, 1996) Vol. 2700.
6. Colonel Bruce G. Oldaker, "Lasers and Optics Education," *Photonics Research Center 1998 Program Review*, pp. 69-77.
7. Peter W. Milonni and Joseph H. Eberly, *Lasers*, New York: John Wiley and Sons, 1988, pp. 523-524.
8. Orazio Svelto, *Principles of Lasers*, 4th Ed., New York: Plenum Press, 1998, p. 174.
9. Vittorio Magni, "Resonators for solid-state lasers with large-volume fundamental mode and high alignment stability," Applied Optics 25, 1 (1 January 1986), pp. 107-117.
10. D. C. Hanna, C. G. Sawyers, M. A. Yuratich, "Telescopic resonators for large-volume TEM_{00}-mode operation," *Opt. and Quant. Elect.* 13 (1981), pp. 493-507.
11. J. Steffen, J. P. Lörtscher and G. Herzinger, *IEEE J. Quant. Elect.* QE-8 (1972), pp. 359-362.
12. W. R. Sooy, "The Natural Selection of Modes in a Passive Q-Switched Laser," *App. Phys. Lett.* 7, 2 (15 July 1965) pp. 36-37.
13. Shalei Dong, Qitao Lü, Ion Lancranjan, "220 W average output power from a Q-switching Nd:YAG slab laser with a $LiF:F_2^-$ crystal," Optics *and Lasers Technology*, 25, 3 (1993), pp. 175-178.
14. W. deRossi *et al.*, "Mode-locking operation of a pulsed Nd:YAG laser with F_2^-: LiF color-center crystal in a dual configuration," *App. Opt.* 31,15 (20 May 1992), pp. 2719-2721.
15. Junewen Chen, I. K. Fu, and S. P. Lee, "$LiF:F_2^-$ as a high repetition rate Ng:YAG [sic] laser passive modulator," *App. Opt.* 29,18 (20 June 1990), pp. 2669-2674.

16. V. P. Chebotayev, S. I. Marennikov, and V. A. Smirnov, "Application of LiF Crystals with F_2^- Colour Centers," *Appl. Phys. B* **31** (1983), pp. 193-199.
17. Orazio Svelto, *Principles of Lasers*, 4th Ed., New York: Plenum Press, 1998, pp. 312-313.
18. H. Statz, G. A. deMars, and D. T. Wilson, "Problem of Spike Elimination in Lasers," *Journal of App. Phys.* **36**, 5 (May 1965), pp. 1510-1514.

Future Direction

The laser described in this report will be used in SRRS experiments as described by Dr. Timothy Pritchett elsewhere in this program review report. Furthermore, if we are able to regain the pulse modulation, we intend to pursue the idea that the modulation could be limited to the first pulse of a multiply Q-switched pulse train.

Selected Publications and Conference Presentations: None

Cadet Publications and Presentations

CDT Dixon T. Brockbank and CDT Brandon S. Woll, "Construction of a Q-Switched, Nd:YAG Laser with Telescopic Resonator," Conference presentation at Rochester Symposium for Physics Students XX, 2 May 2000.

Cadet Involvement

1. CDT Dixon T. Brockbank, Class of 2000, Fall '99 – Spring '00, "Construction of a Q-Switched Nd:YAG Laser with Telescopic Resonator," Cadets Brockbank and Woll did most of the actual construction of the laser and characterization of its output. Starting with a laser head and parts from old lasers, they learned and followed the design of the telescopic resonator. Particular challenges were in increasing mechanical stability, doing experiments to understand the 4 – 9 ns modulation, developing an expertise in optimizing and aligning the laser, and figuring out the electronics to install the amplification system.

2. Fall '99 – Spring '00, "Construction of a Q-Switched Nd:YAG Laser with Telescopic Resonator," Cadets Brockbank and Woll did most of the actual construction of the laser and characterization of its output. Starting with a laser head and parts from old lasers, they learned and followed the design of the telescopic resonator. Particular challenges were in increasing mechanical stability, doing experiments to understand the 4 – 9 ns modulation, developing an expertise in optimizing and aligning the laser, and figuring out the electronics to install the amplification system.

Collaboration

None

Augustus Way Fountain III

Military Rank: Major

Branch: Chemical Corps /Academy Professor

Home Address:
501-H Merritt Road
West Point, NY 10996
(914) 446-9852

Office Address:
Department of Chemistry
United States Military Academy
West Point, New York 10996-5000
(914) 938-8624/3765
(914) 938-3062/2235 (FAX)

Email: augustus-fountain@usma.edu

EDUCATION:

Ph.D.   The Florida State University, Tallahassee, Florida
Major: Analytical Chemistry, 1997
Dissertation Advisor: Charles K. Mann
Dissertation Title: "Abscissa Calibration and Transfer for the Development of Instrument Independent Raman Spectra"

M.S.   The Florida State University, Tallahassee, Florida
Major: Analytical Chemistry, 1994
Thesis Advisor: Thomas J. Vickers
Thesis Title: "The Fourier Transform Approach to Raman Spectroscopy"

B.S.   Stetson University, DeLand, Florida
Major: Chemistry, 1985
Research Advisor: Edwin Coolidge
Research Title: "Application of Differential Pulse Anodic Stripping Voltammetry for the Determination of Selected Heavy Metals"

RESEARCH INTERESTS:

Analytical Chemistry: Vibrational Spectroscopy, Laser Spectroscopy, Chemometrics and Electrochemistry. My primary interests involve the development of novel methodologies, especially those using optical spectroscopy, for qualitative and quantitative analysis to solve difficult chemical problems. I am especially interested in the coupling of vibrational spectroscopy (both infrared and laser Raman spectroscopy) and optical imaging to gather molecular information remotely.

THERMAL AND UV LASER PYROLYSIS OF THE POLYIMIDE PMDA-ODA: ANALYSIS OF THE GASEOUS PRODUCTS BY TIME-RESOLVED AND DISCRETE INFRARED SPECTROSCOPY

CPT RAYMOND L. WAGNER AND MAJ AUGUSTUS W. FOUNTAIN III

Photonics Research Center and Department of Chemistry,

United States Military Academy,

West Point, NY 10996, USA

E-mail:augustus-fountain@usma.edu

Thermal and UV-laser pyrolysis of a thin film polymer (Kapton®) was studied to determine the gaseous products evolved and to elucidate a potential mechanism for decomposition. Thermal pyrolysis covered a temperature range from 800 to 1300 °C in 100 degree increments. Non-ablative laser pyrolysis was conducted using a continuous wave (cw) Argon ion laser at 363.6 nm. The results from the UV-laser pyrolysis show that the principal gaseous products evolved are CO, CO_2, C_2H_2, H_2NNH_2, CH_4 and HCN. The only gaseous products observed in the thermal pyrolysis study are CO and CO_2 with the principle component of thermal pyrolysis being carbon monoxide. While the amount of carbon dioxide evolved was relatively constant, the concentration of carbon monoxide increased with temperature. These results help provide essential information for the analysis of the chemical properties of the commercial polyimide Kapton and a better understanding of the polymer carbonization process.

1 Introduction

A great deal of research on the pyrolysis of the polymer, PMDA-ODA (Kapton®) figure 1, has been accomplished over the past 30 years. The Photonics Research Center has been studying the transforming effects of ultraviolet laser radiation on the polyimide PMDA-ODA since the early 1990's.[1,2,3] In these earlier works it was shown that when the surface of a thin film of Kapton was irradiated with a UV laser it could be carbonized and that the carbonization process was dependent on laser intensity and the atmosphere. The resulting carbon surface is reminiscent of pyrolytic glassy carbon and while Kapton is an electrical insulator the irradiated portion conducts electricity. Its electrochemical properties were further compared to both platinum and commercially available glassy carbon electrodes. [4] This phenomenon is unique to the polyimide Kapton and the study of the carbonization process continues to be of great interest.

While previous results were demonstrated, little was understood about the mechanism(s) that lead to the carbonization process. We believe that the degradation process brought on by the absorption of ultraviolet light is due in part to a thermal process. The impetus of this work was to gain further insight into the carbonization mechanism(s) and attempt to discriminate between steps that are generally thermal or photochemical in nature. In this series of experiments the object was to determine and compare the results of thermal pyrolysis and UV laser irradiation of the film. In order to determine the exact mechanism of the carbonization of Kapton, an airtight cell was built to collect discrete and continuous IR data. During the discrete analysis, the gaseous products were transferred after UV laser carbonization into a three-meter white cell using a custom manufactured vacuum line and
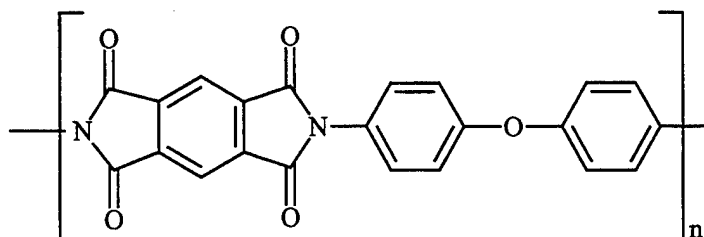
Figure 1. Structural Diagram of PMDA-ODA, Kapton®

then analyzed. For the time-resolved study, a constant flow of high purity argon gas swept the gaseous products out of the irradiation cell to the FT-IR spectrometer.

The UV laser irradiation of the polyimide film resulted in gaseous products consisting of CO, HCN, C_2H_2, CH_4, H_2NNH_2 and CO_2. The only gaseous products observed in the thermal pyrolysis study were CO and CO_2 with the principal component of thermal pyrolysis being carbon monoxide. These results illustrate the differing products seen from the UV irradiation and thermal pyrolysis of Kapton. The gaseous products generated through laser carbonization have led to several theories of the mechanism for the breakdown of Kapton. One mechanism proposes that CO is the first product produced in the irradiation.[1] Our results appear to confirm this and indicate that the generation of CO is a thermal process and not characteristic of UV irradiation.

2 Experimental

2.1 Thermal Pyrolysis:

Commercial Kapton HN in 125 μm thick films was obtained from DuPont. The film was cut into small segments, cleaned, and weighted before irradiation or thermal pyrolysis. Thermal pyrolysis of the polyimide film was conducted in a transmission condensate cell using a PY-2 Pyrolyzer (SpectraTech, Inc.). We modified the cell by replacing the NaCl windows with ZnSe and improved the seal to allow us to evacuate the cell. The temperature range for pyrolysis was mechanically controlled from 800 to 1300 °C and timed from 0 to 10 seconds. The gaseous products were observed directly with an FT-IR spectrometer (Midac, Inc.). Spectra were collected from 600 to 4000 cm^{-1} at 4 cm^{-1} resolution. For these measurements at least 64 co-added spectra were acquired to achieve an adequate signal-to-noise ratio.

2.2 UV Irradiation:

The UV laser excitation was conducted in a custom cell manufactured in house. A Coherent INOVA 200-20, operating between 350 - 380 nm multiline UV, provided the cw laser radiation (TEM_{00}). With these optics, most of the laser power is generated by the 363.3 nm line. The output power averaged 600 mW at the sample. A General Scanning, DE2000 Controller and XY mirror stage, Model E00-Z2173, provided precision control of the laser beam. A 200 mm focal length lens produced a spot size of approximately 100 mm. There was no attempt to correct the focus as the beam scanned because the total beam travel was less than 1 cm. An HPGL Conversion Utility, provided by Coherent, sent the appropriate coordinates to the DE2000 for the raster pattern used to etch the surface of the polyimide. A

mechanical shutter also under the control of the DE2000 allowed precise starting and stopping of the beam.

For the time-resolved study, the evolved gases were first generated in the irradiation cell and then transferred to a three-meter gas cell (Infrared Analysis, Inc.). Argon gas continuously flowed through the cell and across the polymer film at a rate of 100 ml/min. An outlet tube carried the argon and evolved gases into the three-meter cell inside the MIDAC FT-IR spectrometer. A small amount of argon gas was also used as a continuous purge for the FT-IR spectrometer. Spectra were collected from 600 to 4000 cm^{-1} at 4 cm^{-1} resolution. 50 individual spectra were created by co-adding 5 spectra at 30-second intervals.

3 Discussion

3.1 Thermal Pyrolysis:

By analyzing the gaseous products generated by thermal pyrolysis and comparing them to those generated during UV laser irradiation, we hoped to gain further understanding of the degradation patterns in the polyimide Kapton. The mechanical limits of the pyrolyzer prevented us from going beyond 1300 °C. At 800 °C the Kapton began to show significant degradation and observable generation of CO and CO_2. Over the 500 degree range that was investigated, a relative increase in the amount of CO generated with temperature was measured. (Figure 2) While it was difficult to calibrate the transmission condensate cell for
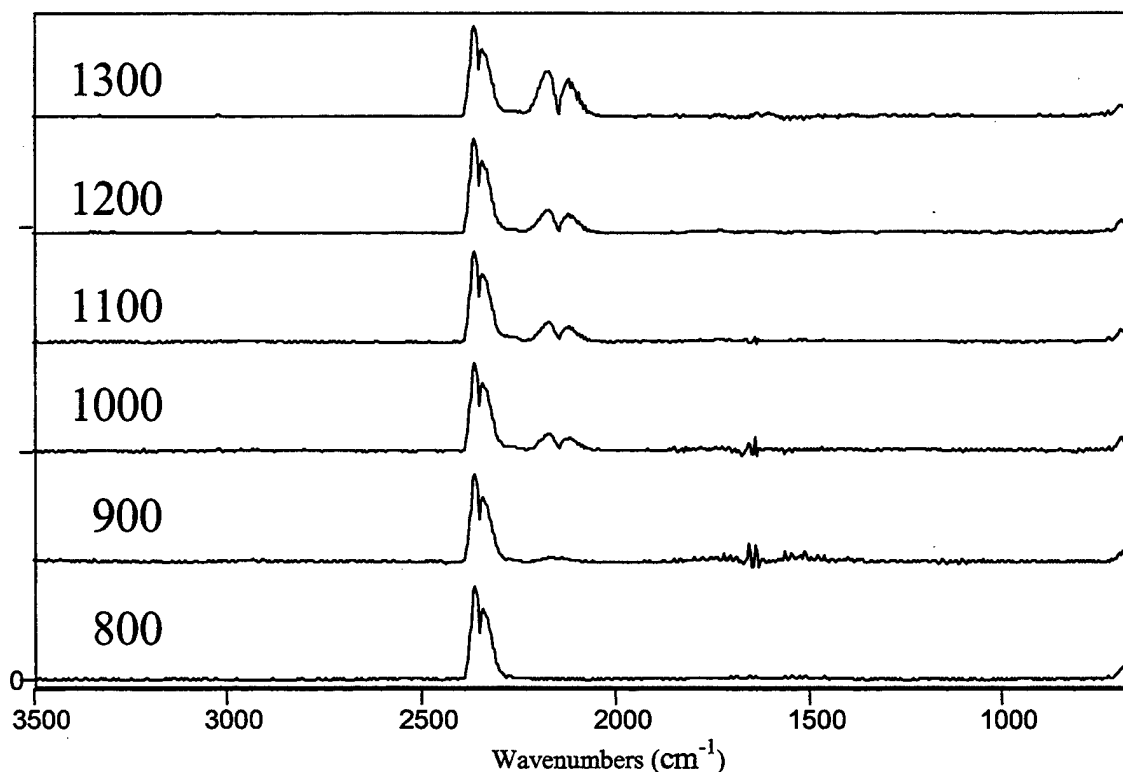

Figure 2. Infrared Absorption Spectra from Thermal Pyrolysis

either CO_2 and CO, the observed increase loss of mass in the film correlated with an increase in integrated band intensity for CO.

Although thermal pyrolysis produced physical changes to the film it did not carbonize the surface. The Kapton lost its flexibility and color throughout the film, in stark contrast to laser irradiation. While laser irradiation carbonizes approximately the top 25 to 50 µm of the surface, the remainder of the film retains its flexibility and physical properties. During thermal pyrolysis, a varnish like appearance was also observed on the surface of the polymer film. This effect is similar to that reported by Smith, *et al* during the pyrolysis of polyphenyl ether lubricants.[5]

3.2 *UV Laser Irradiation:*

Abstract factor analysis was applied to the time resolved data collected during the flow through experiment in order to determine the number of gaseous components and assist in their identification. Factor analysis is a matrix decomposition procedure that treats each spectrum as a vector and partitions the variance in the spectra into a series of abstract factors that are mutually orthogonal. The mathematical basis for factor analysis is sufficiently explained in the literature, notably by Malinowski.[6] Briefly, each spectrum represents a column vector in a data matrix D. Either premultiplying or postmultiplying the data matrix with its transpose forms the covariance matrix Z. Since both are equivalent strategies, we chose to form the covariance matrix as indicated in equation 1. The covariance matrix is then diagonalized in order to generate an abstract factor matrix C and the corresponding score matrix R (equation 2). The columns in C are the *eigenvectors* of D and constitute a mutually orthonormal set. The largest amount of variance in the spectra is contained in the first abstract factor and is essentially the average spectrum over the entire set. The next largest amount of variance is contained in the second abstract factor, with the remaining variance likewise being contained in subsequent abstract factors.

$$Z = DD^T \qquad (1)$$
$$D = RC \qquad (2)$$

The more common method of decomposing the data matrix and extracting the abstract factors is accomplished through singular value decomposition (SVD). Here, D is an $m \times n$ matrix whose number of rows m is greater than the number of columns n. The decomposition rewrites the matrix D into the product of a column-orthogonal $m \times n$ matrix U, an $n \times n$ diagonal matrix S, and the transpose of an $n \times n$ orthogonal matrix V. Using the standard notation, the data matrix is expressed as

$$D = USV^T . \qquad (3)$$

In this form, U and V are orthonormal matrices that contain eigenvectors spanning the row and column space of D. S is a diagonal matrix that contains the square root of the eigenvalues.[7] The matrix representation in equation 2 is readily obtained from equation 3 by noting that

$$US = R \qquad (4)$$
$$V^T = C . \qquad (5)$$

The number of significant abstract factors was determined using the power spectra method described by Mann *et al.*[8] The first six abstract factors accounted for 86% of the total variance in the spectra with the remaining factors accounting for mostly noise. While these abstract spectra have no true physical meaning, they do account for the observed changes in the experimental data and indicate the presence of six major components. These

components were identified as CO, CO_2, HCN, CH_4, C_2H_2, and H_2NNH_2. (Figure 3) While target transformation of reference spectra of these compounds with the abstract factors proved inconclusive, subtraction of these reference spectra left only noise and revealed no other components.

In an earlier work the gaseous products from the carbonization process were identified as CO, HCN, C_2H_2, and CO_2. It was further assumed that the amount of CO_2 was negligent and was mostly present in the background. We can no longer conclude this for two reasons. First, CO_2 was identified as a major component though abstract factor analysis. Second, in this series of time resolved experiments high purity argon was simultaneously used to sweep the gaseous components from the UV irradiation cell into the white-cell and continuously purge the FT-IR spectrometer. The subtraction of subsequent background scans revealed only noise, so the presence of CO_2 in the spectra can only be accounted for by it being generated during the carbonization process.

Further analysis of the time resolved data showed that the initial gaseous products generated are CO, CO_2, C_2H_2, and HCN. After further irradiation, CH_4 and H_2NNH_2 appear in the spectra and increase at the same rate as the other components. It is not clear if these components are generated as a result of further decomposition of the polyimide or binders used in the commercial production of Kapton. The late appearance in the spectra may also be a result of there initially not being enough of a concentration to observe the bands of either component. In either case, both CH_4 and H_2NNH_2 are confirmed components in the spectra through abstract factor analysis and cannot be discounted.

3.3 Molecular Modeling:

Kapton has numerous electronic absorption bands throughout the ultraviolet spectrum. Many of these bands are due to the various conjugated π orbital systems throughout the polymer. In order to gain an appreciation of what were the most probable electronic transitions to initiate carbonization, MOPAC and Gaussian 98 were used to calculate the charge density,
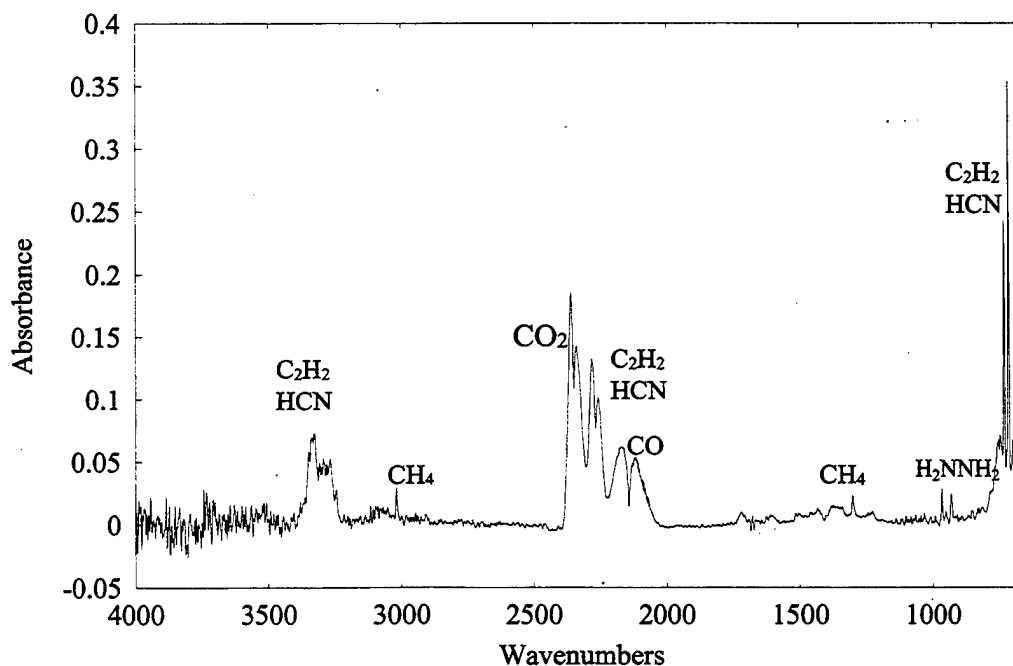

Figure 3. Infrared Absorption Spectrum of Gaseous Products from UV Laser Irradiation

electrostatic potential and molecular orbital energies for PMDA-ODA oligamers of varying length.[9] Figures 4.a and 4.b show the highest occupied molecular orbital (HOMO) and the lowest unoccupied molecular orbital (LUMO) for a segment containing two repeating units of the polymer. As shown here, the HOMO spans the phenyl ether moiety of the repeating unit, with the majority of the density on the phenyl rings. The LUMO spans the imide portion of the repeating unit, primarily with charge density in the anti-bonding orbitals of the sigma bonds between the carbonyl carbons and the phenyl ring. The energy difference between these two orbitals was calculated at 6.6 EV $(1.05 \times 10^{-18}$ J). While this energy is more than the energy of a photon at 363 nm, these results allow for the discussion for a potential transfer of charge from the phenyl moiety that would

Figure 4. a. Highest Occupied Molecular Orbital (HOMO) of PMDA-ODA b. Lowest Unoccupied Molecular Orbital (LUMO) of PMDA-ODA

initiate the polymer degradation. While this might account for the generation of carbon monoxide, it does not provide any further explanation of how the carbon network is formed.

4 Conclusion

Our interests in the laser induced carbonization of Kapton is directed toward developing polymer based electrically conducting networks. This effect appears to be unique for Kapton and understanding the mechanism offers the possibility for the further development of these carbonized surfaces as electrical devices. By gaining further insight into the carbonization mechanism we hope to determine other existing polymeric candidates or suggest new polymeric materials that would also produce conducting carbon networks without the generation of hazardous products such as HCN.

Previous works by Srinivasan et al suggested a carbonization mechanism that accounted for the generation of CO from the polyimide Kapton. However, there was no explanation provided for the generation of the other gaseous components or the role of UV laser excitation into the carbonization process. While our data supports the initial step in the proposed mechanism, the generation of CO appears to be a thermal process and not necessarily a characteristic of UV laser irradiation. Molecular orbital calculations indicate a

possible electronic transition that would account for the generation of CO and initiation of the carbonization reaction. However, the energies involved are greater than those being presently used for laser irradiation.

Based on our data we can also no longer dismiss the presence of CO_2 in the carbonization products. Abstract factor analysis of the time resolved data indicates that CO_2 is a major component. While the generation of CO is easily understood through the release of the carbonyl group by breaking of the C—N and C—C bonds in the imide ring, the mechanism that generates CO_2 is not readily apparent.

5 Acknowledgements

6 References

1. R. Srinivasan, R. R. Hall, W. D. Wilson, W. D. Loehle, and D. C. Allbee Chem. Mater., 6 (7), 889 (1994).
2. R. Srinivasan, R. R. Hall, W. D. Wilson, W. D. Loehle, and D. C. Allbee Synthetic Metals, 66, 301 (1994).
3. R. Srinivasan, R. R. Hall, W. D. Wilson, W. D. Loehle, and D. C. Allbee J. Appl. Phys., 78 8, 4881 (1995).
4. G. H. Wynn, and A. W. Fountain III J. Electrochem. Soc., 144 (11), 3769 (1997).
5. R. J. Byrd, C. S. Saba, and H. A. Smith Tribology Transactions, 35 (4), 667 (1992).
6. E. R. Malinowski, Factor Analysis in Chemistry, (John Wiley & Sons, Inc., New York, 1991), Chap. 4, pp. 34 - 39.
7. 10 William H. Press, Saul A. Teukolsky, William T. Vetterling, Brian P. Flannery Numerical Recipes in C, 2nd Ed., (Cambridge University Press, New York, 1992) Chap. 2, p.59.
8. C. Shen, T. J. Vickers, and C. K. Mann, J. Chemometrics, 5, 417-434 (1991).
9. Gaussian 98, Revision A.7, M. J. Frisch, G. W. Trucks, H. B. Schlegel, G. E. Scuseria, M. A. Robb, J. R. Cheeseman, V. G. Zakrzewski, J. A. Montgomery, Jr., R. E. Stratmann, J. C. Burant, S. Dapprich, J. M. Millam, A. D. Daniels, K. N. Kudin, M. C. Strain, O. Farkas, J. Tomasi, V. Barone, M. Cossi, R. Cammi, B. Mennucci, C. Pomelli, C. Adamo, S. Clifford, J. Ochterski, G. A. Petersson, P. Y. Ayala, Q. Cui, K. Morokuma, D. K. Malick, A. D. Rabuck, K. Raghavachari, J. B. Foresman, J. Cioslowski, J. V. Ortiz, A. G. Baboul, B. B. Stefanov, G. Liu, A. Liashenko, P. Piskorz, I. Komaromi, R. Gomperts, R. L. Martin, D. J. Fox, T. Keith, M. A. Al-Laham, C. Y. Peng, A. Nanayakkara, C. Gonzalez, M. Challacombe, P. M. W. Gill, B. Johnson, W. Chen, M. W. Wong, J. L. Andres, C. Gonzalez, M. Head-Gordon, E. S. Replogle, and J. A. Pople, Gaussian, Inc., Pittsburgh PA, 1998.

Future Direction

Future endeavors include a comparison of the effects of CO_2 concentration and temperature on bandshape.

Selected Publications and Conference Presentations

1. Stephen F. Dinetz, Elliot J. Bird, Raymond L. Wagner, and Augustus W. Fountain III "Thermal and UV Laser Pyrolysis of the Polyimide PMDA-ODA: Analysis of the Gaseous Products by Time-Resolved And Discrete Infrared Spectroscopy" Proceedings of the International Symposium on Polyimides and Other High Temperature Polymers, Newark, NJ, December 1999.
2. Wynn, Gary H.; Fountain, Augustus W. III "Development and Characterization of Electrochemical Devices Using UV-Laser Induced Carbonization of Polyimide Films", *J. Electrochem. Soc.*, 144, 11, pp. 3769-3772.
3. Wagner, R. L; Fountain, Augustus W. III "Thermal and UV-laser Pyrolysis of Kapton: A Comparative Study", International Symposium on Polyimides and Other High Temperature Polymers, Newark, NJ, December 1999.
4. Wynn, Gary H.; Cuadrado, Juan A.; Fountain, Augustus W. III; Allbee, David C. "UV-Laser Induced Carbonization of Polyimides: Development of Patternable Conducting Carbon Networks and Electrochemical Characterization", 20th Army Science Conference, Norfolk, Virginia, July 1996, paper B-03.
5. Wynn, Gary H.; Fountain, Augustus W. III; Cuadrado, Juan A.; Allbee, David C. "Development and Electrochemical Characterization of UV-Lased Induced Conducting Carbon Networks on Polyimides", ACS Spring National Meeting, New Orleans, Louisiana, 1996, paper 566.
6. Fountain, Augustus W. III; Wynn, Gary W.; Cuadrado, Juan A.; Allbee, David C. "Laser Induced Carbonization of Polyimides: Electrochemical Characterization", PITTCON, Chicago, Illinois, March 1996, paper 377P.

Cadet Publications and Presentations

1. Bird, Elliot J. "Thermal and UV-laser Pyrolysis of Kapton", Mid-Hudson Section of the American Chemical Society Undergraduate Poster Symposium, New Paltz, New York, May 1999, paper 14.

Cadet Involvement

1. CDT Elliot J. Bird, c/o 1999, CH400, CH489-490.
2. CDT Stephen F. Dinetz, c/o 2000, CH489-490.

Collaboration

None

THE USE OF MULTIVARIATE ANALYSIS TO DETERMINE TEMPERATURE FROM LOW RESOLUTION INFRARED SPECTRA OF CARBON DIOXIDE

MAJ AUGUSTUS W. FOUNTAIN III

Department of Chemistry and Photonics Research Center,

United States Military Academy, West Point, New York 10996
E-mail: augustus-fountain@usma.edu

The remote optical monitoring of gaseous contaminants is important for both military and industrial applications. An important parameter for quantifying chemical species and for predicting plume dynamics is the temperature. While in some industrial monitoring situations it may be practical to independently measure the temperature of stack emissions, for compliance monitoring and military chemical reconnaissance a remote optical means of estimating gas plume temperature is required. It was noticed that the band shape of low resolution spectra of carbon dioxide in equilibrium with an exhaust plume was very sensitive to temperature. Spectra of carbon dioxide were acquired under controlled laboratory conditions in 5 degree increments from 20 - 200 °C. Various multivariate models were used to predict the temperature. It was found that partial least squares was unable to effectively model the simultaneous changes in amplitude and bandwidth with temperature. However, Principal Component Regression (PCR) was found to be well correlated with temperature and allowed cross-validated prediction within 4% error.

1 Introduction

The remote sensing needs for both Force XXI and Army After Next, as outlined in Army Vision 2010, must meet the Nation's goal of total information dominance on the battlefield.[1] It is important that this technology provides our forces with an unprecedented real-time battlefield situational understanding of the extent and location of any chemical contamination. This technological need has parallel applications with governmental agencies charged with ensuring compliance with environmental laws and treaties governing the production of weapons of mass destruction (WMD).[2]

Current military detection devices use a passive infrared device that detects a chemical agent by monitoring changes in the vibrational spectrum of the atmosphere. They are unable to reliably determine which agent is present and can not determine its relative concentration. To meet future needs, an acceptable chemical standoff detector must both detect and quantify chemical warfare agents. An important parameter for quantifying chemical species and for predicting plume dynamics is temperature. While in some industrial monitoring situations it may be practical to independently measure the temperature of stack emissions, for compliance monitoring and military chemical reconnaissance a remote optical means of estimating gas plume temperature is required.

When using Fourier transform infrared (FT-IR) spectroscopy to monitor gases, spectra are normally acquired at high resolution to accommodate the large degree of rotational band overlap and deviations from Beer's Law. Temperature measurement of gaseous emissions reported in the literature by Griffiths *et al.* relied on measuring the Boltzmann distribution of rotational lines in high resolution FT-IR emission spectra.[3] However, acquiring gas phase spectra at low resolution would provide the advantages of higher signal to noise ratio and faster spectral acquisition.

It was noticed in field measurements that the band shape of carbon dioxide in equilibrium with an exhaust plume was very sensitive to temperature. We then postulated that multivariate algorithms might be capable of determining the temperature of a gaseous mixture based solely on these changes in the band shape. Our initial efforts were directed toward applying partial least squares (PLS) to the analysis, because it has been effectively used to model the response of many linear and nonlinear relationships.

2 Experimental

Spectra of carbon dioxide were acquired as mixtures of 200 ppm carbon dioxide in nitrogen. The gases were mixed and transferred into a 10 meter variable path length cell (Graseby Specac) via a custom manufactured vacuum manifold (Ace Glassware). The pressure in the cell was maintained at atmospheric pressure for all measurements. The path length of the cell was calibrated and set to 5.28 meters.

The gas cell was equipped with a heating jacket that allowed for temperature control from ambient to 200 °C. The gases were allowed to come into thermal equilibrium with the cell prior to acquiring spectra. The spectrum of the evacuated cell, heated to the appropriate temperature, was used as the background spectrum. Three independent spectra of CO_2 mixtures were acquired from 20 °C to 200 °C in 5 degree increments. One set of spectra was used for the calibration phase of the PLS algorithm and further abstract factor analysis; a second set was used for the prediction phase of the PLS algorithm; and the third was reserved for cross validation analysis. All spectra were recorded at 4 cm^{-1} resolution on a Midac (Irvine, CA) M2000 series spectrometer using GRAMS/32 (Galactic, Inc.). Prior to analysis, spectra were baseline corrected, windowed from 2200 cm^{-1} to 2500 cm^{-1} to isolate the v_3 band of carbon dioxide, and normalized to unit area. Partial least squares, factor analysis, and regression analysis were accomplished using MathCad 8.0 Professional (Mathsoft, Inc.). The PLS1 algorithm was programmed using MathCad as outlined by Haaland and Thomas.[4] Principal Component Regression (PCR) was performed as described by Wentzell, Andrews, and Kowalski.[5]

3 Results and Discussion

The spectra in Figure 1 highlight the observed changes in bandshape for CO_2. Between 20 °C and 100 °C, the greatest change in the spectrum occurs in the intensity of the P and R branches of the vibrational-rotational envelope. While the greatest change in intensity occurs in the R branch (43%), the reduction in the intensity of the P branch coincides with the appearance of a small shoulder at 2330 cm^{-1} and a slight increase in the full width at half height (FWHH). For temperatures between 100 °C and 200 °C, there is only a 6% decrease in the maximum intensity compared to a 15% increase in the FWHH. These changes coincide with the depopulation of molecules in states with low rotational quantum numbers and their subsequent repopulation into states with higher rotational quantum numbers as the temperature increases.

3.1 Partial Least Squares Regression.

Partial least squares is a multivariate analysis tool capable of determining the dependent factors in a linear relationship; most often concentration measured from absorbance. The

PLS algorithm is closely related to other multivariate methods, such as classical least squares and factor analysis, but has several advantages. First, it is a full spectrum technique and is not dependent on choosing the proper band segment for the analysis. Second, only the concentrations ·of the components of interest are included in the calibration. Since the algorithm generates scores that are orthogonal, the presence of other components, even if known, does not interfere with the analysis.
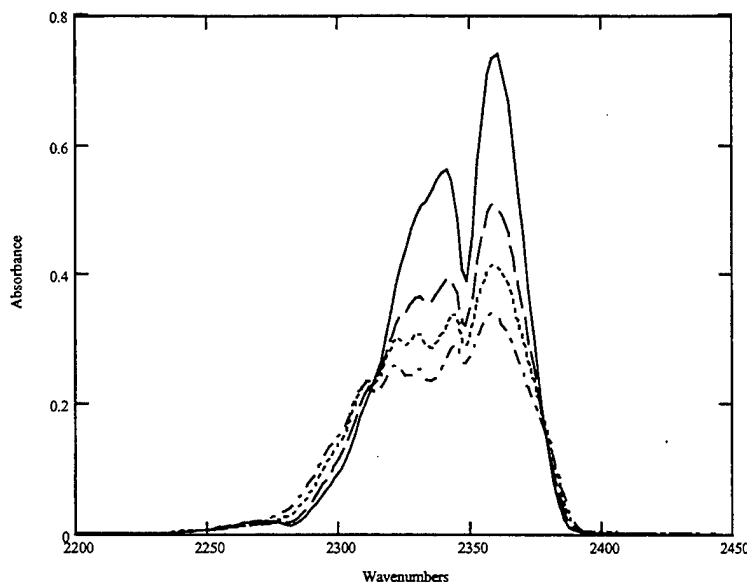

Figure 1. Normalized spectra of the v_3 band of carbon dioxide, from 2200 ... 2500 cm^{-1} at 20 °C (—), 80 °C (——), 140 °C (···), and 200 °C (—·—).

The PLS algorithm can be broken down into two major phases: spectral decomposition and prediction. The spectral decomposition phase begins with the assumption that there is a linear dependence on the absorbance at each wavenumber to some factor, in our case temperature. In matrix notation, the model for m calibration standards, n observed wavenumbers and l components is

$$A = CK + E \qquad (1)$$

where A is a matrix of $m \times n$ measured spectra, C is the $m \times l$ factor matrix, K is the $l \times n$ matrix representing the l individual pure component spectra at n wavenumber values, and E is the $m \times n$ matrix of spectral errors. The observed low resolution spectrum is the linear combination of the intensities from all rotational states. The underlying assumption was that PLS would model the bandshape changes with temperature, where the intensity of each rotational line is proportional to the Boltzmann population in each rotational state at each temperature. So in our case C is the matrix of measured temperatures and K is a matrix representing a hypothetical spectrum for a closely grouped band of rotational transitions.

In PLS, spectral decomposition creates a new orthogonal coordinate system of basis vectors.

$$A = TB + E \qquad (2)$$

The matrices, A and E, are the same as in equation 1, but B is now a $h \times n$ matrix of loading vectors and T is a $m \times h$ matrix of scores in the new coordinate system. Here B is a row matrix of eigenvectors of $A^T A$ and T is a column matrix of eigenvalues of AA^T. The calibration, or spectral decomposition, phase is an iterative one. The predicted error sum of squares (PRESS) is used as a metric to determine the number of loading vectors required for the model. PRESS is defined as:

$$PRESS = \sum_{i=1}^{m} (\hat{c}_i - c_i)^2 \qquad (3)$$

8-3

where m is the number of samples, $\hat{c}_i$ is the estimated factor from the model and c_i is the actual factor. The number of loading vectors that produce the smallest PRESS value are then used in the prediction step.

During the prediction phase, the intensities in the sample spectrum are correlated with the loading vectors obtained in the spectral decomposition phase. After mean centering the sample spectrum, the quantity of interest is iteratively estimated using the loading vectors and scores determined previously. At each step the variance is determined and substituted back into the regression model for the sample spectrum until the optimal number of loading vectors are used.[4]

Leave-out-one cross-validation was utilized to generate a regression between known and predicted temperatures using PLS. The regression curve appeared to have two separate linear regions. Separate regressions were generated from spectra corresponding to CO_2 at 20 °C to 110 °C and 110 °C to 200 °C. The first regression was fairly linear ($R = 0.974$) and corresponded to 8% error from the known temperature. While the second regression was also linear ($R = 0.964$), it deviated significantly from the regression up to 100 °C and likewise corresponds to 25% error.

Partial least squares analysis was applied separately to the spectra of CO_2 at temperatures less than 100 °C and greater than 100 °C. Separate regressions based on leave-out-one cross-validation showed improved correlation and prediction for each subset. This affirmed to us that PLS was unable to model the simultaneous changes in intensity and bandwidth observed in the CO_2 spectra.

3.2 Factor Analysis.

Factor analysis was applied to partition the variance in the spectra into a series of abstract factors that are mutually orthogonal. The mathematical basis for factor analysis is sufficiently explained in the literature, notably by Malinowski.[6] Briefly, each spectrum represents a column vector in a data matrix **D**. Either premultiplying or postmultiplying the data matrix with its transpose forms the covariance matrix **Z**. Since both are equivalent strategies, we chose to form the covariance matrix as indicated in equation 4. The covariance matrix is then diagonalized in order to generate an abstract factor matrix **C** and the corresponding score matrix **R** (equation 5). The columns in **C** are the *eigenvectors* of **D** and constitute a mutually orthonormal set. The largest amount of variance in the spectra is contained in the first abstract factor and is essentially the average spectrum over the entire set. The next largest amount of variance is contained in the second abstract factor, with the remaining variance likewise being contained in subsequent abstract factors.

$$\mathbf{Z} = \mathbf{D}\mathbf{D}^T \qquad (4)$$
$$\mathbf{D} = \mathbf{R}\mathbf{C} \qquad (5)$$

The more common method of decomposing the data matrix and extracting the abstract factors is accomplished through singular value decomposition (SVD). Here, **D** is an $m \times n$ matrix whose number of rows m is greater than the number of columns n. The decomposition rewrites the matrix **D** into the product of a column-orthogonal $m \times n$ matrix **U**, an $n \times n$ diagonal matrix **S**, and the transpose of an $n \times n$ orthogonal matrix **V**. Using the standard notation, the data matrix is expressed as

$$\mathbf{D} = \mathbf{U}\mathbf{S}\mathbf{V}^T . \qquad (6)$$

In this form, **U** and **V** are orthonormal matrices that contain eigenvectors spanning the row and column space of **D** respectively. **S** is a diagonal matrix that contains the square root of the eigenvalues.[7] The matrix representation in equation 5 is readily obtained from equation 6 by noting that

$$US = R \qquad (7)$$
$$V^T = C . \qquad (8)$$

Factor compression seeks to remove variance in the data matrix by discarding abstract factors associated with noise and retaining only the abstract factors associated with the largest *eigenvalues*. The number of significant abstract factors was determined using the power spectra method described by Mann *et al.*[8] Three significant abstract factors were identified (Figure 2). While these abstract spectra have no true physical meaning, they do account for the observed changes in the experimental data. The second and third abstract factors nearly take on the form of a first and second derivative. The second abstract factor has negative peaks consistent with the maxima of the P and R branches and zero crossings that bound the lower rotational states of CO_2. The third abstract factor has positive peaks consistent with the maxima of the P and R branches and at the far edges of the vibrational-rotational envelope. Since the remaining abstract

Figure 2. 1st (bottom), 2nd (middle), and 3rd (top) Significant Abstract Factors Derived from the Set of Carbon Dioxide Spectra.

factors were insignificant, all of the spectral variance associated with the depopulation and repopulation of rotational states within the CO_2 spectra are encapsulated in these three abstract factors.

3.3 Principal Component Regression.

The object of factor analysis is to generate a series of orthogonal vectors that account for the greatest amount of variance in the original data. All of the original spectra can then be represented as some linear combination of these abstract factors. The projection of a spectral vector on one of the orthogonal abstract factors is a measure of that factor's variance and is proportional to the corresponding eigenvalue.[9] The projection is calculated by forming the dot or inner product of the spectrum and the abstract factor. The cosine between these two vectors is in a sense, the normalized least squares estimate as described by Lawton and Sylvestre.[10]

In PCR, the regression is generated from the projection of the spectra onto the reduced set of scores. After factor compression, the data matrix **D** can be represented by the product of the reduced scores and loadings,

$$D = \tilde{U}\tilde{S}\tilde{V}^T + E \qquad (9)$$

where **E** is a matrix of spectral errors. The regression model is similar to inverse least squares, except in PCR the regression vector that is generated relates the reduced set of scores, $\widetilde{U}\widetilde{S}$, to the quantity of interest. In the prediction step, the scores for the unknown spectrum are found by forming the product of the spectrum and the reduced matrix of loadings, $\widetilde{V}$. The unknown quantity, in our case temperature, is then given by forming the product of the previously found scores and the regression vector. One can easily form another regression vector that conveniently combines both regression and prediction steps. This vector is then directly multiplied to a sample spectrum, as shown in equation 10, to obtain the unknown quantity.

$$t_{unk} = a_{unk} \widetilde{V}\widetilde{S}^{-1}\widetilde{U}^T t \qquad (10)$$

In this notation, **a** is the unknown spectrum and **t** is vector representing the known temperatures from the regression step.

Leave-out-one cross-validation was used to generate a series of linear regressions to successively determine the temperature of CO_2 from the omitted spectrum. The regression of predicted vs. known temperature is shown in Figure 3. Here the predicted temperatures are well correlated ($R = 0.997$) and represent an error of 4%.

Figure 3. Cross-validated Prediction Plot Based on Principal Component Regression of the First Three Abstract Factors.

3.4 Effect of Noise on Prediction.

In order to determine the robustness of this method, normally distributed random noise was added to the spectra to degrade its signal-to-noise ratio. Since the ratio of the R-branch maxima to the RMS noise in the original data set was greater than 1000:1, the signal-to-noise ratio was successively reduced in half from this value to a ratio of 1:1. Principal Component Regression and leave-out-one cross-validation were used to generate new regressions of predicted vs. known temperatures at each new signal-to-noise ratio.

The F-statistic as derived by Mark was used as a metric to determine when the regression became statistically insignificant.[11] Based on this statistic, the regression remained statistically significant at the 99% confidence level until the signal-to-noise ratio reached 30:1. The regression remained significant at the 97.5% confidence level until the signal-to-noise level dropped to 20:1 and then at the 90% confidence level when the signal-to-noise ratio was 10:1.

4 Conclusion

The estimation of temperature is an important parameter in the quantitative analysis of gaseous contaminates. In many situations, the remote acquisition of high resolution Fourier transform infrared spectra is impractical. While low resolution generally produces spectra
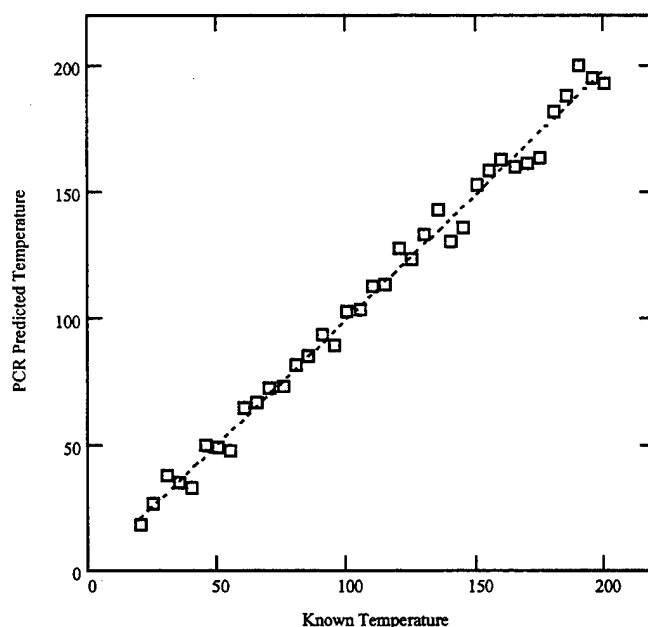
with a higher signal-to-noise ratio at faster acquisition times, the rotational fine structure typically used to determine the temperature of gases is lost. Therefore a multivariate means of analysis was needed to determine the temperature based only on the changes in observed bandshape.

Principal component regression (PCR) and partial least squares (PLS) are multivariate methods that combine the individual strengths of classical least squares and the inverse least squares. In this study however, it was shown that partial least squares analysis was unable to account for the simultaneous changes in band intensity and bandwidth observed in the CO_2 spectra. Because PLS generally assumes a linear relationship with the component of interest, the model attempts to generate loading vectors that account for the variance in a linear fashion. While the spectra exhibited a nearly linear decrease in the intensity from 20 °C to 100 °C, PLS was able to produce an acceptable regression. However once the change in bandwidth became the major source of variance in the spectra, the PLS model deviated significantly and appears to begin a new regression. Therefore, the PLS approach proved ineffective overall.

Like PLS, factor analysis successively partitions the variance in the data into an orthogonal set of basis vectors. In principal component regression (PCR), the projection of a spectral vector onto the coordinate system of orthogonal abstract factors is used as a least squares estimator of the variance for regression. In our case a regression model using the first three abstract factors was shown to be an effective estimate of the variance and well correlated with temperature. Regression based on leave-out-one cross-validation produced temperature estimates within 4% error of the known value. This regression was also shown to be robust even when the signal-to-noise ratio was poor.

From this study we conclude that PCR is a more effective multivariate analysis tool for determining the temperature of a gas from low resolution spectra. However because this study was based on laboratory data, we recommend further analysis with open path and field data trials before this method is incorporated into a remote optical sensing scheme.

5 Acknowledgements

6 References

1. GEN D. J. Reimer, Army Vision 2010 (U.S. Army, Washington, DC, 1996) p. 10.
2. T. L. Marshall, C. T. Chaffin, R. M. Hammaker, and W. G. Fateley, Environ. Sci. Technol., 28, 224A-232A (1994)
3. L. A. Gross, P. R. Griffiths, and J. N. P. Sun, "Temperature Measurement by Infrared Spectrometry", in Infrared Methods for Gaseous Measurements, J. Wormhoudt, Ed. (Marcel Deker, Inc., New York, 1985), Chap. 3, pp. 93 - 99.
4. D. M. Haaland and E. V. Thomas, Anal. Chem., 60, No. 11, 1193-1202 (1988).
5. P. D. Wentzell, D. T. Andrews, and B. R. Kowalski, Anal. Chem., 69, No. 13, 2299-2311 (1997).

6. E. R. Malinowski, Factor Analysis in Chemistry, (John Wiley & Sons, Inc., New York, 1991), Chap. 4, pp. 34 - 39.
7. William H. Press, Saul A. Teukolsky, William T. Vetterling, Brian P. Flannery Numerical Recipes in C, 2nd Ed., (Cambridge University Press, New York, 1992) Chap. 2, p.59.
8. C. Shen, T. J. Vickers, and C. K. Mann, J. Chemometrics, 5, 417-434 (1991)
9. A. Phatak and S. D. Jong, J. Chemometrics, 11, 311-338 (1997).
10. W. H. Lawton and E. A. Sylvestre, Technometrics, 13, No. 3, 617-632 (1971).
11. H. Mark, Spectroscopic Calibration (John Wiley & Sons, Inc., New York, 1991), Chap. 3, p. 97.

Future Direction

Future endeavors include a comparison of the effects of CO_2 concentration and temperature on bandshape.

Selected Publications and Conference Presentations

1. Szczepanski, Michael P.; Fountain, Augustus W. III "The Use of Multivariate Analysis to Determine Temperature from Low Resolution Infrared Spectra of Carbon Dioxide", *Appl. Spectrosc.*, 54 (2), 2000.
2. Fountain, Augustus W. III; Szczepanski, Michael P.; "The Remote Optical Detection of Gas Plume Temperature from Low Resolution Gas Phase Infrared Spectra of Carbon Dioxide", 27th Annual Meeting of the Federation of Analytical Chemistry and Spectroscopy Societies, Vancouver, British Columbia, October 1999, paper 701.
3. Fountain, Augustus W. III; Szczepanski, Michael P.; "The Remote Optical Detection of Gas Plume Temperature from Low Resolution Gas Phase Infrared Spectra of Carbon Dioxide", Northeastern Regional Meeting of the American Chemical Society, Potsdam, New York, June 1999, paper 164.

Cadet Publications and Presentations

1. Szczepanski, Michael P.; "The Remote Optical Detection of Gas Plume Temperature from Low Resolution Gas Phase Infrared Spectra of Carbon Dioxide", Mid-Hudson Section of the American Chemical Society Undergraduate Poster Symposium, New Paltz, New York, May 1999, paper 11.

Cadet Involvement

1. CDT Michael P. Szczepanski, c/o 1999, CH489-490. CDT Szczepanski won the Mid-Hudson ACS Undergraduate Research Award for 1999.

Collaboration

1. Dr. William G. Fateley, Professor of Chemistry, Kansas State University
2. Dr. Robert T. Kroutil, Principle Investigator, Edgewood Chemical and Biological Center, Maryland

PHOTOOXIDATIVE BLEACHING OF CHLOROPHYLLIN

MAJ AUGUSTUS W. FOUNTAIN III

Photonics Research Center and Department of Chemistry,
United States Military Academy,
West Point, NY 10996, USA
Email:augustus-fountain@usma.edu

Chlorophyllin, a water soluble, copper-containing porphyrin can be bleached rapidly in the light or slowly in the dark in a reaction which is oxygen dependent. Both the photo and the dark bleaching reactions are temperature dependent. Cyclic voltammetry measurements show that the copper in the bleached and non-bleached state remains in the +2 redox state and could be readily reduced. This would imply that there is no net oxidative change to the copper during the bleaching process. FT-IR absorption spectroscopy showed vibrations characteristic of a vinyl functionality disappeared upon bleaching. Aqueous solutions of chlorophyllin were not dialyzable through dialysis tubing of molecular weight cut-off, 6,000-8,000 molecular weight, indicative of an aggregate chlorophyllin micelle. Analysis of products by high performance liquid chromatography showed that the chlorophyllin mixture was more complex than originally anticipated and that two components were lost from the mixture upon photobleaching. One compound that is preferentially lost upon photobleaching has been identified by mass spectral analysis as Cu (II) chlorin e6.

1 Introduction

Reactions associated with photosynthesis have the potential to generate active oxygen intermediates such as $^xO_2^-$, H_2O_2, ^xOH, and $^1O_2$[1-3]. Whether generated through autoxidations of electron transport components [1-3] or directly through photosensitization by pigments [4-5], these intermediates carry the potential to destroy the chlorophyll molecule. In a previous study using chlorophyllin, the relatively stable, water-soluble, copper substituted porphyrin, we have shown that the photodestructive process involved oxygen, possibly a peroxide and could be efficiently prevented by the addition of reductants[6]. Earlier reports on the photodestruction of the highly sensitive chlorophyll molecule showed that photobleaching was an oxygen dependent process probably involving oxygenation[7-8]. In the case of chlorophyll, the products as well as reaction rates were dependent upon the solvent system used. When bleached colorless, the detected hydrophilic products of complete ring degradation include: glycerol, organic acids such as lactic, succinic, citric and malonic acids, as well as the amino acid, alanine[9].

The advantage of studying chlorophyllin is that the molecule is inherently more stable than chlorophyll and has the additional advantage of being water soluble. Moreover chlorophyllins are often used commercially in foods, detergents, deodorants and in the pharmaceutical and cosmetic industries [10-11]. We now report on further investigations on the photodestruction of chlorophyllin by examining the kinetics of decay and a preliminary analysis of the photobleached product.

2 Materials and Methods

2.1 Photobleaching of Chlorophyllin

The sodium salt of chlorophyllin was purchased from Sigma Chemical Co. (St. Louis, MO). Material was weighed under minimal light conditions and dissolved immediately prior to use in 50 mM potassium phosphate, pH 7.0. Typical sample concentrations were 0.88 mM and all solutions were kept in the dark in brown vials covered with aluminum foil prior to use.

Chlorophyllin samples (15 mL total volume) were placed in a 20 mL test tube immersed in a transparent temperature controlled water bath. Illumination was provided by a single 500 W quartz halogen bulb. Total radiation reaching the sample was approximately 14 W m^{-2} at 630 nm.

For kinetic studies, data acquisition was carried out in a continuous circuit, flow-through reactor system. The chlorophyllin sample solution was drawn into the pump and through a 1 cm quartz flow-through cuvette situated in a Hewlett Packard model 8452A UV-Vis photodiode array spectrophotometer. Flow rates were set at 5 mL/min. Readings were taken at 20 sec intervals for periods of up to two hr resulting in several hundred data points for each kinetic bleaching experiment. The continuous circuit system allowed uninterrupted measurement with small sampling ratios and large mean residence times.

2.2 Infrared Absorption Spectra

Infrared absorption spectra of unbleached and photobleached chlorophyllin were acquired as a pressed KBr disc after solvent removal. Three separate discs of each type were prepared. For unbleached chlorophyllin, the average sample was 0.59 ± 0.04 mg in 112.11 ± 0.01 mg of KBr. For photobleached, the average sample was 1.76 ± 0.04 mg in 139.84 ± 0.01 mg of KBr. The powdered analyte and KBr matrix was mixed in a dental mill for 20 min. The mixture was then pressed into a disc with a KBr press. The disc form was washed with acetone and dried in an oven at 110°C for 1 hr prior to use. Owing to transfer losses, the final disc weights were 91.34 ± 0.01 mg for the unbleached and 100.02 ± 0.02 mg for the photobleached sample. A MIDAC MD2000 FT-IR with a DTGS detector was used. The spectrometer was continuously purged with high purity (99.99%) nitrogen. All spectra were acquired with an instrumental resolution of 1 cm^{-1} at 256 coadditions to achieve adequate signal-to-noise ratio.

2.3 High Performance Liquid Chromatography and Mass Spectral Analysis

Semi-preparative HPLC was used to identify which major components in commercially available chlorophyllin underwent photodestructive photobleaching and to fractionally collect samples for further analysis. Aqueous solutions of the trisodium salt of chlorophyllin were prepared under minimal light conditions in distilled water and then photobleached for 24 hrs. A control solution was prepared and stored in a refrigerator while protected from any light. Both solutions were then acidified from a nominal pH 9.66 to pH 2.3 by adding 0.10 M HCl. This aqueous solution was extracted with 3 - 10 mL aliquots of diethyl ether. The three diethyl ether fractions were combined and brought to dryness under a stream of nitrogen. The residue was dissolved in the mobile phase for HPLC analysis which was performed with a Varian 9000 Series HPLC equipped with a 9012 pumping system and a 9050 variable wavelength detector operated at 407 nm. A Waters µBondapak 10 micron C18

(250 x 4.6 mm I.D.) analytical column with an acetonitrile:water mobile phase was used for these separations. The pump was operated in the gradient mode at a combined flow rate of 1 mL/min. The solvent gradient program consisted of an initial solvent composition of 30:70 acetonitrile: water for two min followed by a linear gradient to 90:10 acetonitrile:water at 18 min where the composition was held constant for an additional 17 min. The total run time was 35 min. The peaks were collected and analyzed on a Bruker Esquire Quadrupole Ion Trap Mass Spectrometer (MS) equipped with an electrospray interface. The samples were infused into the electrospray interface by syringe pump at a rate of 3 μL/min. All spectra were acquired in the negative ion mode. Tandem mass spectra of the molecular anions were acquired by collisional activation with the helium buffer gas.

3 Results

3.1 Time and Temperature Effects on Photobleaching of Chlorophyllin

Absorption spectra of chlorophyllin were collected at 0, 5, 10 and 60 min of illumination. In the spectra both the α and Soret peaks were diminished in a time dependent fashion, the α peak decreasing faster than that of the Soret Peak. The decrease in absorbance in the α peak is indicative of degradation in the highly conjugated structure whereas the Soret reduction is consistent with ring degradation. This could imply a loss of conjugation preceding ring degradation.

We next examined the effect of temperature on the reduction of the α peak at 630 nm. The rate of photobleaching increased as the temperature was raised. Analysis of the rate of bleach taken as the rate of a pseudo-first order treatment of the initial phase of the bleaching (initial 300 sec) showed the activation energy, calculated from an Arrhenius plot, was 4.49 kcal/mol (data not shown). The temperature dependence of bleaching is indicative of a multi-step mechanism, which includes not only a photochemical component but a kinetic (presumably oxidative) component as well. Reduced oxygen concentrations at higher temperatures were apparently not rate limiting because photodegradation rates increased with increasing temperatures resulting in a linear Arrhenius plot in the range between 10°C and 70°C.

3.2 Infrared Absorption Analysis

Infrared spectra of non-bleached and photobleached chlorophyllin is shown in Fig. 1. The fingerprint region is enlarged to highlight structural changes that occur between 1000...800 cm^{-1}. Differences between the bleached and non-bleached molecule can be seen. Most notable is the intensified CO_2^- stretch associated with a deprontonated carboxylic acid at approximately 1400 cm^{-1}, and the disappearance of peaks at 960 and 877 cm^{-1} for the photobleached chlorophyllin. These peaks are attributed to vinyl CH and vinyl CH_2 deformations. The vinyl CH and CH_2 deformations appear slightly lower in frequency due to electron "donation" from the porphyrin ring system [12]. The vibration characteristic of a nonconjugated C=C at 1673 cm^{-1} (not shown) also disappears in the spectrum of the photobleached sample. There does not appear to be any change in the vibrations characteristic of the porphyrin ring [13-14]. These data are indicative of an oxidation occurring on the vinyl group external to the porphyrin ring during the photobleaching process.
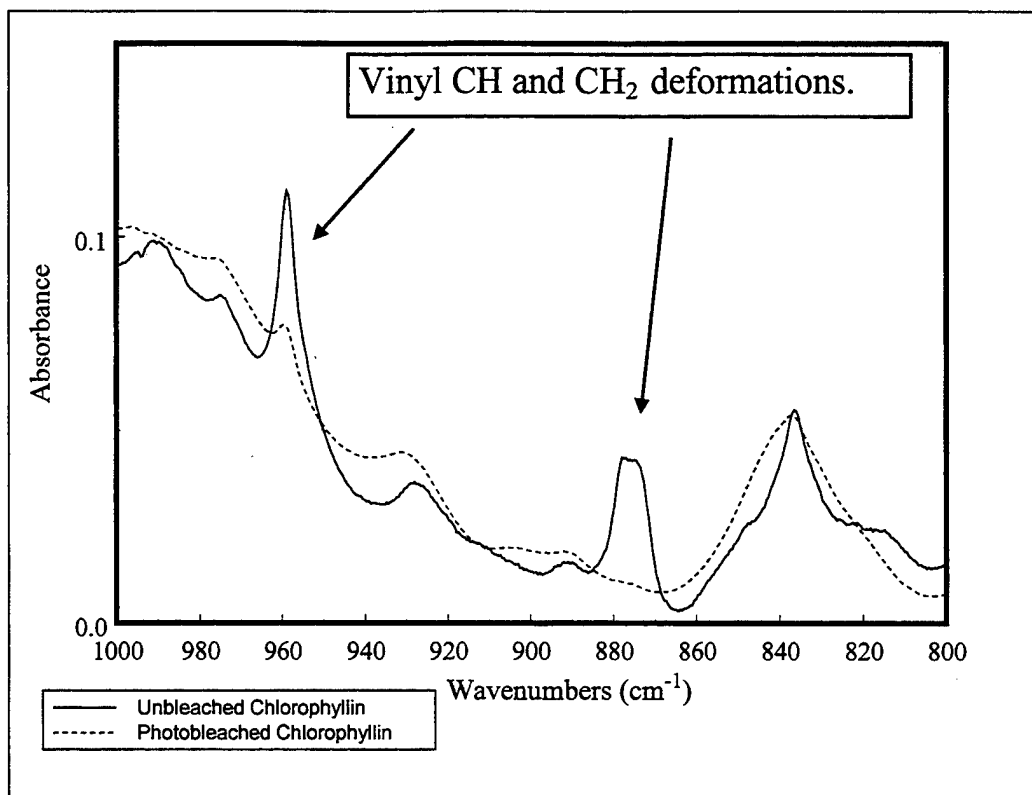
Figure 1. Infrared absorption spectra of unbleached and photobleached (48 hrs) chlorophyllin. Expansion of region between 1000 and 800 cm^{-1}

3.3 Preliminary Analysis of Photobleached Products

Following the separation protocols described previously by Inoue et al. [11] (Figure 2 and 3), chlorophyllin was converted to the free acid by adding 6M HCl until the pH was less than 2.0. The chlorophyllin was then extracted with diethyl ether to eliminate salts and surfactants used in the isolation and commercial conversion of chlorophyllin [9]. Four major peaks were observed from the unbleached sample (RT 19 min., RT 20 min. RT 22 min. and RT 26 min.) with the peak at RT 22 min. being split into at least two components. These four peaks were collected and analyzed by electrospray MS. No conclusive information was obtained from peak#1 at retention time (RT) 19 min. Either the concentration of material that produced this peak was extremely low or the material did not fully deprotonate under the spray conditions employed. However, peak#2 (RT 20 min) contained at least three different chlorophyllin like compounds with neutral masses of 629, 657, and 721. Tandem mass spectrometry of these three components revealed a common loss of 44 Da indicative of decarboxylation. The component with mass 657 was consistent with Cu (II) chlorin e6. The compounds with masses 629 and 721 were not identified. Peak#3 (RT 22 min) also contained three components with masses 613, 627, and 705. Again, tandem mass spectrometry indicated a common loss of 44 Da from the three components, respectively. The component with neutral mass 613 was tentatively assigned to be Cu (II) chlorin e4. The last major peak (peak#4, RT 26 min) contained only two components with neutral masses 611 and 625. Tandem mass

spectrometry under the same conditions as above produced different results. The component with mass 611 ([M-H]⁻ = m/z 610) produced m/z 522 by two successive losses of 44 Da. However, the component at mass 625 ([M-H]⁻ = m/z 624) produced m/z 551 via loss of 73 Da consistent with $^XCH_2CH_2COOH$.

Figure 2. Chromatographic Separation of Unbleached Chlorophyllin

The photobleached sample contained only two peaks at RTs 20 and 22 min. Peak#1 (RT 20 min) contained three components with masses 630, 632, and 721. The mass 721 component remained unchanged after photolysis. The component assigned as Cu (II) chlorin e6 was lost. Peak#2 (RT 22 min) contained two components with masses 613 and 627 relatively unchanged by the photolysis. While the peaks at RT 20 and 22 appear in both the dark and photobleached samples, the composition of the peaks was altered by the photolysis of the Cu (II)

Figure 3. Chromatographic Separation of Bleached Chlorophyllin

chlorin e6. In conclusion, this mass spectral data indicate that Cu (II) chlorin e6 was converted or destroyed by photobleaching.

4   Discussion

The initial premise in undertaking this study was to utilize a simple, relatively stable system in which to analyze the photooxidation of chlorophyll-like molecules, believing that this could serve as a model for photosynthetic systems exposed to continual high light intensities. To the contrary, our studies, as well as that of Inoue et al. [11], have shown that commercially available chlorophyllin, widely used in industrial products, consists of several components. Moreover, our analysis shows the sample to be comprised of more than the four components previously described by Inoue et al. [11]. In addition, the presence of emulsifiers could lead to large molecular weight micellar complexes, which would explain why chlorophyllin solutions are not easily dialyzed. Nevertheless, despite the complexity of the system, we feel that our data reveal certain aspects about chlorophyllin behavior upon
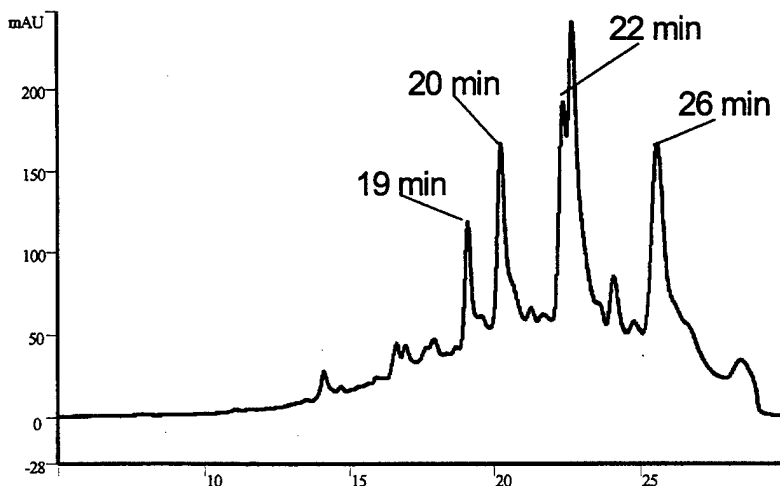
irradiation and allow for the elaboration of possible reaction mechanisms to explain, in part, the photooxidative process.

Our analysis of the products separated by HPLC revealed that two peaks are lost upon photobleaching, one of which has been identified as Cu (II) chlorin e6. The other peaks changed in relative intensities but preliminary double mass spectral analysis of the remaining peaks were inconclusive.

Our infrared spectra data may indicate that in the course of photodestruction, the vinyl group on the chlorophyllin molecule may be undergoing an oxygenation resulting in the formation of an oxirane. We have shown that under aerobic conditions, the pigment molecule chlorophyllin is bleached in a temperature dependent fashion, thereby implicating a thermal component in the process. Therefore, it is conceivable that an oxygenation might be involved in the photobleaching process. The oxygenation may be in the form of two mono-oxygenations in which an oxirane (epoxide) is first formed followed by a second oxygenation leading to the formation of a carboxylate. Alternately, a single dimolecular oxygenation resulting in an endoperoxide might be possible.

Possible oxygenation agents include: $^{X}O_2^-$, $^{1}O_2$, ^{X}OH as well as H_2O_2. We have previously shown that neither superoxide dismutase nor hydroxyl radical nor singlet oxygen traps were effective in preventing the photobleaching of chlorophyllin [6]. Only catalase afforded some degree of protection. Hence, it would appear that the oxygenating species exists in the bound or caged state, protected from external reagents. In this sequence, the bound O_2 is reduced to form a caged $^{X}O_2^-$. Reductant could be provided either directly from the ring or through a Cu II/Cu I transition. The sequestered superoxide could, in turn, oxygenate the vinyl group as well as interact with porphyrin rings, eventually leading to deconjugation, ring opening and the destruction of the molecule.

It should be noted that the potential photooxygenations postulated in this work contrast with the *in vivo* enzymatic monooxygenations recently described by Hortensteiner et al. [15] for pheophorbide *a*. Their elegantly described enzymatic system is a chlorophyll elimination that serves as part of the metabolic turnover of the molecule in the dark during growth of the photosynthetic organism. In contrast, we are describing potential photodestructive reactions that may be occurring in an illuminated, photoreactive system.

The Cu-containing chlorophyllin molecule is inherently more stable than chlorophyll and also lacks ring V. However, despite these differences, the molecule's stability can lend itself to a more detailed study of the oxygenation products. Our data show that oxygenation is involved in photodestruction. These studies may have utility in serving as a model for chlorophyll degradation during times of photosynthetic stress in plants, algae and photosynthetic bacteria. Also these studies may have some utility in assessing ways of stabilizing chlorophyll for possible industrial applications. However, to further elucidate the mechanism involved in the photobleaching of chlorophyllin, a detailed analysis of the photodestructive process of each individual major chlorophyllin component would be required.

5 Acknowledgments

6 References

1. H.D. Rabinowitch and I. Fridovich (1983) Superoxide radicals, superoxide dismutases and oxygen toxicity in plants. *Photochemistry and Photobiology*, **37**, 679-690.
2. M.L. Salin (1987) Toxic oxygen species and protective systems of the chloroplast. *Physiologia Plantarum*, **72**, 681-689.
3. R.D. Allen (1995) Dissection of oxidative stress using transgenic plants. *Plant Physiology*, **107**, 1049-1054.
4. J.D. Spikes (1977) Photosensitization, In, *The Science of Photobiology*, (Edited by K.C. Smith), pp 87-112. Plenum Press, New York.
5. A. Telfer, S.M. Bishop, D. Phillips and J. Barber (1994) Isolated photosynthetic reaction center of photosystem II as a sensitizer for the formation of singlet oxygen. Detection and quantum yield determination using a chemical trapping technique. *Journal of Biological Chemistry*, **269**, 13244-13253.
6. A. Penttilä, C.R. Boyle and M.L. Salin (1996) Active oxygen intermediates and chlorophyllin bleaching. *Biochemical and Biophysical Research Communication*, **226**, 135-139.
7. J.J. Jen and G. Mackinney (1970) On the photodecomposition of chlorophyll in *vitro-I.* reaction rates. *Photochemistry and Photobiology*, **11**, 297-302.
8. K.L. Marsh and J.S. Connolly (1984) Effects of solvent on the rate of bacteriochlorophyll *a* photo-oxidation. *Journal of Photochemistry*, **25**, 183-195.
9. A. Llewellyn, R.F.C. Mantoura and R.G. Brereton (1990) Products of chlorophyll photodegredation. 2. Structural identification. Photochemistry and Photobiology **52**, 1043-1047.
10. Warner Jenkinson Europe Website; http://www.colorcreators.com/18 chlor.htm.
11. H. Inoue, H. Yamashita, K. Furuya, Y. Nonomura, N. Yoshioka and S. Li (1994), Determination of copper (II) chlorophyllin by reversed-phase high-performance liquid chromatography. *Journal of Chromatography A*, **679**, 99-104.
12. G. Socrates (1994) *Infrared Characteristic Group Frequencies: 2nd Ed.*; John Wiley & Sons, Inc.: New York.
13. H. Ogoshi, Y. Saito and K. Nakamoto (1972) Infrared spectra and normal coordinate analysis of metalloporphins. *Journal of Chemical Physics*, **57**(10), 4194-4202.
14. H. Susi and J. S. Ard (1977) A valence force field for nickel porphin and copper porphin. *Spectrochimica Acta,* **3A**, 561-567.
15. S. Hörtensteiner, K.L. Wüthrich, P. Matile, K-H. Ongania and B. Kräutler (1998) The key step in chlorophyll breakdown in higher plants: Cleavage of pheophorbide *a* macrocycle by a monooxygenase. *Journal of Biological Chemistry*, **273**, 15335-15339.

Future Direction

We are currently working on developing a NIR and MIR diffuse reflectance spectroscopic method to remotely detect leaf nitrogen status of cotton (*Gossypium hirsutum L.*) plants. Mississippi State University is growing the plants and conducting the chromatographic analysis of leaf pigments.

Selected Publications and Conference Presentations

1. Alvarez, Luis M.; Fountain, Augustus W. III; Lynn, Bert; Salin, Marvin L. "Photooxidative Bleaching of Chlorophyllin", Free Rad. Res., 31(Supplement), 1999, 97-105.
2. Salin, Marvin L.; Fountain, Augustus W. III; Lynn, Bert "Photoperoxidation of Chlorophyllin: Evidence of a Carboxylated Product", Winter Meeting 1998 of the Society for Free Radical Research, Granada, Spain, November 1998.
3. Alvarez, Luis M.; Shea, Corey; Fountain, Augustus W. III, Salin, Marvin "Mechanism of Oxidative Bleaching of Chlorophyllin", ACS Spring National Meeting, San Francisco, California, 1997.

Cadet Publications and Presentations

1. Alvarez, Luis M.; Shea, Corey; Fountain, Augustus W. III, Salin, Marvin "Mechanism of Oxidative Bleaching of Chlorophyllin", ACS Spring National Meeting, San Francisco, California, 1997.

Cadet Involvement

1. CDT Luis Alvarez, c/o 1997, CH489-490.
2. CDT Corey Shea, c/o 1997, CH489-490
3. CDT Tresa van Heusen, c/o 2000, CH489-490.

Collaboration

1. Marvin L. Salin, Ph.D., Professor of Biochemistry, Mississippi State University
2. Bert C. Lynn, Ph.D., Associate Professor of Chemistry, Mississippi State University
3. Jac J. Varco, Ph.D., Professor of Agriculture, Mississippi State University
4. Bahanu Habulihaz, Ph.D. (candidate), Mississippi State University
5. Madhankumar Sathyamoorthy, Ph.D. (candidate), Mississippi State University

Timothy Michael Pritchett

Department of Physics
United States Military Academy
West Point, New York 10996

(914) 938-2315
ht1187@usma.edu

EDUCATION

PhD Physics, University of California Berkeley, 1990.
Thesis: "Supersymmetry, Index Theorems, and Differential Forms"
Centre de Physique Théorique (theoretical laboratory for the CNRS) *and* Université d'Aix–Marseille (France) 1985–86.
MA Physics, University of California Berkeley, 1984.
Diplomvorprüfung (comprehensive exams) Mathematics, Georg–August–Universität Göttingen (Germany), 1982. Grade "1" = "very good."
BA "with distinction," Integrated Science Program, Northwestern University, 1980.

PROFESSIONAL APPOINTMENTS

Associate Professor of Physics, United States Military Academy, West Point, New York, 1998–Present
Assistant Professor of Physics, United States Military Academy, West Point, New York, 1994–1998
Visiting Assistant Professor of Physics, Pomona College, Claremont, California, 1992–1994
Lecturer in Summer Session, University of California, Berkeley, California, Summer 1991, 1992, 1993
Visiting Assistant Professor of Physics, The College of Wooster, Wooster, Ohio, 1991–92
Lecturer, Step 8, California Polytechnic State University, San Luis Obispo, California, 1990–91

PERSONAL

Born 20 March 1958, in Prairie du Chien, Wisconsin.
Single, no children.

CURRENT RESEARCH INTERESTS

Theoretical modeling of a variety of systems and processes in nonlinear optics: stimulated rotational Raman scattering (in support the experimental work of M. Donovan and L. Henry, USMA); beam propagation in thick nonlinear materials (in support of experimental work under G. Wood, U. S. Army Research Lab); development of more accurate models of optical parametric oscillators.

STIMULATED ROTATIONAL RAMAN SCATTERING IN H₂ GAS IN THE PRESENCE OF STOKES SEEDING

TIMOTHY M. PRITCHETT

Department of Physics and Photonics Research Center
United States Military Academy, West Point, New York 10996
E-mail: ht1187@usma.edu

Considerable progress has been made in our efforts to develop a seeded experiment to measure the Stokes gain resulting from stimulated rotational Raman scattering (SRRS) of an elliptically polarized pump beam by gaseous H₂ as a function of the polarization ellipticity of the pump beam. A single-mode Nd:YAG laser, intended to serve as the pump in the new experiment, has been designed and built, and its output is currently being characterized. At the same time, a design for the remainder of the experimental setup has been developed. External seeding of the Raman medium with radiation at the Stokes frequency should eliminate the shortcomings inherent in our recently published investigation of SRRS in H₂ using an unseeded experiment.

1 Introduction

Stimulated rotational Raman scattering (SRRS) was first observed in gaseous deuterium by Minck, Hagenlocker, and Rado [1] in 1966. The process subsequently became the subject of a number of experimental investigations [2, 3, 4], and it has attracted renewed interest [5, 6] in the past few years. One expects the gain in SRRS, unlike that in the corresponding vibrational Raman process, to be strongly influenced by the ellipticity of the polarization of the pump radiation. Experimental studies of the dependence the SRRS gain on the polarization state of the pump do indeed support this expectation, but only in a limited way, since these investigations involved only linearly or circularly polarized pump beams. More complete experimental confirmation arrived in mid-1999, when a group from this Center (Colonel Bruce G. Oldaker, Lieutenant Colonel (retired) Thomas R. Moore, and First Lieutenants (and former USMA Cadets) James Smith and Gregory McIntyre, and this author) published their results on the dependence of the intensity of the scattered Stokes radiation in SRRS on the polarization of a pump beam of arbitrary ellipticity [7].

We begin this report with a brief review of the salient results of the classical theory of SRRS presented in [7], since certain of these results apply both when the SRRS process is externally "seeded" with radiation at the Raman-shifted frequencies and when it is "unseeded." In an unseeded SRRS experiment, the initial polarization of the fields at the shifted frequencies (in particular, the Stokes field) is random, so [7] makes an *ad hoc*, though very reasonable assumption, about the effective initial polarization in the unseeded case. The experimental data in [7] appear to validate this assumption, despite their large uncertainties. These uncertainties, which reflect the stochastic nature of the initiation process, are intrinsic to an unseeded experiment; to reduce their size, one must "seed" the scattering medium with radiation at the Stokes frequency. Such a seeded experiment has long been the goal of the SRRS group of the Photonics Research Center. At the Center's last technical review two years ago, Oldaker [8] reported on his efforts with Second Lieutenants (former Cadets) Peter Chapman and Bruce Rohrbough to design a single-mode Nd:YAG laser of sufficient power

for such an investigation. In the interim, Lieutenant Colonel Michael Donovan, Captain Leanne Henry, Cadet Dixon Brockbank, and Cadet Brandon Woll have constructed a laser following the Oldaker-Chapman-Rohrbough design and are currently in the final stages of characterizing the beam; Donovan reports on that work elsewhere in this *Program Review.* At the same time, this author, in consultation with Colonel Oldaker, has developed a design for the other apparatus to be used in the proposed seeded SRRS experiment. The setup of the seeded experiment is discussed in the final section of this report.

2 A Two-beam Classical Theory of SRRS

2.1 General theory: Stokes + (depleted) pump

Pritchett, *et al.* [7] present a purely classical theory of SRRS which is applicable even in the regime in which the pump beam experiences significant depletion as it propagates through the Raman medium. We quote the results for the simplest possible model, one in which the radiation field contains only components at the pump and Stokes frequencies, ω_L and ω_S, respectively. Readers interested in the details of the derivation are referred to [7].

Choosing the z-axis to lie parallel to the direction of propagation of the pump beam, we define the spatially slowly varying amplitude components $\vec{A}_L(z)$ and $\vec{A}_S(z)$ and write the electric field in terms of them as

$$\vec{E}(z,t) = \vec{A}_L(z)\,e^{i(k_L z + \omega_L t)} + \vec{A}_S(z)\,e^{i(k_S z + \omega_S t)} + c.c.,$$

where k_L and k_S are, respectively, the pump and Stokes wavenumbers. We normalize the field amplitudes by dividing by the initial amplitude of the pump: $\vec{a}_S(Z) = \vec{A}_S(Z)/\left|\vec{A}_L(0)\right|$ and $\vec{a}_L(Z) = \vec{A}_L(Z)/\left|\vec{A}_L(0)\right|$, and introduce a dimensionless parameter Z related to the gain.

$$Z = \frac{\varepsilon^{(1)}}{2\pi k_S \gamma \left|\vec{A}_L(0)\right|^2}\, z$$

In the above expression for Z, $\varepsilon^{(1)}$ is the square of the linear refractive index of the medium and γ is positive real quantity whose magnitude is proportional to components of the third-order electric susceptibility: $-i\gamma = 2\chi_{1122}(\omega_S;\omega_L,-\omega_L,\omega_S) = -2\chi_{1122}(\omega_L;\omega_S,-\omega_S,\omega_L)$. (There is only a single independent component of the susceptibility governing purely rotational SRRS transitions in gaseous hydrogen. For a further discussion of this, we refer the interested reader to [7] and the references cited therein.) In terms of these quantities, the pump and Stokes frequency components of the nonlinear wave equation in the slowly varying envelope approximation may be written:

$$\frac{d\vec{a}_S(Z)}{dZ} = 3\vec{a}_S(\vec{a}_L \cdot \vec{a}_L{}^*) - 2\vec{a}_L(\vec{a}_S \cdot \vec{a}_L{}^*) + 3\vec{a}_L{}^*(\vec{a}_S \cdot \vec{a}_L) \tag{1a}$$

$$\frac{d\bar{a}_L(Z)}{dZ} = \frac{k_L}{k_S} \left[3\bar{a}_L(\bar{a}_S \cdot \bar{a}_S{}^*) - 2\bar{a}_S(\bar{a}_L \cdot \bar{a}_S{}^*) + 3\bar{a}_S{}^*(\bar{a}_L \cdot \bar{a}_S) \right], \tag{1b}$$

As noted above, one might expect the rotational scattering process to depend on the ellipticity of the pumping radiation. To experimentally determine the nature of this dependence, we create elliptically polarized pump radiation by passing the pump beam through a linear polarizer followed by a quarter-wave plate, the fast axis of which is oriented at an angle ε with respect to the transmission axis of the polarizer. The envelope for the normalized pump field is thus of the form

$$\bar{a}_L(Z) = a_L(Z) \begin{bmatrix} \cos\varepsilon \\ i\sin\varepsilon \end{bmatrix}.$$

At this point, it would be straightforward to solve the coupled ordinary differential equations (1) numerically, if only $\bar{a}_S(0)$, the initial value of the Stokes amplitude, were known. In an experiment in which the medium is externally "seeded" with radiation at the Stokes frequency, $\bar{a}_S(0)$ can be controlled precisely, and it is just such an experiment which is described below and which we hope to begin running later this year. In the absence of such an external Stokes seed, however, the SRRS process is stochastically initiated by scattered radiation within the medium. In this case, it is known from very general thermodynamic considerations [9] that $|\bar{a}_S(0)|$ is on the order of 10^{-6}; however, the polarization of the initial Stokes radiation is random.

In order to deal with the random character of the initial polarization of the Raman-shifted fields in an unseeded SRRS process, the theoretical treatment in [7] makes certain assumptions. These assumptions become eminently plausible when we consider the limit in which the pump intensity experiences no significant reduction as the pump beam propagates through the scattering medium.

2.2   Undepleted pump approximation

In the regime in which $|\bar{a}_S(Z)| \ll 1$, the depletion of the pump beam may be neglected, and the normalized pump field amplitude treated as a constant [10]: $\bar{a}_L(Z) = \bar{a}_L(0)$. Equation (1a) then reduces to the linear equation

$$\frac{d}{dZ}\bar{a}_S(Z) = \begin{bmatrix} \frac{7}{2} + \frac{1}{2}\cos(2\varepsilon) & \frac{5}{2}i\sin(2\varepsilon) \\ -\frac{5}{2}i\sin(2\varepsilon) & \frac{7}{2} + \frac{1}{2}\cos(2\varepsilon) \end{bmatrix} \cdot \bar{a}_S(Z)$$

with the general solution

$$\bar{a}_S(Z) = \frac{\bar{v}_+{}^* \cdot \bar{a}_S(0)}{|\bar{v}_+|^2} \bar{v}_+ \exp(\lambda_+ Z) + \frac{\bar{v}_-{}^* \cdot \bar{a}_S(0)}{|\bar{v}_-|^2} \bar{v}_- \exp(\lambda_- Z),$$

where $\bar{a}_S(0)$ is the initial value of the normalized Stokes field amplitude. The gain eigenvalues $\lambda_\pm$ are given by

$$\lambda_{\pm} = \tfrac{1}{2}\left(7 \pm \sqrt{1 + 24\sin^2 \varepsilon}\right),$$

and the corresponding eigenvectors are, respectively,

$$\vec{v}_+ = \frac{1}{2}\begin{bmatrix} \cos(2\varepsilon) + \sqrt{1 + 24\sin^2 \varepsilon} \\ -5i\sin(2\varepsilon) \end{bmatrix} \quad \text{and} \quad \vec{v}_- = \frac{1}{5}\begin{bmatrix} i\left(\cot(2\varepsilon) - \sqrt{25 + \cot^2(2\varepsilon)}\right) \\ 5 \end{bmatrix}.$$

2.3 Assumed initial Stokes polarization in an unseeded experiment

Generically, $\vec{a}_S(0)$ will include a component parallel to $\vec{v}_+$. This component will experience larger gain than the component parallel to $\vec{v}_-$ and thus will dominate the process, even outside the regime of validity of the undepleted pump approximation. In the case in which $|\vec{a}_S(Z)|$ is not necessarily always negligible compared to unity and the pump beam may experience significant depletion, equations (1) must be solved numerically for given pump ellipticity. In view of the considerations just outlined, we take the initial values of the Stokes and pump fields to be, respectively,

$$\vec{a}_S(0) = \frac{10^{-6}}{|\vec{v}_+|}\vec{v}_+ \quad \text{and} \quad \vec{a}_L(0) = \begin{bmatrix} \cos\varepsilon \\ i\sin\varepsilon \end{bmatrix}.$$

3 Results of Unseeded Experiments

Reference [7] reports experimental data showing the polarization dependence of the intensity of the Stokes radiation produced by unseeded SRRS of a 532-nm, single-mode beam of energy 17.1 ± 0.2 mJ and pulsewidth 30 ± 2 ns. Those data are reproduced above in Figure 1, which shows the energy of the Stokes beam as a function of the wave-plate rotation angle. Each datum represents the average of over 50 individual experimental realizations. The large uncertainties associated with the data reflect the fact that in an unseeded experiment, the
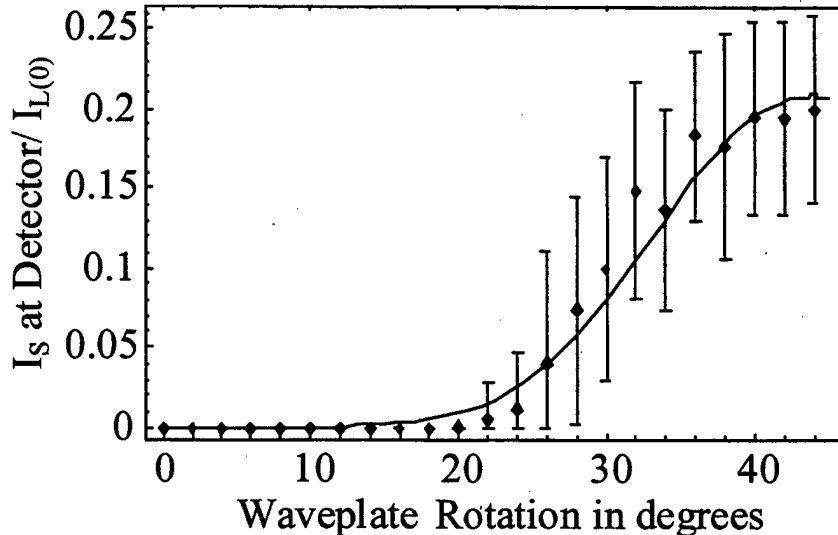

Figure 1. Energy in a single polarization component of the Stokes beam as a function of the waveplate rotation angle. The solid line shows prediction of the simple, classical, two-beam model described in this work.

Stokes beam is initiated by a stochastic process. As a result, the size of the uncertainties cannot be reduced by increasing the number of experimental realizations per data point; rather, these uncertainties can be significantly reduced only by seeding the cell with a Stokes beam of known intensity and polarization.

The solid line in Figure 1 represents the prediction of the model described in [7] with a gain parameter $Z = 2.26$. In accordance with the experimental arrangement, this curve reflects only the energy in the polarization component of the Stokes light parallel to the transmission axis of a final linear polarizer. On average, the energy contained in the anti-Stokes component was less than one percent of the energy in the Stokes component, which justifies the validity of ignoring the anti-Stokes component in the theory. Although the experiment involved a focused beam, the theoretical approximation of a collimated beam appears to be quite adequate in this case.

4 Seeded Experiment

We have devoted the past two years to the design and construction of a single-mode laser for use in an experiment similar to that described in [7], but employing a Stokes seed. Figure 2 shows a schematic of the other apparatus to be used in this investigation. Stokes-shifted radiation generated in the H_2 cell situated between linear polarizers P1 and P2 is used to seed the SRRS process in the other cell. Extraneous frequency components are removed from the seed beam by the 547-nm notch filter, F. As the Stokes seed beam exits the cell in which it is generated, the radiation is circularly polarized in the sense opposite to that of the entering pump. The Stokes seed beam then
passes through a quarter-wave plate, creating a linearly polarized beam. This is done in order
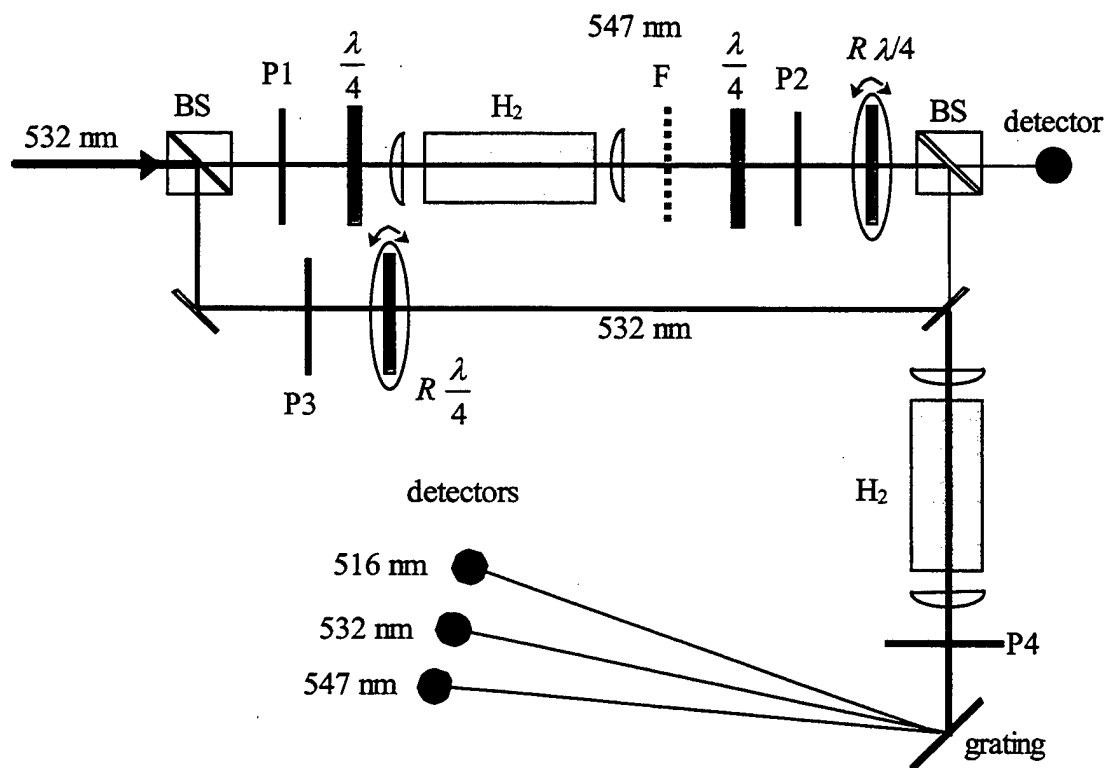

Figure 2. Setup for the seeded experiment.

11-5

to maximize the power transmitted by the linear polarizer P2, whose transmission axis is aligned with that of P1. A pair of quarter-wave plates mounted on rotation stages enable one to independently control the polarization ellipticity of both entering the second Raman cell: the Stokes seed beam and the pump beam. The linear polarizer P4 placed before the grating ensures that the data contain no effects arising from the change in the grating efficiency with the varying polarization. The transmission axis of P4 is oriented parallel to that of P3.

By seeding the Stokes beam, the SRRS initiation can be controlled in both polarization and intensity. From a theoretical standpoint, the primary advantage of a seeded experiment lies in the fact that the initial polarization of the Stokes beam is known, rendering unnecessary the assumption that the initial Stokes polarization lie parallel to the eigenvector corresponding to the larger gain in the undepleted pump version of the classical theory. Experimentally, seeding the cell provides the sole means for reducing the uncertainty in the data. These experiments, which we hope to commence in several months, will provide data to compare with predictions of the gain dependence on the polarization of the initiating radiation.

References

1. R. M. Minck, E. E. Hagenlocker, and W. G. Rado, "Stimulated pure rotational Raman scattering in deuterium," *Phys. Rev. Lett* **17**(5), 229-231 (1966).
2. John L. Carlsten and Robert G. Wenzel, "Stimulated rotational Raman scattering in CO_2-pumped para-H_2," *IEEE J. Quantum Electronics* **QE-19**(9), 1407-1413 (1983).
3. M. A. Henesian, C. D. Swift, and Jr. R. Murray, "Stimulated rotational Raman scattering in nitrogen in long air paths," *Op. Lett.* **10**(11), 565-667 (1985).
4. M. D. Duncan, R. Mahon, L. L. Tankersley, and J. Reintjes, "Rotational Raman gain suppression in H_2," *Op. Comm.* **64**(5), 467-473 (1987).
5. Frank Hanson and Peter Poirier, "Stimulated rotational Raman conversion in H_2, D_2, and HD," *IEEE J. Quantum Electronics*, **29**(8), 2342-2345 (1993).
6. M. R. Perrone, V. Piccinno, G. De Nunzio, and V. Nassisi, "Dependence of rotational and vibrational Raman scattering on focusing geometry," *IEEE J. Quantum Electronics*, **33**(6), 938-944 (1967).
7. Tim Pritchett, James Smith, Gregory McIntyre, Thomas R. Moore, and Bruce G. Oldaker, "Dependence of the gain in stimulated rotational Raman scattering in H_2 on the pump ellipticity," *J. Mod. Optics 46(6)*, 949-956 (1999).
8. Bruce G. Oldaker, "Lasers and Optics Education," *United States Military Academy Photonics Research Center 1998 Program Review* (West Point, NY, 1998), pp. 69-77.
9. B. Ya. Zel'dovich, N. F. Pilipetsky, and V. V. Shikunov, *Principles of Phase Conjugation* (Springer Verlag, Berlin, 1985), p. 29.
10. G. V. Venkin, Yu. A. Il'inskii, and G. M. Mikheev, "Influence of the polarization of radiation on the energy characteristics and threshold of stimulated Raman scattering due to rotational transitions," *Sov. J. Quantum Electron.* **15**(3), 395-397 (1985).

REFINEMENTS IN THE THEORY OF THERMAL LENSING

TIMOTHY M. PRITCHETT

Department of Physics and Photonics Research Center
United States Military Academy, West Point, New York 10996
E-mail: ht1187@usma.edu

We model the thermal lensing of a tightly focused, continuous wave laser beam by a thin sample of a liquid exhibiting nonsaturable linear absorption. If the transverse extent of the sample is small compared to spot size of the beam, the observed Fraunhofer diffraction pattern consists of a series of concentric rings, of which the outermost is always very prominent. The diameter of this outermost ring varies linearly with the beam power. It also varies linearly with the magnitude of the thermo-optic coefficient *dn/dT* of the sample liquid.

1 Introduction

When a laser beam propagates through a sample, a portion of the energy in the beam is absorbed, giving rise to temperature and density gradients within the sample. For beams having a pulsewidth greater than a few microseconds, the effects of density gradients may be safely ignored, while the temperature profile may be obtained by solving the heat equation with a source term proportional to the local beam intensity. The resulting temperature profile induces a parallel spatial variation in the refractive index, effectively forming a lens within the medium. Gordon, *et al.* [1] obtain the solution for the temperature profile in an infinite laminar medium traversed by a principal-mode Gaussian beam at normal incidence, but this result, which forms the point of departure for all subsequent theory on thermal lensing at time scales of a microsecond and longer [2], ignores the effects of heat loss through the planar end faces of the medium. The heat flow model presented below represents the first attempt to treat explicitly the effects of sample cooling and to extend the theory of thermal lensing to cylindrically symmetric beams of non-Gaussian beamshape. Specifically, we model the effects of thermal lensing of a tightly focused, continuous wave, cylindrically symmetric beam by a thin sample of a material exhibiting nonsaturable linear absorption. The sample is confined in a cuvette to a thin, disk-shaped region near the focal plane of the beam. The transverse extent of the sample is significantly greater than the beam spot size. We calculate the diffraction pattern expected at a detector situated some distance away. From the far-field diffraction pattern, one can learn something of the thermo-optical properties of the sample, assuming the beam is well characterized. Alternately, one can employ a sample of known thermo-optical properties and use the diffraction pattern to provide information about the beam itself.

2 A Model for Thermal Lensing of Microsecond Pulses

2.1 Heat Diffusion in a Thin Sample

On time scales longer than a few microseconds, the position-dependent variation in the refractive index that is responsible for thermal lensing arises primarily from the temperature

profile $\Delta T(\vec{r},t)$, *i.e.*, from the spatially non-uniform temperature rise of the medium over the initial temperature of the medium (and ambient air). The temperature profile is obtained by solving the heat diffusion equation with source and sink terms.

$$\left[\rho c \frac{\partial}{\partial t} - \kappa \nabla^2 \right] \Delta T(\vec{r},t) = q(\vec{r},t) - h(\vec{r},t)$$

Here, the constants ρ, c, and κ are, respectively, the density, specific heat, and thermal conductivity of the medium. The combination ρc is the medium's the specific heat per unit volume while $\kappa/\rho c$ is its thermal diffusivity. The function $q(\vec{r},t)$ is the heat source density, carrying units of power/volume. In the present case, where heat is deposited in the material as a result of the absorption of energy from a laser beam propagating through it, $q(\vec{r},t)$ is proportional to the local irradiance $I(\vec{r},t)$, where the constant of proportionality is α, the absorption coefficient of the medium. The function $h(\vec{r},t)$, a heat sink density, describes heat loss through the boundaries of the medium: for a sample of thickness Δz, the rate of energy loss through an infinitesimal element of surface area dA,

$$h(\vec{r},t)\,\Delta z\,dA = H\,\Delta T(\vec{r},t)\,dA,$$

is proportional to the difference in temperature between that infinitesimal element of sample surface and the surrounding air. As a practical matter, the constant of proportionality H must be measured experimentally.

In the absence of nonlinear absorption, the beamshape exhibits no change as the beam propagates through the sample. If the sample is thin, the effects of longitudinal heat flow within the sample may be safely neglected. In fact, as long as $\Delta z \ll z_R$, we may even disregard the variation of the spot radius with z within the sample and treat w as a constant. Thus, for a thin sample, the temperature profile $\Delta T(r, t)$ is the solution of

$$\rho c \frac{\partial}{\partial t} \Delta T(r,t) - \frac{\kappa}{r} \frac{\partial}{\partial r}\left(r \frac{\partial}{\partial r} \Delta T(r,t) \right) = \alpha I(r,t) - \frac{H}{\Delta z} \Delta T(r,t), \qquad (1)$$

$$\Delta T(r,0) = 0,$$

where either ΔT or its spatial derivative $\partial \Delta T/\partial r$ must satisfy appropriate boundary conditions on the cylindrical sides of the sample. The time scale of the diffusive heat transfer described by (1) is given by the thermal characteristic time $t_c = c\rho w^2/\kappa$. Introducing the dimensionless variables $\tau = t/t_c$ and $\xi = r/w$, we write (1) in the form

$$\frac{\partial \Delta T}{\partial \tau} - \frac{1}{\xi} \frac{\partial}{\partial \xi}\left(\xi \frac{\partial \Delta T}{\partial \xi} \right) = T_c \frac{I(\xi,z)}{I(0,z)} - \frac{Hw^2}{\kappa \Delta z} \Delta T. \qquad (2)$$

Here the characteristic temperature $T_c = 2\alpha P/\kappa$, where the factor of 2 has been inserted for later convenience, sets the scale of the temperature increase resulting from heating of the medium by the beam.

2.2. Temperature Profile for an Infinite Planar Medium with no Cooling

In the event that the sample is not only thin, but has a transverse extent far exceeding the

spot radius, the sample geometry is well approximated by an infinite plane. In this case, there are no radial boundary conditions on the temperature profile ΔT. For the moment, we will ignore the effects heat loss through the end faces of the sample and set $H = 0$; we treat the case of non-vanishing heat loss in the following section. With these approximations, we now solve the partial differential equation (2), subject to the initial condition $\Delta T(r, 0) = 0$, for two different beamshapes.

Gaussian Beam. We consider first the case in which the incident beam is a principal-mode Gaussian beam of spot radius $w(z)$, where z is the longitudinal distance from focus. The beam delivers total power P and is characterized by two parameters, the spot radius at focus w_0 and the Rayleigh range $z_R = \pi w_0^2 / \lambda$, where λ is the wavelength.

For the infinite planar geometry, the partial differential equation (2) with $H = 0$ may be solved analytically for a Gaussian beamshape. The resulting temperature profile, a derivation of which may be found in [1], is

$$\Delta T(\xi, \tau) = \frac{T_c}{8\pi}\left(Ei\left[-2\xi^2\right] - Ei\left[\frac{-2\xi^2}{1+8\tau}\right] \right), \tag{3}$$

where $Ei(z)$ is the exponential integral.

We emphasize the fact that the solution (3) is the product of an overall scale factor proportional to the beam power and a dimensionless function parameterized by the dimensionless ratio τ. The series of thick curves shown in light gray in Figure 1 illustrates how the temperature profile produced by a Gaussian beam evolves with the time parameter τ.

"Top hat" Beam. We turn next to the case of an incident "top hat" beam, whose total output power P is uniformly distributed over a spot of radius w. Following Carslow and Jaeger [3], we obtain the Green's function for the problem:

$$G(\xi, \xi', \tau) = \frac{1}{4\pi \, t_c \kappa \tau} EXP\left[-\frac{\xi^2 + \xi'^2}{4\tau}\right] I_0\left(\frac{\xi \xi'}{2\tau}\right),$$

where I_0 is the modified Bessel function of the first kind. The temperature profile is obtained from the Green's function and the source density $q(\xi', \tau')$ by integration.

$$\Delta T(\xi, \tau) = \frac{T_c}{4\pi} \int_0^1 \xi' \, d\xi' \int_0^\tau \frac{d\tau}{\tau'} EXP\left[-\frac{\xi^2 + \xi'^2}{4\tau}\right] I_0\left(\frac{\xi \xi'}{2\tau}\right) \tag{4}$$

Once again, we discover that the solution is the product of an overall scale factor proportional to the beam power and a dimensionless function parameterized by τ. Numerical evaluation of the integral in (4) for $\tau = 1, 10, 40$, and 100 yields the series of curves designated by the thin, black lines in Figure 1.

The two sets of curves appearing in Figure 1 are virtually identical, illustrating how the energy absorbed from the beam is redistributed ("smeared") by thermal diffusion to produce a generic temperature profile that is relatively insensitive to the beamshape. In fact, the profiles resulting from heating by the Gaussian beam differ noticeably from those obtained for the top hat beam only at distances from the beam axis on the order of the spot size or less, with the higher on-axis temperatures seen from the principal-mode Gaussian beam reflecting

the fact that its on-axis power density is twice that of a top hat beam delivering the same total power. Figure 1 also shows that the relative discrepancy between the two sets of curves diminishes with time, as smoothing by the thermal diffusion process has more opportunity to manifest itself.
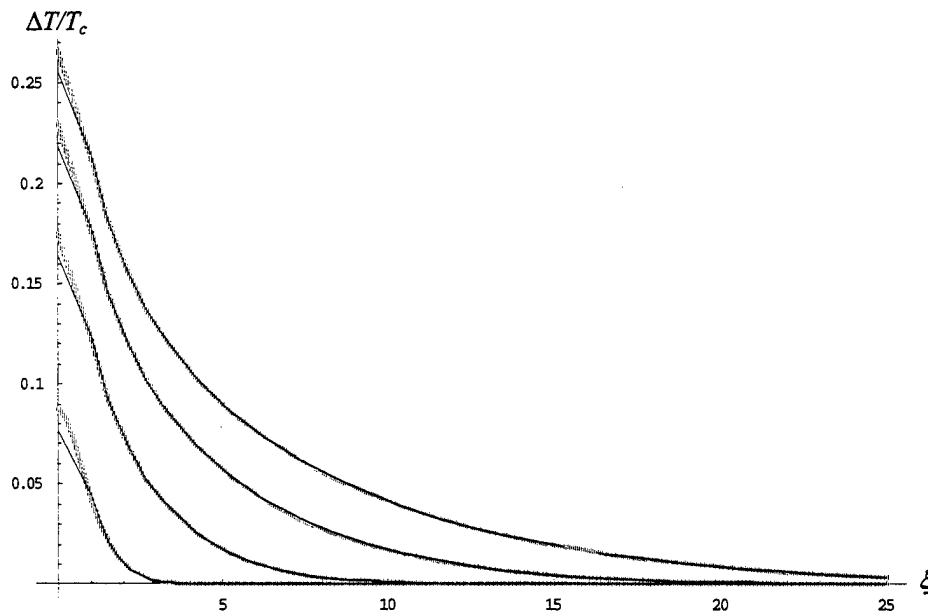

Figure 1. Temperature profile in an infinite planar medium with negligible cooling. In order of increasing height and extent, the four profiles correspond respectively to heating times of 1, 10, 40, and 100 times the thermal characteristic time t_c. The profiles designated by thick, gray lines result from heating by a principal-mode Gaussian beam; those designated by thin, black lines are for a top hat beam.

We summarize the results of this section as follows. In the absence of cooling by the external surroundings, the temporal dependence of the temperature profile in an infinite planar medium undergoing heating by a laser beam propagating through it in the direction normal to the plane is given by a dimensionless parameter. This parameter, τ, is the time the sample has experienced heating by the beam divided by a thermal characteristic time related not only to the thermal properties of the material, but to the beam spot size as well. The overall scale T_c of the temperature profile varies linearly with the beam power and is independent of the beamshape. The *shape* of the temperature profile is given by a dimensionless function of the time parameter τ, and this shape function is insensitive to the beamshape, at least for sufficiently large values of τ.

2.3. Incorporation of Cooling Effects

The solution of (2) in the presence of cooling through the end faces of the sample is complicated by the unavailability of a value for H, the constant of proportionality linking the escaping heat flux to the local temperature difference between the medium and the surrounding air. In principle, H ought to be measured directly for the particular experimental setup used, but this determination is somewhat problematic.

In order to avoid the necessity for a direct measurement of H, we proceed as follows. It is clear on physical grounds that the solution to (2) in the presence of cooling must asymptotically approach a steady-state profile for sufficiently long times. The form of the (time-dependent) solutions obtained in absence of cooling suggests that the steady-state profile resulting when cooling is included should be characterized by an overall scale factor which varies linearly with the beam power P. We assume that the *shape* of the steady-state profile is independent of P, and we approximate the shape of the steady-state profile by that obtained from the analytic solution at a particular value of the dimensionless ratio τ. We determine the critical value of τ by fitting the far-field diffraction pattern predicted by the model for a given value of the beam power to that actually observed experimentally. In the event that the shape of actual steady-state temperature profile exhibits no (or only weak) dependence on the beam power, and that it is indeed well approximated by the profile shape obtained from the analytic solution, then the critical value of τ obtained in this way will be valid for all values of P, within the range of applicability of the model.

2.4. Far-field Diffraction Pattern Due to Thermal Lensing

Given the temperature profile existing in the medium, it is straightforward to compute the resulting far-field diffraction pattern, particularly in the case of a thin sample. As we have already noted, at time scales longer than a few microseconds, it is the temperature profile $\Delta T(\vec{r}, t)$ that dominates the local variation of refractive index. For a sufficiently thin ($\Delta z \ll z_R$) sample, the effects of a position-dependent change in the refractive index are adequately represented by a phase shift at the exit face of the sample. Huygens' integral relates the electric field amplitude on the exit face of the sample to the field at a detector situated a (comparatively long) distance down the optic axis. In the present case, the cylindrical symmetry of the field on the exit face permits the integration over the angular coordinate to be performed analytically, yielding a Bessel function. The remaining integration over the radial coordinate on the exit face thus takes the form of a Fourier-Bessel transform, commonly known as a Hankel transform. We compute it using the algorithm recently published by Magni, *et al.* [4].

Although the temperature profile, and thus the induced thermal lens, is relatively insensitive to the beamshape, the far-field diffraction pattern is not, as Figure 2 illustrates. Of course, this is true even in the absence of thermal lensing effects: for instance, the diffraction pattern, both near- and far-field, of a freely propagating Gaussian beam is itself Gaussian, whereas the Fraunhofer diffraction pattern resulting from a top hat beam is marked by interference fringes (Airy rings).

3 Comparison of Model Predictions and Experimental Data

As described above, the dimensionless ratio τ is assumed to parameterize a function giving the shape of the steady-state temperature profile. In order to determine the critical value of τ corresponding to the profiles actually observed, we calculate the diffraction pattern predicted at a distance of 21 z_R (16.75 cm) from a sample having a thermal characteristic time t_c of 28.9 ms, illuminated by an argon ion laser at 11.2 mW. Fitting the intensity distribution obtained from the model to that recorded experimentally, we obtain a "best fit" value of $\tau = 0.15$. The

value of τ obtained by fitting the far-field intensity pattern observed from the 11.2-mW beam was then used to compute the patterns predicted at a range of other laser powers. These patterns show good agreement with those observed experimentally.
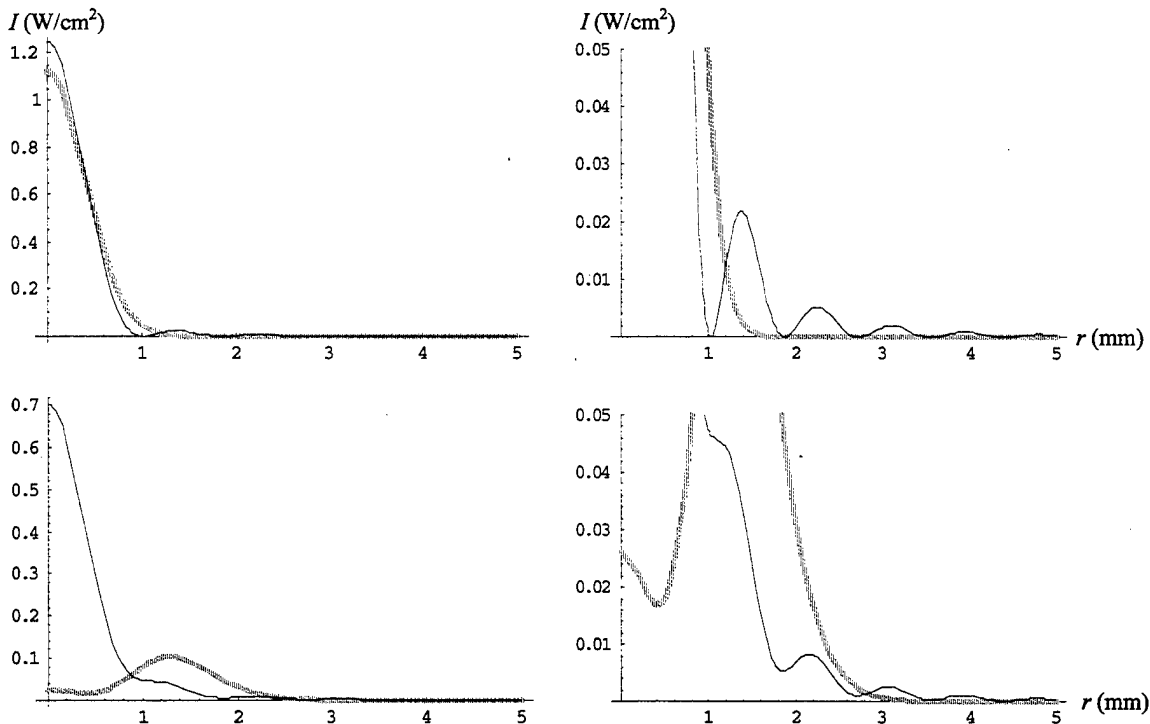

Figure 2. Effect of beamshape on far-field intensity. Thick, gray lines designate intensity profiles at 22 Rayleigh ranges from focus of a principal-mode Gaussian beam; thin, black lines, profiles from a top hat beam. Both beams deliver 11.2 mW. Profiles shown at the top result from free propagation alone (no sample); those appearing below arise from thermal lensing by a thin sample heated for 0.15 t_c. Airy rings resulting from diffraction of the top hat beam are clearly seen in the expanded scale used in the graphs on the right.

4   Results of Modeling Studies

Employing the thermal lensing model of Section 2 with τ fixed at the experimentally determined value of 0.15, we investigated the dependence of the far-field diffraction pattern on various parameters, to include the beam power. We modeled a linearly absorbing material having an absorption coefficient α of 14.95 cm^{-1} and exhibiting no saturation. The assumed values of 9.1×10^{-8} m^2/s for the thermal diffusivity $\kappa/\rho c$ and -5.6×10^{-4} K^{-1} for the thermo-optic coefficient dn/dT correspond to the values for toluene. A principal-mode Gaussian beam of wavelength 514 nm propagates through a sample of the material. The waist w_0 of the focused beam is 36 μm, corresponding to a Rayleigh range of 7.9 mm. The sample has a thickness of 0.1 mm and is situated 8.0 mm behind the focal plane. We used the model to calculate the intensity distribution on an image plane located 175.5 mm from focus.

The far-field diffraction pattern consists of a series of concentric rings, of which the outermost is the most prominent. The rings are present for laser powers in excess of 4 mW; at lower powers, only a single central maximum is distinguishable. For values of the laser power less than 98 mW, the outermost ring is the brightest ring in the pattern, and even

above this level, it remains the pattern's most easily distinguished feature. The radius r of the outermost ring increases linearly with the beam power P according to the relation $r = m\,P + r_0$. We find a value of 0.123 ± 0.003 mm/mW for the slope m and 0.10 ± 0.08 mm for the intercept r_0. In addition, the number of rings present in the diffraction pattern also depends linearly on the power; in general, one additional ring can be observed for each 10-mW increase in the total beam power. Finally, we note that r is not a function of beam intensity, that is, it depends not on the ratio P/w^2, where w is the spot radius, but rather depends on P and w independently.

At a fixed value of the beam power, the radius r of the outermost ring varies linearly with the thermo-optic coefficient dn/dT. As in the previous case, the outermost ring is the most prominent feature of the diffraction pattern, and, for $dn/dT \tau\ 0.0048$ K^{-1}, it is also the brightest ring present in the pattern. The relation between r and dn/dT passes through the origin (intercept zero): $r = m \times dn/dT$. At a beam power of 11.2 mW, we find a value of 2110 ± 40 mm K for the slope m. The number of rings also increases roughly linearly with dn/dT, with one additional ring observed for each increase in dn/dT of about 0.0005 K^{-1}.

5 Conclusions

Presented here is a theoretical model capable of predicting the far-field intensity distribution resulting from thermal lensing of a principal-mode Gaussian laser beam having a pulsewidth in excess of several microseconds. The lensing effect is produced by the absorption of radiant energy from a propagating laser beam by a thin sample of a nonsaturable, linearly absorptive material. The transverse extent of the sample is significantly greater that the spot size of the beam, so edge effects due to the longitudinal "sides" of the sample may be ignored. In order to treat the effects of cooling through the transverse end faces of the sample, the model makes two *ad hoc* assumptions regarding the shape of the steady-state temperature profile arising in the sample when the rate at which the sample absorbs heat from the propagating beam exactly balances that at which it loses heat to the surrounding air. The model assumes that even though the overall *scale* of the steady-state profile depends on the beam power, the *shape* of the profile does not. It further assumes that this steady-state shape is well approximated by the shape of the profile occurring in an uncooled, infinite planar sample of the same material for a particular value of a dimensionless parameter τ. A value is obtained for τ by fitting the far-field intensity distribution computed using the model to experimental data taken at a single beam power. The parameter value obtained in this way is then used in the model to calculate the far-field intensity distributions predicted at a range of other beam powers. These predictions show excellent agreement with the observed intensity distributions, which seems to validate the assumptions of the model.

Thermal lensing gives rise to a characteristic diffraction pattern consisting of a series of concentric rings (intensity maxima), of which the outermost is generally the brightest and is in all cases very prominent. We used the model to investigate the dependence of the radius of the outermost ring on the beam power at fixed values of the beam waist at focus and of the parameters characterizing the medium. We found the radius of the outermost ring, as well as the number of rings, to vary linearly with the beam power. We also used the model to study the dependence of the outermost ring radius on the thermo-optic coefficient dn/dT of the sample at fixed values of the beam power, the beam waist, and the other material parameters. In this case, the radius of the outermost ring, as well as the number of rings, exhibits a linear

dependence on dn/dT of the sample. An application of these results to characterization work is described elsewhere [5].

References

1. J. P. Gordon, R. C. Leite, R. S. Moore, S. Porto, and J. R. Whinnery, "Long-transient effects in lasers with inserted liquid samples," *J. Appl. Phys. 36(1)*, 3-8 (Jan 1965).
2. S. A. Akhmanov, et al., "Thermal Self-Action of Laser Beams," *IEEE J. Quantum Electronics QE-4(10)*, 568-575 (Oct 1968).
3. H. S. Carslaw and J. C. Jaeger, *Operational Methods in Applied Mathematics, 2nd Ed.* (Dover Publications, New York,1948), pp. 343 ff.
4. Vittorio Magni, Giulio Cerullo, and Sandro De Silvestri, "High-accuracy fast Hankel transform for optical beam propagation," *J. Opt. Soc. Am. A 9(11)*, 2031-2033 (1992).
5. Timothy Pritchett, Gary L. Wood, and Andrew G. Mott, "A Novel powermeter based on thermal lensing," ARL Technical Report, ARL-TR-xxxx, in press.

Future Direction

The project described in this report was concluded in December, 1999. My collaborators and I are currently applying for a U.S. patent for a device based in part on these results.

Selected Publications and Conference Presentations

1. T. Pritchett, "Thermal Lensing in a Non-saturable Absorber," *Proceedings of the Sixth Annual ARL/USMA Technical Symposium* (West Point, NY: 1998), pp. 184-195.
2. T. Pritchett, "Aspects of Beam Propagation and Thermal Lensing," *Proceedings of the US/UK Laser Beam Propagation Modeling Workshop*, (Wright-Patterson Air Force Base, OH: 1999), pp. 124-130.
3. T. Pritchett, "Modeling Long-timescale Thermal Effects in Nonlinear Optical Media," *Proceedings of the Seventh Annual ARL/USMA Technical Symposium* (West Point, NY: 1999), pp. 171-181.

Cadet Involvement

2LT Robert Allee, Class of 1999, AIAD project, Summer 1998. 2LT Allee (at that time, CDT Allee) experimentally measured the radius of the outermost ring in the far-field diffraction pattern as a function of the beam power.

Collaboration

Dr. Gary L. Wood and Mr. Andrew G. Mott, Optics Branch, Sensors and Electron Devices Directorate, U.S. Army Research Lab, Adelphi, MD.

Barry L. Shoop

Military Rank: Lieutenant Colonel   **Branch:** Signal Corps /Academy Professor

Home Address: **Office Address:**
294B Lee Road   Photonics Research Center
West Point, NY 10996   United States Military Academy
(914) 446-8341   West Point, New York 10996-5000
                                             (914) 938-5567 (O)
                                             (914) 938-3062 (F)

                                             Email: Barry-Shoop@usma.edu

EDUCATION:

Ph.D.	Stanford University, Stanford, California
	Major: Electrical Engineering, June 1992
	Dissertation Advisor: Joseph W. Goodman
	Dissertation Title: "Optical Oversampled Analog-to-Digital Conversion."
M.S.	U.S. Naval Postgraduate School, Monterey, California
	Major: Electrical Engineering, September 1986
B.S.	The Pennsylvania State University, State College, Pennsylvania
	Major: Electrical Engineering, June 1980

RESEARCH INTERESTS:

Current research interests focus on optical information processing for analog-to-digital (A/D) conversion and includes a major research thrust in the area of smart pixel technology. Applications include high-speed, high-resolution A/D conversion, two-dimensional artificial neural networks for digital halftoning, and wavelet transforms for radar signal processing.

PROFESSIONAL HONORS:

Fellow, Optical Society of America
Senior Member, The Institute of Electrical and Electronic Engineers
IEEE-USA Millenium Medal, February 2000
IEEE-USA Leadership Award, September 1999

MIXED-SIGNAL APPLICATIONS OF SMART PIXEL TECHNOLOGY

LTC BARRY L. SHOOP

Department of Electrical Engineering and Computer Science and Photonics Research Center
United States Military Academy, West Point, New York 10996
E-mail: Barry-Shoop@usma.edu

Smart pixel technology is a relatively new field which integrates electronic circuitry with optoelectronic devices in an effort to improve overall performance of existing applications and enable new applications not previously envisioned with either single technology. Smart pixels leverage the functionality and programmability of established electronic circuit technology and the high-speed switching and parallelism of arrays of optoelectronic devices. A smart pixel hardware implementation of the error diffusion neural network has been investigated and experimentally characterized. This hardware approach to the error diffusion neural network provides the ability to perform real-time image halftoning for applications such as xerography, laser printing, and facsimile.

1 Introduction

Smart pixel technology is a relatively new approach to integrating electronic circuitry and optoelectronic devices in a common framework. The purpose is to leverage the advantages of each individual technology and provide improved performance for specific applications. Here, the electronic circuitry provides complex functionality and programmability while the optoelectronic devices provide high-speed switching and compatibility with existing optical media. Arrays of these smart pixels leverage the parallelism of optics for interconnections as well as computation.

There are a number of different approaches to fabricating smart pixels which generally differ in the way in which the electronic and optical devices are integrated. Monolithic integration, direct epitaxy, and hybrid integration are the three most common approaches in use today. Monolithic integration allows both the electronics and the optical devices to be integrated in a common semiconductor material in a single growth process or by utilizing a re-growth process. The material of choice here is compound semiconductor material such as GaAs, InGaAs, or InP. Potentially, this approach would produce faster smart-pixels; however, there exist difficulties in the simultaneous optimization of both the electronic and optical circuits on the same substrate. Direct epitaxy of compound semiconductors onto silicon is another approach. The problems here are typically a result of lattice mismatch and differences between the coefficients of thermal expansion between the two materials. For example, the lattice mismatch between silicon and GaAs is 4% while the thermal expansion coefficients differ by 50%, resulting in a potentially unstable bond between the two dissimilar materials. Catastrophic failure of these devices typically occurs at this interface as a result of stress, strain, and sheer of the crystalline material. Hybrid processing is the third approach to developing smart-pixels. Here the optical devices are grown separately from the silicon electronic circuitry. Then in a subsequent processing step, the optical devices are bonded to the silicon circuitry using a variety of bonding techniques. These include flip-chip bonding, epitaxial lift-off and subsequent Van der Waals (contact) bonding, and creating a physical cavity above the silicon circuitry and flowing-in optical material such as liquid crystal

material. Using this third approach, both the optical devices and the electronic circuits can be independently optimized resulting in an overall optimization of the smart-pixel.

2   Current Smart-Pixel Research

Over the past two years, we have focused our research efforts on designing, characterizing, and incrementally improving a smart pixel implementation of the error diffusion neural network based on a specific hybrid integration technique. In this research, self-electrooptic-effect device (SEED) multiple quantum well (MQW) modulators are flip-chip bonded to complimentary metal-oxide-semiconductor (CMOS) very large scale integration (VLSI) silicon circuitry to create the CMOS-SEED smart pixel.

5×5 CMOS-SEED Smart Pixel Array

Here, we report on the results of two consecutive generations of CMOS-SEED smart pixel arrays. The first generation CMOS-SEED array consisted of a 10 × 10 array of SEED MQW modulators integrated with 0.8 μm CMOS silicon circuitry while the second generation integrated an identical SEED array with 0.5 μm CMOS silicon circuitry. The focus of both of these designs was to demonstrate the usefulness of smart pixel technology to this specific analog neural application. Although optical weighting and interconnections are clearly the preferred method of achieving the necessary neural interconnections, neither of these designs incorporated this approach. Instead, electronic weighting and interconnections were incorporated in the design with analysis focused on optimizing the specific performance of the analog neural circuitry and the receiver and driver circuitry for the optical input and output signals, respectively. In a parallel effort within this research program, diffractive optical weighting and interconnections have recently been designed and experimentally characterized for a future smart pixel architecture. An overview of these results will be presented later in this report.

First-Generation CMOS-SEED

The functionality necessary to implement the error diffusion neural network consists of a one-bit quantizer, two differencing nodes, and the interconnection and weighting of the error diffusion filter. Figure 1 shows the first-generation circuitry for a single neuron of the error diffusion neural network using the CMOS-SEED smart pixel technology. All state variables in each circuit are represented as currents. Beginning in the upper-left of the circuit and then proceeding in, the input optical signal incident on the SEED is continuous in intensity and represents the individual analog pixel intensity. The input SEED at each neuron converts the optical signal to a photocurrent and subsequently, current mirrors are used to buffer the input. The width-to-length ratio of the metal oxide semiconductor field effect transistors (MOSFETs) determine the current gain used to amplify the photocurrent. The first circuit produces two output signals: $+I_u$ which represents the state variable $u(m,n)$ as the input to the quantizer and $-I_u$ which represents the state variable $-u(m,n)$ as the input to the feedback differencing node. The function of the quantizer is to provide a smooth, continuous thresholding function for the neuron producing the output signal I_{out} which corresponds to the state variable $y(m,n)$. This second electronic circuit is a modified wide-range transconductance amplifier which produces a hyperbolic tangent sigmoidal function when
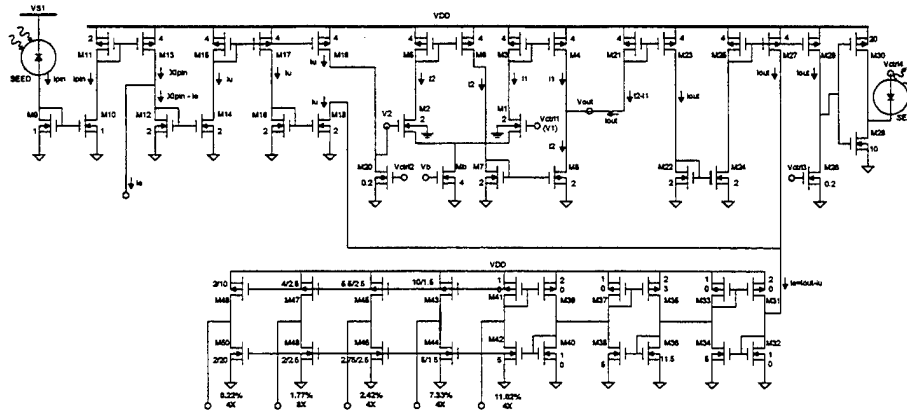
Figure 1. Circuit diagram for the first-generation smart pixel implementation of the error diffusion neural network based on a CMOS-SEED-type smart pixel architecture.

operated in the sub-threshold regime. Additional transistors are included in the modification to provide input current to output current functionality. The third circuit takes as its input I_{out}, the state variable $y(m,n)$, produces a replica of the original signal, and drives an output optical SEED. In this case, the output optical signal is a binary quantity represented as the presence or absence of light. Here, the photoemission process is electroluminescence which results from the SEED being forward-biased. The last circuit at the bottom of the schematic implements the error weighting and distribution function of the error diffusion filter. The weighting is implemented by again, scaling the width-to-length ratio of the MOSFETs to achieve the desired weighting coefficients. The neuron-to-neuron interconnections are accomplished using the four metalization layers of the 0.8 μm silicon CMOS process. The difficulty encountered using this weighting and interconnect approach was that we were forced to constrain the size of the diffusion kernel to a 5 × 5 array because of the physical extent of the circuitry necessary to implement this functionality. Even with this reduced filter kernel, the weighting and interconnect circuitry consumed over 75% of the total silicon area. As a result, a smaller filter with a 5 × 5 region of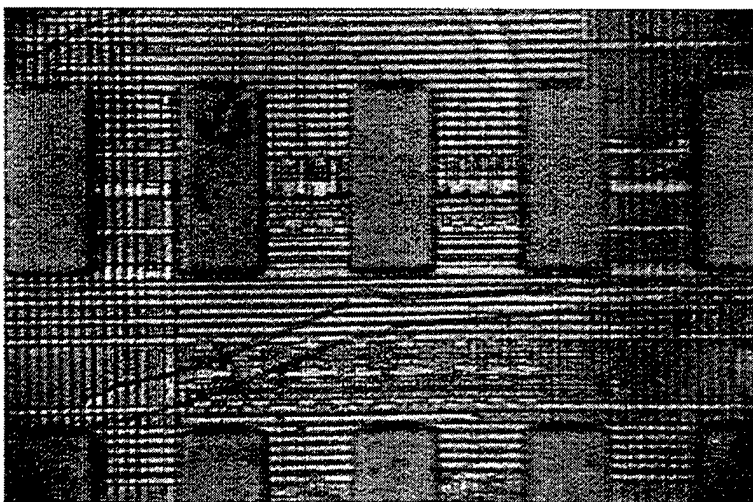 support was designed and these coefficients were used in the smart pixel architecture. The five unique coefficients in this filter are shown at the bottom of the error diffusion circuitry along with the number of additional replications necessary to implement the 5 × 5 filter.

Figure 2 shows a photomicrograph of a single neuron of the first-generation error diffusion neural network. This smart pixel implementation resulted in a network with approximately 90

Figure 2. Photomicrograph of a single neuron of the 5 × 5 error diffusion neural network.

transistors per smart pixel and a total transistor count of nearly 1800. A total of 50 optical input / output channels are provided in this implementation. The rectangular features are the MQW modulators while the silicon circuits are visible between the modulators. The MQW modulators are approximately 70 μm × 30 μm and have optical windows which are 18 μm × 18 μm. Experimental testing of this first-generation smart pixel array confirmed electrical functionality of the quantizer operation as well as the replication features of the current mirrors within the architecture. We have also verified and characterized the electroluminescence of the SEED modulators. These experimental results demonstrated the importance of transistor matching within the wide-range transconductance amplifier and the error weighting circuitry. The results from this first-generation design and characterization were incorporated into the second-generation design in an effort to improve individual circuit operation and, as a result, improve overall network performance.

Second-Generation CMOS-SEED

In the design of the second-generation CMOS-SEED smart pixel, we concentrated on improving the performance of the neural circuitry. Specifically, we improved the error weighting circuitry and the quantizer performance. We also attempted to accurately model the operation of each of the functional elements as well as the total nonlinear network performance using SPICE simulation tools. The same 5 × 5 array size and functionality of one-bit quantization, subtraction, neuron-to-neuron weighting and interconnection, and optical input and output were retained. The electronic circuitry for the error diffusion neural network was implemented this time in 0.5 μm silicon CMOS technology. Figure 3 shows the circuitry associated with a single neuron of this second-generation error diffusion neural network. The one-bit quantizer is again implemented using a modified wide-range transconductance amplifier operated in the sub-threshold regime. The slope of this sigmoidal function was carefully designed by matching MOSFET transistors to meet the convergence criteria and the nonlinear dynamics of the error diffusion neural network. The error weighting circuitry at the bottom represents only the largest weight (11.02%) with interconnects to its four local neighbors (I_{outA} - I_{outD}).
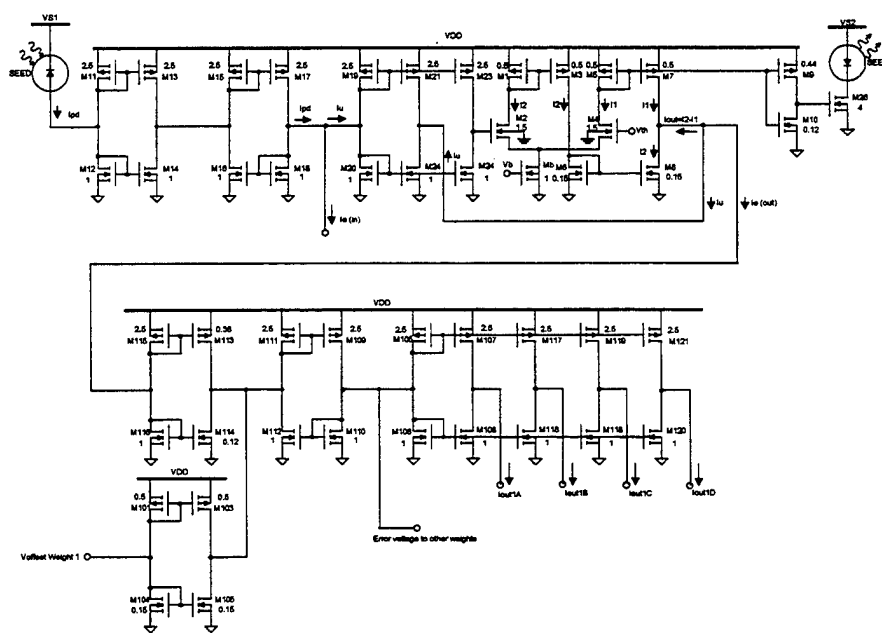

Figure 3. Circuit diagram of a single neuron and a single error weight of the 5 × 5 error diffusion neural network based on a CMOS-SEED-type smart pixel architecture.

Again, all state variables are represented as currents. The error weighting and distribution circuitry for the 5 × 5 array was again implemented in silicon circuitry, matching individual and stage-to-stage MOSFET transistors. Bi-directional error currents were implemented to provide the circuitry and the network with fully-symmetric performance. The specific improvements to the second-generation circuitry include improving stage-to-stage isolation by tying the drain and source of selected transistors together, as seen with transistors M19 and M20 in the schematic. This configuration places a constraint on the common node which helped isolate adjoining stages. This was particularly important to accurate circuit operation since the design of the wide-range transconductance amplifier required small feature size transistors compared to the input buffer and error weighting circuitry. In the circuit layout, we also changed several of the transistors in the wide-range transconductance amplifier to ensure that small width-to-length ratios were used in an effort to minimize channel length modulation effects. The SEED driver circuit was redesigned to provide additional isolation between the large currents used to forward bias the SEED and the balance of the sensitive neural circuitry. Finally, we accurately matched transistor characteristics throughout the network using extracted transistor data from a previous 0.5 μm foundry run.

The central neuron of this new smart pixel array consists of approximately 160 transistors while the complete 5 × 5 array accounts for over 3600 transistors, a nearly two-fold increase in the total transistor count over our first-generation design. The central neuron is interconnected to the surrounding 24 neurons in the 5 × 5 array using the same fixed interconnect and weighting scheme as in the first-generation realization. SPICE simulations of the complete 5 × 5 nonlinear dynamical neural network were performed using transistor parameters extracted from a previous 0.5 μm MOSIS foundry. Figure 4 shows the SPICE simulation for the performance of the complete 5 × 5 array to a linear input signal. As the input signal is linearly increased over the input dynamic range, the number of neurons in the *on*-state increases from 0 to 25, representing the analog input level at any given time interval as the ratio of the number of neurons in the *on*-state to those in the *off*-state. The non-uniform rate of increase in the number of neurons in the *on*-state is predictable and is a result on the artificially small network size. Figure 5 shows an expanded segment of Figure 4 which provides an analysis of the transient behavior of the network. These simulations predict individual neuron switching speeds of less than 1 μs demonstrating the capability for real-time digital image halftoning.

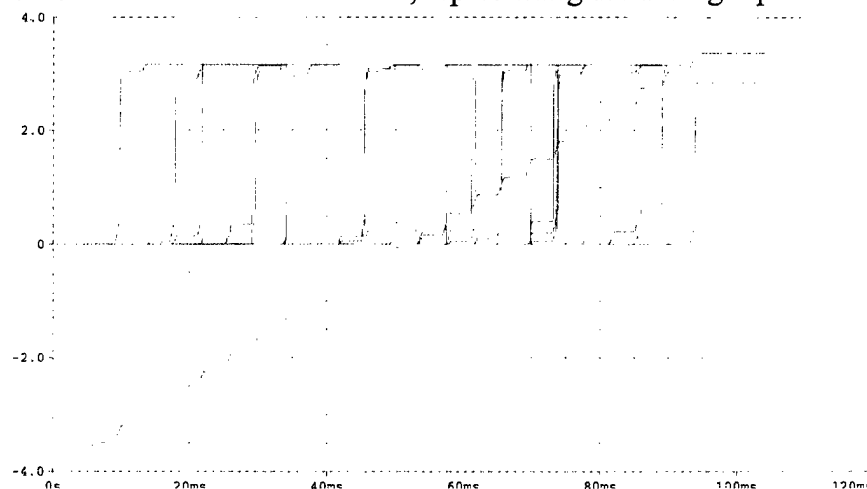**Figure 4.** Dynamic performance characterization of the 5 × 5 error diffusion neural network to a stepped linear input.

Individual component functionality was experimentally characterized and dynamic operation of the full 5 × 5 neural array was experimentally characterized. Dynamic stimulus of single and multiple neurons was also conducted and demo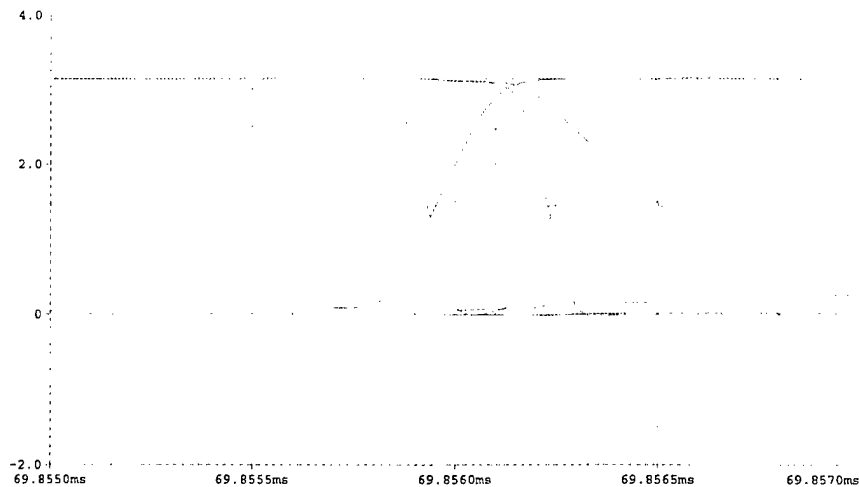nstrated correct error diffusion and network operation. Figure 6 shows CCD images of the operational 5 × 5 CMOS-SEED smart pixel array. Figure 6(a) shows the fully-functioning array while Figure 6(b) shows the 5 × 5 CMOS-SEED neural array under 50% gray-scale input. Here 50% of the SEED modulators are shown to be in the on-state.

Figure 5. Transient analysis of 5 × 5 network. performance.

Both the SPICE simulations and the experimental results demonstrate that this approach to a smart pixel implementation of the error diffusion neural network provides sufficient accuracy for the digital halftoning application. The individual neuron switching speeds also demonstrate the capability for this smart pixel hardware implementation to provide real-time halftoning of video images.

(a) (b)

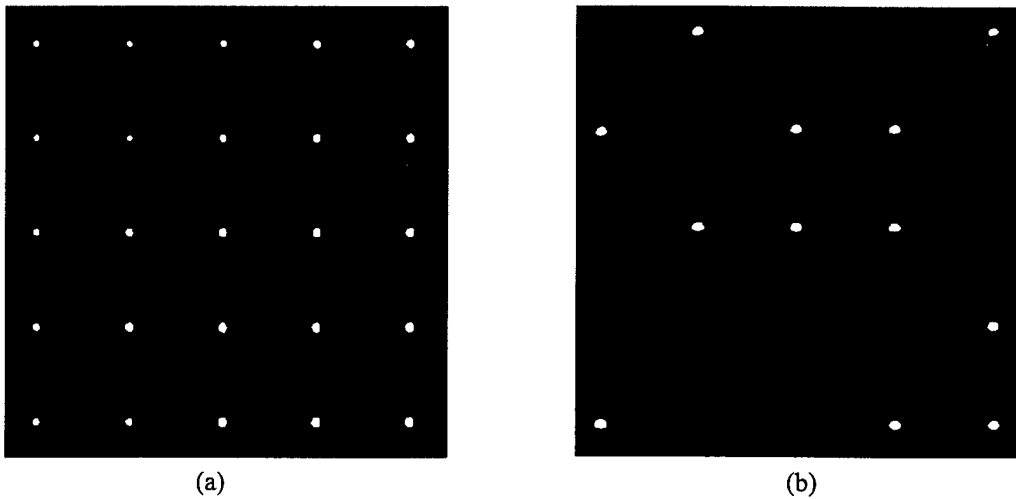**Figure 6.** CCD images of the 5 × 5 CMOS-SEED array (a) fully-operational array and (b) under 50% gray scale illumination.

3 Summary and Observations

Through this research, we have successfully demonstrated the applicability of smart pixel technology to this specific mixed-signal neural network application. The experimental results confirm individual functionality as well as correct network operation of the hardware

implementation of the error diffusion neural network. The switching speed of the individual transistors in conjunction with the convergence speed of the neural network confirms that this hardware approach to implementing the error diffusion neural network can provide real-time processing speeds for the digital image halftoning application. Extensions of this work include scaling the smart pixel array to larger array sizes and investigating the extension of the smart pixel error diffusion neural network to the application of high-resolution A/D conversion using spatial oversampling techniques. We will also be investigating the integration of optical weighting and interconnection of the neural array using diffractive optical filters which is a parallel research effort focused on increasing the fill-factor of the smart pixel array.

Publications and Conference Presentations

1. D. A. Hall, B. L. Shoop, J. Loy, E. K. Ressler, J. Ahadian, and C. Fonstad, Jr., "Performance of GaAs smart pixel components before and after monolithic integration of InGaP LEDs using Epitaxy-on-Electonics technology," *Optics Express*, vol. 4, pp. 151-160, February 1999.
2. B. L. Shoop, T. D. Wagner, J. N. Mait, G. R. Kilby, and E. K. Ressler, "Design and analysis of a diffractive optical filter for use in an optoelectronic error diffusion neural network," *Applied Optics*, vol. 38, pp. 3077-3088, May 1999.
3. B. L. Shoop, R. W. Sadowski, G. P. Dudevoir, E. K. Ressler, A. H. Sayles, D. A. Hall, and D. M. Litynski, "Smart pixel technology and an application to two-dimensional analog-to-digital conversion," *Optical Engineering*, vol. 37, pp. 3175-3186, December 1998.
4. G. R. Kilby, B. L. Shoop, J. N. Mait, T. D. Wagner, and E. K. Ressler, "Experimental characterization of a diffractive optical filter for use in an optoelectronic analog-to-digital converter," *Optics Communications*, vol. 157, pp. 1-6, December 1998.
5. P. K. Das, B. L. Shoop, and D. M. Litynski, "Optical A/D converter and wavelet transform implementation using smart pixels," Proceedings of the International Conference on Optics & Optoelectronics, pp. 54-56, December 1998.
6. B. L. Shoop, D. A. Hall, D. M. Litynski, P. K. Das, and C. DeCusatis, "Applications of smart pixel technology to image compression for optical data compression," *Invited Presentation* in OSA Annual Meeting Technical Digest, 1998, (Baltimore, Maryland) October 1998.
7. T. R. Moore, R. L. Blair, A. J. Megofna, M. P. Reigner, and B. L. Shoop, "Holographic interferometers with photorefractive recording media," *Applied Optics*, vol. 37, pp. 5176-5183, August 1998.
8. B. L. Shoop, P. K. Das, and D. M. Litynski, "Improved resolution of photonic A/D conversion using oversampling techniques," *Proceedings of the SPIE*, vol. 3463, pp. 192-199, November 1998.
9. D. M. Litynski, B. L. Shoop, D. A. Hall, P. K. Das, and C. DeCusatis, "Optical implementation of the wavelet transform using smart pixels," *Proceedings of the SPIE*, vol. 3581, pp. 188-195, November 1998.

10. P. K. Das, C. DeCusatis, B. L. Shoop, D. M. Litynski, "Acousto-photorefractive holographic interferometric correlator for progressive pattern recognition using wavelet transforms," *Proceedings of the SPIE*, vol. 3470, pp. 214-225, October 1998.

Acknowledgments

Collaboration

West Point, Department of Electrical Engineering and Computer Science
1. Major Dirk A. Hall
2. Major James J. Raftery, Jr.
3. Major Robert W. Sadowski
4. Lieutenant Colonel Glen P. Dudevoir
5. Dr. Timothy J. Talty
6. Colonel Andre H. Sayles
7. Colonel Daniel M. Litynski

Rensselaer Polytechnic Institute
1. Professor Pankaj K. Das

THE ERROR DIFFUSION NEURAL NETWORK: THEORY AND EXTENSIONS

LTC EUGENE K. RESSLER, DR. JEAN R. S. BLAIR, DR. THOMAS D. WAGNER,
LTC DAVID A. NASH, AND LTC BARRY L. SHOOP

Department of Electrical Engineering and Computer Science and Photonics Research Center
United States Military Academy, West Point, New York 10996
E-mail: Barry-Shoop@usma.edu

Extensions and applications of the error diffusion neural network are investigated in this research. Extensions from black-and-white halftoning to color halftoning and further to multispectral and hyperspectral applications extend the usefulness of the error diffusion algorithm to new and important military applications. Using the error diffusion neural network to provide other useful image processing functionality including edge detection is also considered in this work. Recent extensions include partitioning of the original image into smaller sub-images for subsequent processing has proven to be useful in reducing the computational time which is important for the smart pixel hardware development being developed in a parallel research effort.

1 Introduction

Digital halftoning, sometimes referred to as spatial dithering, is the process by which a continuous-tone, gray-scale image is rendered using only binary-valued pixels. The underlying concept is to provide the viewer of the image the illusion of viewing a continuous-tone image when, in fact, only black and white pixel values are used in the rendering.

There are a number of different methods by which this digital image halftoning can be accomplished. Ordered dither, produces an output by comparing a single continuous-tone input value against a deterministic periodic array of threshold values. Dispersed-dot ordered dither occurs when the halftone dots are of a fixed size, while clustered-dot ordered dither simulates the variable-sized dots of printer's halftone screens in the rendering. Among the advantages of ordered dither techniques are speed of implementation and simplicity. The primary disadvantage is that ordered dither produces locally periodic patterns in the halftoned image which are visually objectionable. In contrast, halftoning using the error diffusion algorithm, first introduced by Floyd and Steinberg [1], requires neighborhood operations and is currently the most popular neighborhood halftoning process. In this algorithm, the error of the quantization process is computed and spatially redistributed within a local neighborhood in an effort to influence pixel quantization decisions within that neighborhood and thereby improve the overall quality of the halftoned image. Classical approaches to error diffusion, however, suffer from implementation constraints. Here, the algorithm raster scans the image, and for each individual pixel, a binary quantization decision is made based on the intensity of the individual pixel and the weighted error from pixels within a predefined diffusion region of previously processed pixels. As a result, the diffusion filter is necessarily causal resulting in undesirable visual artifacts. In an effort to improve halftone image quality, Anastassiou [2] proposed the use of an error diffusion neural network to provide a mechanism for symmetric error diffusion. However, analysis of this first network's dynamic behavior was considered difficult and convergence and stability issues in conjunction with implementation constraints limited its usefulness.

2 The Error Diffusion Neural Network

The popularity of the neural network-based approach lies in the ability to minimize a particular metric associated with a highly nonlinear system of equations. Specifically, the problem of creating a halftoned image can be cast in terms of a nonlinear quadratic optimization problem where the performance metric to be minimized is the difference between the original and the halftoned images.

The Hopfield-Type Neural Network

The dynamic behavior of an N-neuron Hopfield-type neural network can be described by the following system of N nonlinear differential equations:

$$c\frac{du_i(t)}{dt} = -u_i(t) + \sum_j T_{i,j}\Im\big[u_j(t)\big] + x_i, \tag{1}$$

where $i=1,2,...\ N$, $\Im[\cdot]$ is a monotonically increasing sigmoid function, x_i is an input N-vector, and c is a scaling factor. In equilibrium, Equation (1) implies

$$u_i = x_i + \sum_j T_{i,j}\Im\big[u_j\big]. \tag{2}$$

Hopfield showed that when the matrix of interconnection weights $\mathbf{T}$ is symmetric with zero diagonal elements and the high-gain limit of the sigmoid $\Im[\cdot]$ is used, the stable states of the N functions $y_i(t) = \Im\big[u_j\big]$ are the local minima of the energy function [3]

$$E = -\frac{1}{2}\mathbf{y}^T\mathbf{T}\mathbf{y} - \mathbf{x}^T\mathbf{y} \tag{3}$$

where $\mathbf{y} \in \{-1,1\}$ is an N-vector of quantized states.

The Error Diffusion Neural Network

Figure 1 shows the block diagram of a 2-D error diffusion architecture and an electronic implementation of a four-neuron error diffusion-type neural network. Here the individual neurons are represented as amplifiers and the synapses by the physical connections between the input and output of the amplifiers.
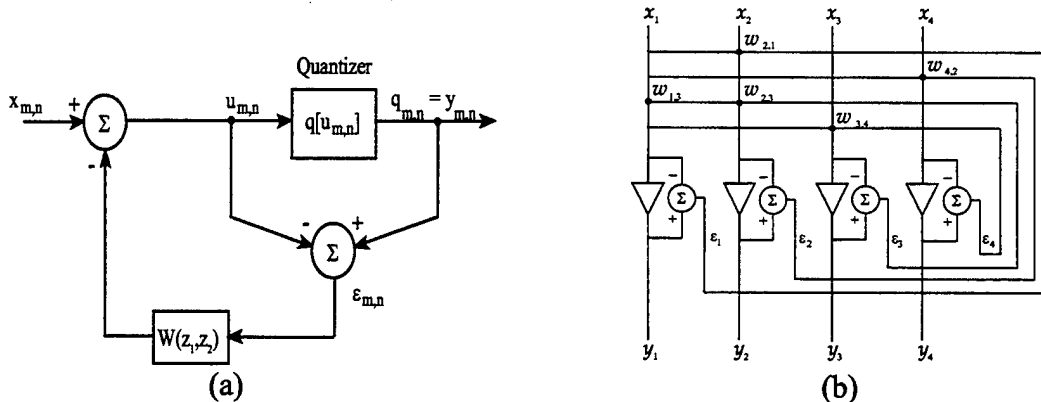

Figure 1. (a) Block diagram of a 2-D error diffusion architecture, (b) Four-neuron electronic implementation. In equilibrium, the error diffusion neural network satisfies

$$\mathbf{u} = \mathbf{W}(\mathbf{y} - \mathbf{u}) + \mathbf{x}. \tag{4}$$

15-2

For an $N \times N$ image, $\mathbf{W}$ is an $N^2 \times N^2$ sparse, circulant matrix derived from the original error diffusion weights $w_{i,j}$. If we define the coordinate system such that the central element of the error diffusion kernel is $(i, j) = (0,0)$, then the matrix $\mathbf{W}$ is defined as
$W(i, j) = -w[(j - i) \operatorname{div} N, (j - i) \operatorname{mod} N]$ where

$$x \operatorname{div} y = \left\lfloor \frac{x}{y} \right\rfloor \text{ if } xy \geq 0 \text{ or } \left\lceil \frac{x}{y} \right\rceil \text{ if } xy < 0 \tag{5}$$

An equivalence to the Hopfield network can be described by

$$\mathbf{u} = \mathbf{A}(\mathbf{W}\mathbf{y} + \mathbf{x}), \tag{6}$$

where $\mathbf{A} = (\mathbf{I} + \mathbf{W})^{-1}$. Effectively, the error diffusion network includes a pre-filtering of the input image $\mathbf{x}$ by the matrix $\mathbf{A}$ while still filtering the output image $\mathbf{y}$ but now with a new matrix, $\mathbf{AW}$. Recognizing that $\mathbf{AW} = \mathbf{I} - \mathbf{A}$ and adding the arbitrary constant $k = \mathbf{y}^T\mathbf{y} + \mathbf{x}^T\mathbf{A}\mathbf{x}$, we can write the energy function of the error diffusion neural network as

$$E = (\mathbf{y} - \mathbf{x})^T \mathbf{A}(\mathbf{y} - \mathbf{x}). \tag{7}$$

From Equation (7) we find that as the error diffusion neural network converges and the energy function is minimized, so too is the error between the output and input images. Computing the Fourier transform of this energy function we find that the error diffusion neural network minimizes the frequency weighted squared error between the output and input images. If the neurons update independently, the convergence of the error diffusion network is guaranteed if

$$\forall k : [\mathbf{AW}]_{k,k} \geq 0. \tag{8}$$

We find in practice, that even in a synchronous implementation, the halftoned images converge to a solution which results in significantly improved halftone image quality over other similar halftoning algorithms.

The Error Diffusion Filter

The purpose of the error diffusion filter is to spectrally shape the quantization noise in such a way that the error resulting from the quantization process is distributed to higher spatial frequencies which are less objectionable to the human visual system. In this application, the feedback filter for the error diffusion neural network was designed using conventional two-dimensional filter design techniques and resulted in the impulse response and frequency response shown in Fig. 2(a) and (b), respectively.

0.0005	0.0020	0.0052	0.0069	0.0052	0.0020	0.0005
0.0020	0.0104	0.0249	0.0329	0.0249	0.0104	0.0020
0.0052	0.0249	0.0584	0.0767	0.0584	0.0249	0.0052
0.0069	0.0329	0.0767	•	0.0767	0.0329	0.0069
0.0052	0.0249	0.0584	0.0767	0.0584	0.0249	0.0052
0.0020	0.0104	0.0249	0.0329	0.0249	0.0104	0.0020
0.0005	0.0020	0.0052	0.0069	0.0052	0.0020	0.0005
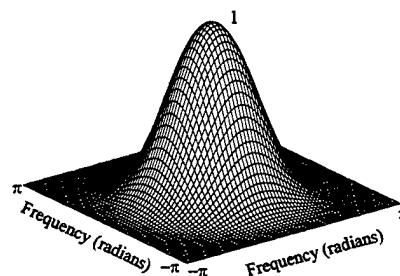
(a)   (b)

Figure 2. (a) Impulse response and (b) frequency response of one specific 7×7 error diffusion filter. ("•" represents the origin)

Figures 3(a) and (b) show 348×348 halftoned images of the Cadet Chapel at West Point using classical halftoning techniques and our error diffusion neural network, respectively. Notice the uniformity of the pixel distributions in the upper-left of Figure 3(b) in the cloud structure and also the improvement in the rendering of edges throughout the image. Figure 3(b) represents an *artifact-free* halftone image.
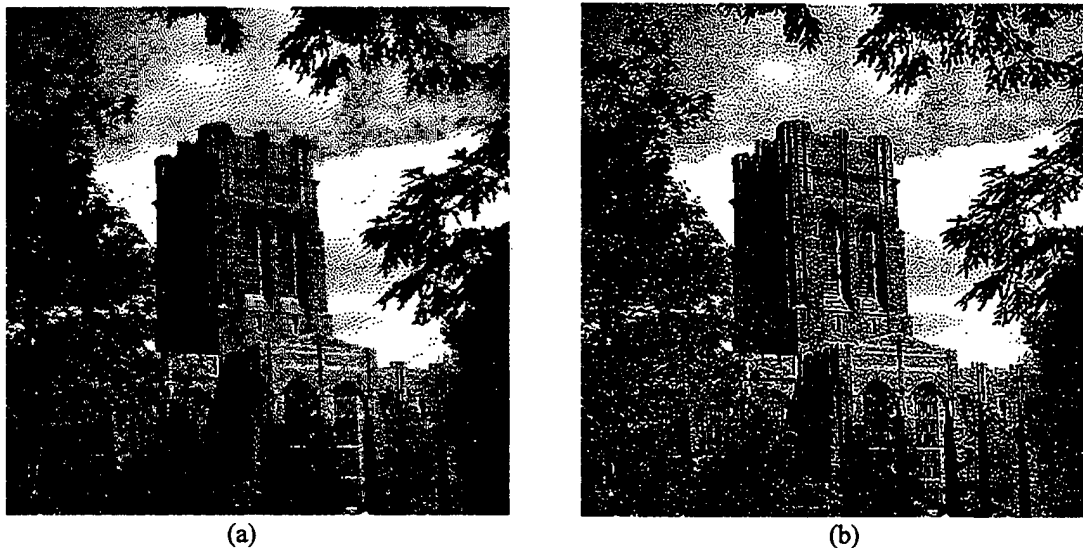

(a)   (b)

Figure 3. Halftoned images of the Cadet Chapel at West Point. (a) using classical error diffusion, and (b) using our error diffusion neural network.

3 Color Extensions

We have also investigated the applicability of the error diffusion neural network to color halftoning, demonstrating excellent color image reproduction while simultaneously achieving a modest image compression ratio of 8:1. To date, the color halftoning has been a simple extension achieved by simply implementing three independent error diffusion networks in parallel, one for each of the primary colors in the image.

4 A Partitioning Approach to Neural Halftoning

From a practical point of view, a problem with the error diffusion network approach to digital halftoning is that it requires one node in the neural network for each pixel in the image; that is, there must be a one-to-one mapping between each pixel in the image and each neuron in the network. Further, each node needs to be physically connected to $q \times q\text{-}1$ of its nearest neighbors, where q is the error diffusion filter size. This permits successive iterations of the network to diffuse the error throughout the halftoned image. Because the error diffusion neural network is a full-rank network, the propagation of error is dependent on error everywhere else in the network, not only at each of the $q \times q\text{-}1$ neighbors. The limiting factor in determining the practicality of this approach to halftoning is the size limitation imposed by hardware. Physical realizations of this network using current smart pixel technology would limit the size to approximately 100×100 pixels. Unfortunately, few images of interest could be processed under those limitations. In fact, if one assumes no more than 300 dpi resolution,

an 8.5 in × 11 in image would require 2550 × 3300 pixels, more than two orders of magnitude larger than the hardware implementation. For these reasons, halftoning of images of non-trivial size using this neural network approach is primarily accomplished through a software implementation, which can be noticeably slow for large images. A factor in the time complexity for software implementations of this neural network is the number of iterations before convergence occurs. It has been shown that this number is bounded above by $(n \times m)^2$, where $(n \times m)$ is the number of pixels in the image. Clearly, a general strategy for maximizing performance seeks to minimize the size of the input image. To be fully general though, one cannot insist on input images of any particular size. Thus we must pursue alternatives that impose essentially no constraints on the size of the input image.

Figure 4 shows the general approach to partitioning input images for this tiling purpose.

(a)

(b)
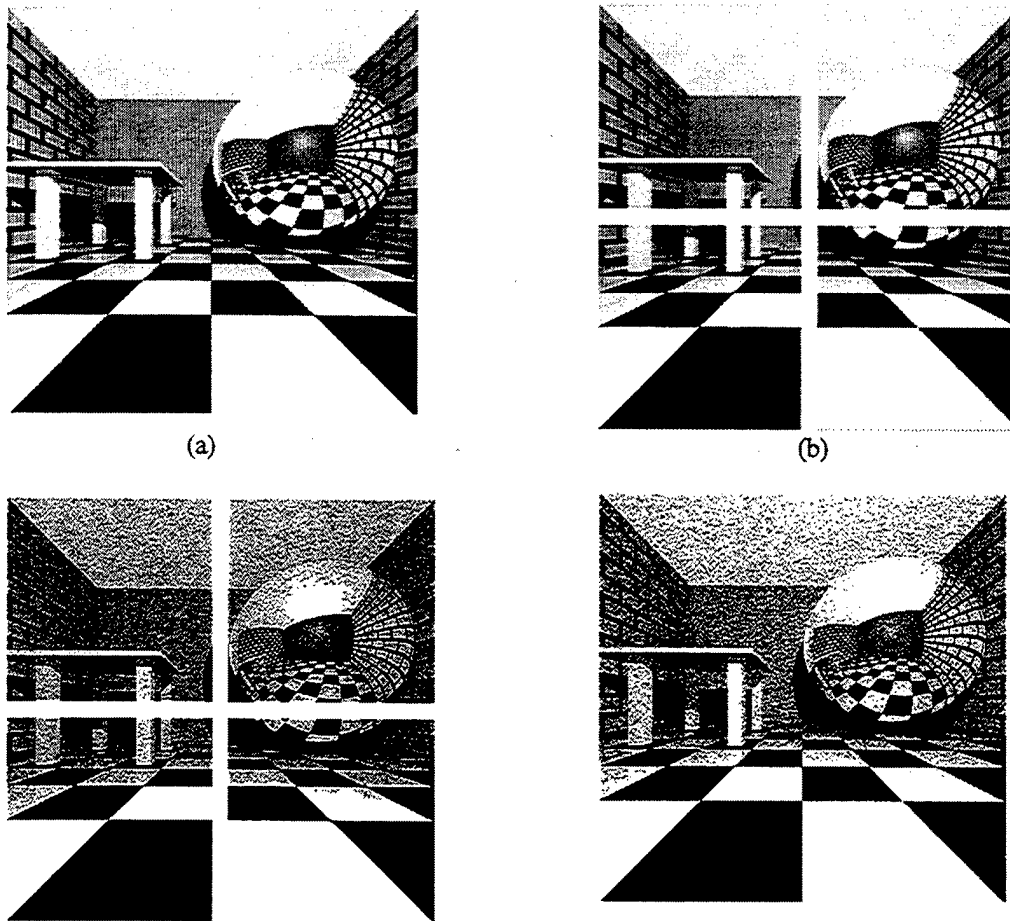
Figure 4. Graphical description of tiling. (a) Original gray-scale image, (b) partition of the original image into tiles, (c) resulting halftone of each tile, (d) tiles combined into final image.

We have investigated several different tiling methodologies from simple partitioning to framing to constrained framing [4]. The approach that has demonstrated the best performance introduces constraints on the halftones of neighboring tiles so that communication of errors across tile edges occurs, with a goal of making the halftoned image appear seamless. This approach breaks the original image into tiles, however, execution of

the error diffusion neural network on individual tiles is not independent. For this approach, tiles must be processed in some specified order. For simplicity, assume the individual tiles are processed in left-to-right, top-to-bottom order. The network is executed on the first, upper left hand tile with the halftoned tile being made up of three parts, as shown in Figure 5.
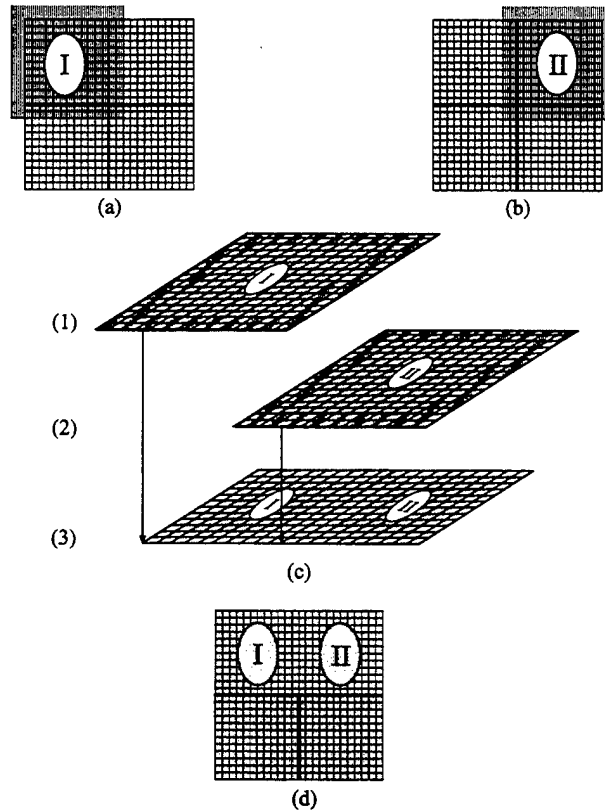

Figure 5. Constrained framing approach to tiling.

The outermost frame is the extra h pixels that will be discarded. The inner frame is made up of halftoned portions that will be used as constraints on the processing of adjacent tiles. This inner frame, together with the innermost square shape, contains the final halftoned values for the first tile. To process the second tile, we again use the second tile with a frame from the original grayscale. However, in this case the network also uses a constraint buffer to maintain halftone values along the frame that are equal to those computed during the processing of the first tile. We implemented these constraints by setting the computed halftone values for the pixels in the constrained frame to the values in the constraint buffer after each iteration of the EDN. The result of processing the second tile is a halftoned tile with frame where the left edge of the frame contains values that are exactly the same as the halftoned values for the corresponding pixels in the first tile. Processing of subsequent tiles continues in like fashion, with the constraint buffer for each tile being filled by the appropriate already-computed halftones from adjacent tiles. This approach results in halftoned images whose quality are comparable with images halftoned using the error diffusion neural network without tiling. Further, by partitioning the original image into k subimages, the time required to perform the halftoning using this approach is reduced by as

much as a factor of k. This result is significant and directly applicable to the smart pixel hardware development.

3 Summary and Observations

We are currently investigating extensions of the error diffusion neural network to areas including color halftoning and tiling. The color halftoning extension will include an investigation of an optimal approach to halftoning of color images, considering human color perception and the relationship and interconnectivity between the three individual networks. A theoretical analysis of this three-dimensional neural network is necessary to address such issues as convergence, stability, and network dynamics. Performance metrics must also be considered, providing quantitative results by which to compare these color halftoning results. A logical extension of this color halftoning which will also be investigated is an extension to more than three primary colors and the relationship to multi-spectral imagery and image compression. Other novel applications are also being investigated including edge enhancement using the error diffusion neural network with a modified error diffusion filter. These extensions hold promise for improving the computational speed of the neural network and extending this research to other military applications.

References

1. R. Floyd and L. Steinberg, "An Adaptive Algorithm For Spatial Gray Scale," *SID 75 Digest* 36, 35-36 (1975).
2. D. Anastassiou, "Error diffusion coding for A/D conversion," *IEEE Trans. Circuits Syst.*, vol. 36, pp. 1175-1186, 1989.
3. D.W Tank and J.J. Hopfield, "Simple neural optimization networks: A/D converter, signal detection circuit, and linear programming circuit," *IEEE Trans. Circuits Syst.*, 33, 533-541 (1986).
4. J. R. S. Blair, T. D. Wagner, D. A. Nash, E. K. Ressler, B. L. Shoop, and T. J. Talty "Partitioning schemes for use in a neural network for digital image halftoning," *Proceedings of the SPIE*, vol. 4055, pp. 36-48, 2000.

Acknowledgments

Selected Publications and Conference Presentations

1. J. R. S. Blair, T. D. Wagner, D. A. Nash, E. K. Ressler, B. L. Shoop, and T. J. Talty "Partitioning schemes for use in a neural network for digital image halftoning," *Proceedings of the SPIE*, vol. 4055, pp. 36-48, 2000.
2. T. D. Wagner, D. A. Nash, J. R. S. Blair, E. K. Ressler, and B. L. Shoop, "A partitioning scheme for optoelectronic neural networks," in Proceedings of the IEEE LEOS 2000 Summer Topical Meeting on Electronic-Enhanced Optics, July 2000.

West Point Collaborators, Department of Electrical Engineering & Computer Science

1. Dr. Jean R. S. Blair
2. Dr. Thomas D. Wagner
3. LTC David A. Nash, Ph.D.
4. LTC Eugene K. Ressler, Ph.D.
5. Dr. Timothy J. Talty

PHOTONIC A/D CONVERSION BASED ON A FULLY-CONNECTED, DISTRIBUTED MESH FEEDBACK ARCHITECTURE

LTC BARRY L. SHOOP

Department of Electrical Engineering and Computer Science and Photonics Research Center
United States Military Academy, West Point, New York 10996
E-mail: Barry-Shoop@usma.edu

A novel approach to photonic A/D conversion using a distributed neural network, oversampling techniques, and a smart pixel hardware implementation is described. In this approach, the input signal is first sampled at a rate higher than that required by the Nyquist criterion and then presented spatially as the input to a two-dimensional error diffusion neural network consisting of M×N neurons, each representing a pixel in the image space. The neural network processes the input oversampled analog image and produces an M×N pixel binary or halftoned output image. By design of the neural network, this halftoned output image is an optimum representation of the input analog signal. Upon convergence, the neural network minimizes an energy function representing the frequency-weighted squared error between the input analog image and the output halftoned image. Decimation and low-pass filtering techniques, common to classic one-dimensional oversampling A/D converters, digitally sum and average the M×N pixel output binary image using high-speed digital electronic circuitry. By employing a two-dimensional smart pixel neural approach to oversampling A/D conversion, each pixel constitutes a simple oversampling modulator thereby producing a distributed A/D architecture. Spectral noise shaping across the array diffuses quantization error thereby improving overall signal-to-noise ratio (SNR) performance. Here, each quantizer within the network is embedded in a fully-connected, distributed mesh feedback loop which spectrally shapes the overall quantization noise thereby significantly reducing the effects of component mismatch typically associated with parallel or channelized A/D approaches. The two-dimensional neural array provides higher aggregate bit rates which can extend the useful bandwidth of photonic-based, oversampling A/D converters.

1 Introduction

The analog-to-digital (A/D) converter is a key element in any electronic or photonic system which senses the natural environment and processes, stores, or displays the information using digital techniques. Since the vast majority of signals in nature are analog and the preferred method of processing, storing, and transmitting signals is digital, this interface is critical to the success of the overall system. Because of the difficulty in achieving high-resolution and high-speed A/D converters, this A/D interface has been and continues to be a barrier to the realization of high-speed, high-throughput systems.

There has recently been renewed interest in new and innovative approaches to A/D conversion, with a significant emphasis on photonic techniques. The potential advantages of using photonics technology come in the form of high-speed clocking, broadband sampling, reduced mutual interference of signals, and compatibility with existing photonic-based systems. Photonic approaches to A/D conversion have been considered in the past with varying degrees of success. Some of the approaches employed Mach-Zehnder interferometers, others incorporated acoustooptic modulators, and recently multiple quantum well modulators have been incorporated into non-traditional architectures.

With the tremendous success of oversampling A/D converters in the audio industry, there has been increased interest in the extension of these oversampling techniques to high-resolution, high-speed A/D applications. In an effort to achieve the ultra-high speed

16-1

sampling required to extend oversampling techniques beyond audio frequency bandwidths, photonic-based oversampling A/D conversion architectures are being investigated. In an oversampling A/D converter, a low-resolution quantizer is embedded in a feedback architecture in order to reduce the quantization noise through spectral noise shaping, effectively trading bandwidth for improved amplitude resolution. The motivation in integrating photonics technologies to oversampling architectures is to extend the sampling rates beyond what is currently available using conventional electronics technology thereby extending the resolution and possibly the conversion speed of oversampling A/D conversion

2   Oversampling A/D Conversion

Oversampled A/D conversion, most commonly referred to as $\Sigma\Delta-$ or $\Delta\Sigma$-modulation, is an A/D technique which has become popular in the audio industry. This approach relies on a temporal form of error diffusion coding, whereby a large error associated with a single sample is *diffused* over many subsequent samples. Here, the error is generated by a low-resolution quantizer, and the diffusion is implemented by embedding the quantizer and a linear filter in a feedback architecture. Figure 1 shows a generalized block diagram of an oversampled A/D converter. The analog signal $x(t)$ is first bandlimited to the range

$0 \leq f_x \leq f_B$ (Hz) and is then sampled at a rate $f_S \gg f_N$, where f_S is the sampling

frequency, $f_N = 2f_x$ is the Nyquist frequency of the sampled signal, and $f_B \leq f_S/2$ is the constrained signal bandwidth. The output of the sampler is then input to the modulator, which provides coarse amplitude quantization and spectral shaping of the quantization noise. The digital postprocessor, which consists of a digital low pass filter and decimation circuitry, removes the quantization noise which was spectrally shaped by the modulator, provides anti-aliasing protection, and reduces the rate to the original sampled signal's Nyquist rate by trading word rate for word length.
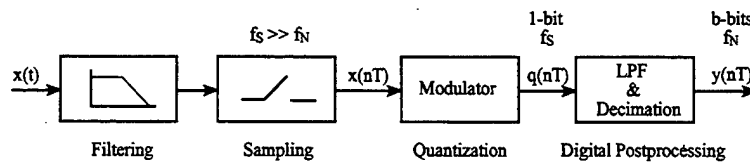
Figure 1. Generalized block diagram of an oversampled A/D converter.

The modulator is the key element of this architecture whose function is to quantize the analog input signal and reduce the quantization noise within the signal baseband. For optical implementations, an alternative architecture to those typically associated with electronic implementations is used in order to reduce optical losses and prevent quantizer overload. Figure 2(a) shows the block diagram of this specific realization called a recursive error diffusion modulator. Here, $H(z)$ represents the Z-transform of a causal, unity gain filter, z^{-1} is a unit sample delay, and q is a low-resolution quantizer. Figure 2(b) shows the noise shaping characteristics for first- and second-order noise shaping filters where $H(z)=1$ and $H(z)=1-2z^{-1}+z^{-2}$, respectively.

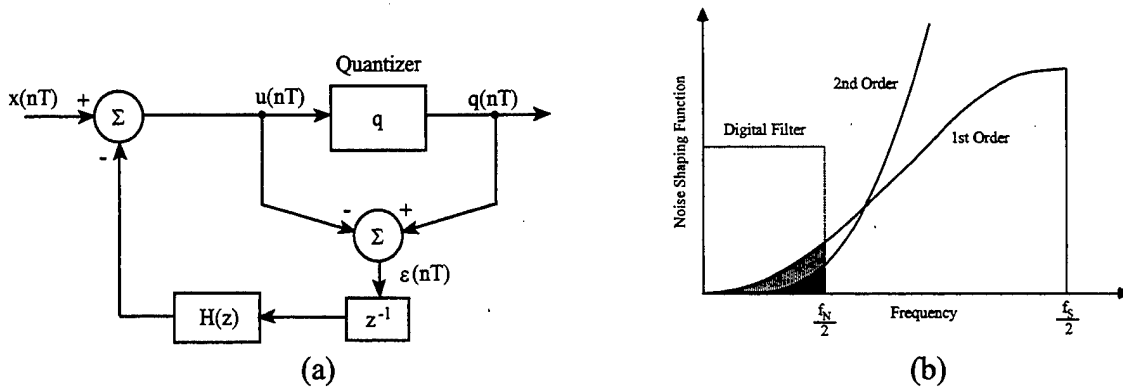**Figure 2.** (a) Block diagram of a recursive error diffusion modulator, and (b) noise shaping characteristics for first- and second-order filters.

The input to the modulator is assumed to be in the range $x_n \in [-b, b)$, where we use the usual definition of the half-open interval $[a, b) = \{x : a \le x < b\}$. It can be shown that for $H(z) = 1$ and assuming a uniform binary quantizer with digital output levels $q(u_n) \in \left\{ +\dfrac{\Delta}{2}, -\dfrac{\Delta}{2} \right\}$, the nonlinear difference equation describing this modulator is

$$q(u_n) = \underbrace{x_n}_{signal} + \underbrace{\varepsilon_n - \varepsilon_{n-1}}_{quantization\ error} . \tag{1}$$

Here the quantity ε_n is the quantization error that would be seen at the modulator output if there were no feedback loop. As a result of the negative feedback, the first-order difference of the error, $\varepsilon_n - \varepsilon_{n-1}$, appears at the output instead. By design, this difference signal is concentrated at high frequencies and can therefore be removed by the digital low pass filter in the postprocessor. If the quantization noise is uncorrelated with the input signal and has statistical moments consistent with a uniform white process, we refer to this process as noise shaping, since only the quantization noise will be affected by the filtering operation.

System Performance

A convenient measure by which to compare an A/D converter's performance is the maximum signal-to-quantization noise ratio $SQNR_{max}$ which is defined as the ratio of the output power at the frequency of a full-scale input sinusoid to the quantization noise power within the signal baseband. In the case of an oversampled A/D converter, analytic evaluation of this expression requires knowledge of the quantizer error spectrum and the postprocessor filter transfer function. If we assume white quantization noise characteristics and an ideal low pass filter with cutoff frequency f_B, the $SQNR_{max}$ for an Nth-order modulator with a full-scale input range of $\pm \Delta / 2$ can be shown to be

$$SQNR_{max}(M, N) = \frac{3}{2} \cdot \left[\frac{2N+1}{\pi^{2N}} \right] \cdot M^{2N+1}, \tag{2}$$

where $M \equiv f_S / f_N$ is defined as the oversampling ratio. A conventional uniform Nyquist rate quantizer with b-bits resolution can be shown to provide a $SQNR_{max}(b) = 3 \cdot 2^{2b-1}$.

Figure 3 shows the theoretical $SQNR_{max}(M, N)$ and equivalent resolution for first- through fourth-order oversampled modulators as a function of oversampling ratio. Results for N=1 are also included because, although the additive noise model does not predict the spectral characteristics of the quantization noise, it does yield accurate results for the $SQNR_{max}$. The case of no noise shaping represents the $SQNR_{max}$ that can be expected if the same quantizer, embedded in the feedback loop of the oversampled modulator, were simply oversampled and digitally filtered. The slope of this curve is 3 B per octave while those of the N=1 and N=2 curves are 9 dB and 15 dB, respectively, showing the significant advantage achieved by using a noise shaping modulator.
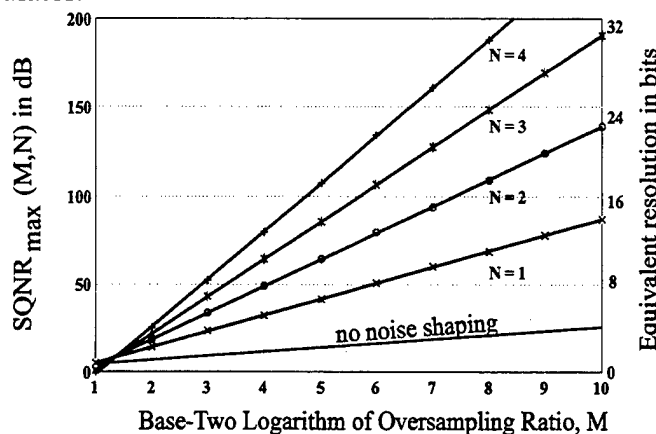

Figure 3. Maximum signal-to-quantization noise ratio of Nth-order modulators.

3 Oversampling, Digital Halftoning, and the Error Diffusion Neural Network

Digital image halftoning is an important class of A/D conversion which can be considered the spatial counterpart of temporal oversampled A/D conversion. In digital halftoning, a continuous-tone input image is spatially oversampled and subsequently processed to produce an output image which is strictly bilevel. The arrangement of the binary output pixels is judiciously chosen such that the resulting halftoned image creates the illusion of a continuous-tone image. There are a number of different approaches to halftoning based on whether the output decision is based on a point process or a neighborhood process. Halftoning using the error diffusion algorithm, first introduced by Floyd and Steinberg [1], uses neighborhood operations and is currently the most popular neighborhood process. In this algorithm, the error of the quantization process is computed and spatially redistributed or *diffused* within a local neighborhood in an effort to influence pixel quantization decisions within that neighborhood and thereby improve the overall quality of the halftoned image. Classical approaches to error diffusion, however, suffer from implementation constraints. In conventional *unidirectional* error diffusion, the algorithm raster scans the image, and for each pixel, a binary quantization decision is made based on the intensity of the individual pixel and the weighted error from pixels within a predefined diffusion region of previously

16-4

processed pixels. As a result of this unidirectional processing, the diffusion filter is necessarily causal and results in undesirable visual artifacts. The logical extension to the unidirectional error diffusion algorithm is a parallel implementation which provides symmetric error diffusion. Anastassiou [2] originally proposed an error diffusion neural network based on a correlation to the Hopfield neural network. However, convergence and stability issues in conjunction with implementation constraints limited the usefulness of this specific method.

The error diffusion neural network can be described as a matrix-vector extension to Figure 2(a). All state-variables are now represented as vectors and the feedback filter is now a 2-D interconnect and weighting matrix **W**. The energy function of the error diffusion neural network can shown to be

$$E(x, y) = (\mathbf{y} - \mathbf{x})^T \mathbf{A}(\mathbf{y} - \mathbf{x}) \tag{3}$$

where **A** is the matrix of interconnect weights derived from the feedback filter coefficients. It is clear from Equation (3) that as the error diffusion neural network converges and the energy function is minimized, so too is the error between the output and input images.

The novel approach to high-resolution photonic A/D conversion proposed here uses oversampling techniques, the error diffusion neural network, and a smart pixel hardware implementation[+]. Here, the input signal is first sampled at a rate higher than that required by the Nyquist criterion and then presented spatially as the input to a 2-D error diffusion neural network consisting of M × N neurons, each representing a pixel in the image space. The neural network processes the input oversampled analog image and produces an M × N pixel binary or halftoned output image. Decimation and low-pass filtering techniques, common to classical 1-D oversampling A/D converters, digitally sum and average M × N pixel output binary image using high-speed digital electronic circuitry. By employing a 2-D smart pixel neural approach to oversampling A/D conversion, each pixel constitutes a simple oversampling modulator thereby producing a distributed A/D architecture, shown in Figure 4. Spectral noise shaping across the array diffuses quantization error thereby improving overall SNR performance. Here, each quantizer within the network is embedded in a fully-connected, distributed mesh feedback loop which spectrally shapes the overall quantization noise thereby significantly reducing the effects of component mismatch typically associated with parallel or channelized A/D approaches. The 2-D neural array provides higher aggregate bit rates which can extend the useful bandwidth of photonic-based, oversampling A/D converters.
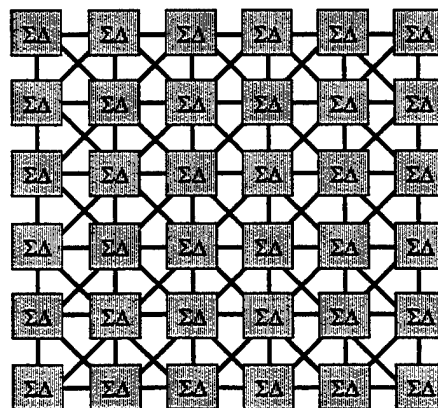

Figure 4. Fully-connected, distributed oversampling A/D converter architecture.

The performance of this distributed approach to A/D conversion can be described in several different ways. The SQNR for this architecture was given previously by Equation (2). The difference here is that the oversampling ratio is proportional to the output image size and therefore can be larger than classic oversampling ratios. Component mismatch effects can be quantified by considering the error diffusion neural network performance under these conditions. As an example, the effect of threshold mismatch across the array can be characterized as a modification to the neural network energy function according to

$$E = (\mathbf{y} - \mathbf{x})^T \mathbf{A}(\mathbf{y} - \mathbf{x}) + \varepsilon_t^T \mathbf{A}^{-1} \varepsilon_t - 2\varepsilon_t^T (\mathbf{y} - \mathbf{x}) \tag{4}$$

where ε is a vector containing the threshold mismatch of the array. This first term in Equation (4) is the same as in the original error diffusion neural network. The last two terms are contributions from threshold mismatch. We know that $\mathbf{A}^{-1} \leq 1$ and therefore $\varepsilon_t^T \mathbf{A}^{-1} \varepsilon_t$ is a scaled version of ε. We also know that $\mathbf{A}^{-1}$ has high-pass spectral characteristics and therefore spectrally-shapes any contributions from the threshold mismatch to higher frequencies. Equation (4) demonstrates that the contribution of the threshold mismatch to performance is spectrally-shaped by the error diffusion filter thereby reducing the overall impact. One specific realization of this new approach using a temporal-to-spatial converter and a smart pixel hardware realization is shown in Figure 5. Here, microlenses are used to convert the input sampled pulses to a 2-D spatial representation, distributing the signal over the detector array in the input plane in parallel.
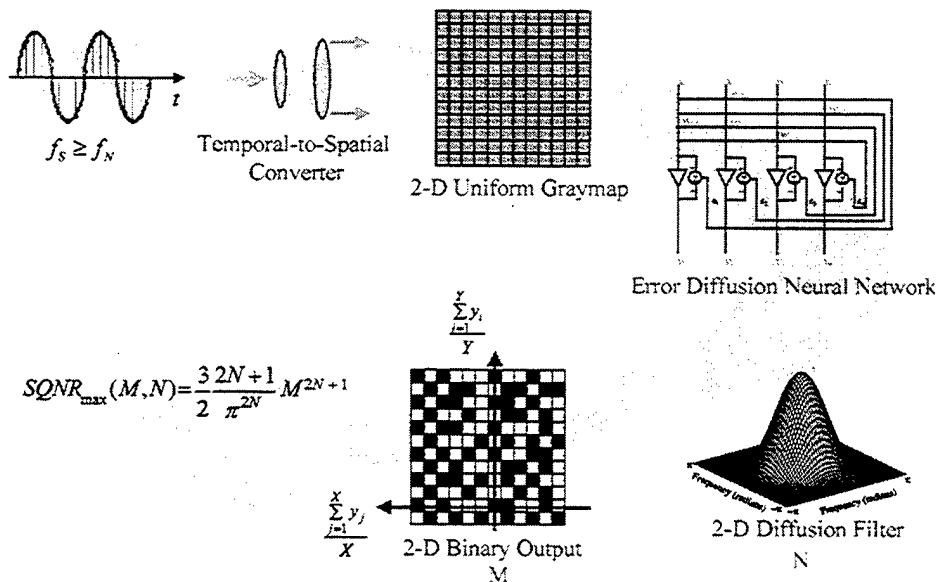

Figure 5. High-resolution photonic-based A/D converter using on 2-D space-time processing.

16-6

4 Summary and Observations

In this new approach to A/D conversion, each pixel constitutes a simple oversampling modulator thereby producing a distributed A/D architecture. Spectral noise shaping across the array diffuses quantization error thereby improving overall SNR performance. Here, each quantizer within the network is embedded in a fully-connected, distributed mesh feedback loop which spectrally shapes the overall quantization noise. This distributed approach to A/D conversion significantly reduces the effects of component mismatch typically associated with parallel or channelized A/D approaches. This 2-D neural approach provides higher aggregate bit rates which can extend the useful bandwidth of photonic-based, oversampling A/D converters.

References

1. R. Floyd and L. Steinberg, "An Adaptive Algorithm For Spatial Gray Scale," *SID 75 Digest,* vol. 36, 35-36, 1975.
2. D. Anastassiou, "Error diffusion coding for A/D conversion," *IEEE Trans. Circuits Syst.,* vol. 36, pp. 1175-1186, 1989.

Selected Publications and Conference Presentations

1. B. L. Shoop, *Photonic Analog-to-Digital Conversion,* Springer-Verlag (to be published in 2000).
2. B. L. Shoop, P. K. Das, E. K. Ressler, and T. J. Talty, "Photonic analog-to-digital conversion based on oversampling techniques," *Invited Paper* in *Proceedings of the SPIE,* vol. 4042, 2000 (*to appear*).
3. B. L. Shoop, "Photonic analog-to-digital conversion using oversampling techniques," *Invited Paper,* in *Proceedings of Optics '99,* (St. Petersburg, Russia), October 1999.
4. D. A. Hall, B. L. Shoop, R. W. Sadowski, A. H. Sayles, G. P. Dudevoir, D. M. Litynski, and P. K. Das, "Experimental results from a smart pixel implementation of the wavelet transformation for signal processing," *Proceedings of the SPIE,* vol. 3391, pp. 168-178, 1998.
5. B. L. Shoop, "Photonic analog-to-digital converters, " *Invited Paper* in *Proceedings of the. SPIE, vol.* 3490, pp. 252-255, 1998.

Cadet Publications and Presentations

1. CDT Zachariah G. Morford, "Decimation and low-pass filtering for high-resolution A/D conversion using VHDL," National Conference on Undergraduate Research, April 2000.

2. CDT Michael J. Sullivan Jr., "Two-dimensional filter design and analysis for an error diffusion neural network," National Conference on Undergraduate Research, April 2000.

Collaboration

1. Dr. Pankaj K. Das, University of California at San Diego
2. Dr. Daniel M. Litynski, University of Western Michigan

West Point Collaborators, Department of Electrical Engineering & Computer Science

1. LTC Eugene K. Ressler, Ph.D.
2. Dr. Timothy J. Talty
3. LTC Edward C. Shaffer, Ph.D.
4. LTC George Nowak, Ph.D.
5. Dr. Jean R. S. Blair
6. Dr. Thomas D. Wagner
7. LTC David A. Nash, Ph.D.
8. LTC Glen P. Dudevoir, Ph.D.

INTEGRATING PHOTONICS-RELATED ENGINEERING DESIGN IN THE DEPARTMENT OF ELECTRICAL ENGINEERING AND COMPUTER SCIENCE CURRICULUM

LTC BARRY L. SHOOP, LTC JOHN C. CARRANO, AND COL ANDRE H. SAYLES

Department of Electrical Engineering and Computer Science and Photonics Research Center
United States Military Academy, West Point, New York 10996
E-mail: Barry-Shoop@usma.edu

The Department of Electrical Engineering and Computer Science maintains a strong undergraduate research and engineering design component in both the electrical engineering and computer science curriculum. This includes actively integrating photonics-related projects into the capstone design experience and providing opportunities for advanced individual development courses in photonics-related subjects. This section describes this program and the projects which were conducted during the 1999 and 2000 Academic Years.

1 Introduction

Photonics technologies underpin many current and future communications, signal processing, and computational systems. The growing number of commercial and military applications of optics has been a driving force behind the evolution of the undergraduate optics program at the United States Military Academy. Military research and development programs have benefited from emphasis on technology transfer from commercial applications to military systems. Similarly, dual-use developments originating in the military sector have been of benefit to private industry. This common-use approach to military and commercial research and development has prompted USMA to implement an integrated education program in optics that is compatible with the focus of industry as well as the Army. This program includes laser familiarization for all 4000 students at West Point and more concentrated studies for a fairly large sample of physics, chemistry, and electrical engineering majors. The optical engineering education program is primarily based on conventional courses in applied optics, laser physics, and photonics engineering. However, the military sector must also focus on extending the same principles to weapon systems applications and soldier protection from radiation, and address such applications in the optics education process. This section discusses general photonics research and engineering education and accounts for electrical engineering and computer science student projects in the Photonics Research Center that are not tied directly to an existing experiment. Such projects are typically independent efforts that can be brought to closure within one or two semesters.

2 Supporting Curriculum

The U.S. Military Academy ensures graduates enter the Army with a balanced undergraduate education that develops basic knowledge in the sciences, engineering, and humanities. Students typically spend three semesters on required science and humanities courses before starting a majors program in a particular discipline. Cadets in an ABET-accredited engineering program take approximately 43 courses during a four-year or eight-semester enrollment. Thirty-one of those courses make up the required humanities, basic science, and engineering core curriculum, followed by twelve field courses which lead to the engineering major. The Academy keeps pace with the technological needs of the Army by requiring all graduates to take a series of at least five engineering courses within the core, regardless of

whether the student is majoring in mathematics, science, engineering, or the humanities. Typically, the five courses fall within a single engineering discipline, lead to an understanding of the engineering process, and culminate with a capstone design project.

The 43 course electrical engineering curriculum shown in Tables 1 and 2 includes the 26 common core courses necessary to produce well-rounded officers for military service, the five course electrical engineering core sequence, 12 additional courses necessary for competence in electrical engineering, and a one credit seminar which is not counted in the 43 courses and is primarily oriented towards exposing students to professional practice. The 12 field courses, seminar course, and the five course core engineering sequence provide a solid foundation in the discipline. The photonics engineering course, EE483, is usually taken during the final semester. The core courses, the breadth of electrical engineering, and a strict four year completion requirement dictate a program that is very carefully designed to meet both academy and accreditation requirements.

Freshman Year

Discrete Math	Differential Calculus
Chemistry	Chemistry
History	History
Psychology	Computer Science
English	English

Sophomore Year

Integral Calculus	Foreign Language
Physics	Physics
Foreign Language	EE365A
Economics	Political Science
Philosophy	Terrain Analysis
	MA364

Junior Year

English Literature	International Relations
Probability & Statistics	Leadership
EE302	EE363A
PH365	EE381
EE475	EE377
EM302	EM301

Senior Year

Military History	Military History
EE383	Law
EE407	EE408A
EE477	EE487A
EE471	EE483
	EE400A Seminar

Table 1. Typical electrical engineering program.

Required Courses:

EE302	Intro to Electrical Engineering I	EE483	Photonics Engineering
EE363A	Intro to Electronics	EE487A	Telecommunications
EE365A	Digital Computer Logic	EM301	Thermodynamics
EE377	Electric Power Engineering	EM302	Statics and Dynamics
EE381	Signals and Systems	PH365	Modern Physics
EE383	Electromagnetic Fields	MA364	Engineering Math
EE407	Electronic Design		
EE408	Analog Electronic System Design	**Elective Courses:**	
EE471	Automatic Control Systems	EE486	Solid State Electronics
EE475	Intro to Computer Architecture	EE488B	Microwave Engineering
EE477	Communications Systems	EE489	Advanced Individual Study

Table 2. Titles of electrical engineering courses.

The computer science curriculum is shown in Tables 3 and 4. The portion of this curriculum which has successfully integrated photonics-related projects is the computer information systems design courses. Through these courses, cadet teams have designed and built information systems which support the administration as well as the research and educational missions of the Center.

Table 3. Typical computer science program.

Freshman Year

Discrete Math	Differential Calculus
Chemistry	Chemistry
History	History
Psychology	Computer Science
English	English

Sophomore Year

Integral Calculus	Probability & Statistics
Physics	Physics
Foreign Language	Foreign Language
Economics	Terrain Analysis
Philosophy	Political Science
	CS360A

Junior Year

MA372	CS383
EE365	CS403
CS384	CS385
Leadership	CS380
English Literature	International Relations
Military History	Military History

Senior Year

CS481	CS478
CS393	CS408A
CS407A	CS476
CS474	Elective
Elective	Law
	CS400

Required Courses:

CS360A	Fundamentals of CS
CS380	Computer Organization
CS383	Information Systems
CS384	Data Structures
CS385	Data Str and Algo Analysis
CS393	Database Systems
CS400	Computer Science Seminar
CS403	Advanced Programming
CS407A	Computer Info Systems Design I
CS408A	Computer Info Systems Design II
CS474	Fundamentals of Comp Theory
CS476	Compiler Design
CS478	Analysis of Prog Languages
CS481	Operating Systems
EE365	Digital Computer Logic
MA372	Introduction to Discrete Math

Elective Courses:

CS473	Computer Graphics
CS482	Advanced Operating Systems
CS484	Computer Networks
CS485	Visiting Professor's Course
CS486	Artificial Intelligence
CS489	Advanced Individual Study
CS490	CS Summer Research Summer
EE484	Adv. Comp Arch. Using VHDL
EE487B	Designing w/Microprocessors

Table 4. Titles of computer science courses.

3   Advanced Individual Study

Undergraduate research opportunities in the Photonics Research Center are generally available to students who have received constructive credit (or validation) for one or more of the 26 core courses. Since every student at USMA must enroll in a minimum of five courses each semester, those who have received constructive credit for more than one course may fill out their schedule with individual research projects through the advanced individual study course, EE489. This process often leads to projects that extend over several semesters, with a course grade being awarded at the end of each semester. In the electrical engineering program, the better students are also permitted to work on an individual research project in lieu of one of the senior-level elective courses. Cadets desiring to substitute advanced individual study for a standard course must work with a faculty advisor to ensure that the project will provide the proper mix of engineering science and engineering design. Those who enroll in the advanced individual study course work under the direct tutelage of a faculty

member who provides extensive guidance, resources, and support. Because the students are at the undergraduate level, the faculty advisor often spends several hours per week discussing theoretical concepts and experimental procedures. The typical results are excellent and often comparable to master's level work. A major difference between undergraduate research and graduate research is the investment of time required of the faculty advisor.

4 Senior Design Program

Both the electrical engineering and the computer science senior design projects cover the entire sixteen week final semester of the program. Prior to the final semester, students are organized into design teams and required to prepare a proposal that delineates project requirements in technical terms and outlines an initial strategy for solving the design problem. Design teams include majors from a variety of disciplines. Additional design team members may include majors from other disciplines, such as engineering management, mechanical engineering, physics, or mathematics, who receive credit for design project contributions through a standard course in their discipline or an undergraduate research course.

Design problems are coordinated with department faculty and, where appropriate, outside organizations such as the Army Research Laboratory. Electrical engineering and computer science majors are first assigned to project teams based on a combination of student preferences for projects, student preferences for team members, and instructor recommendations. The target group size for each design team is four electrical engineering majors plus students from other disciplines as needed. Once all majors and sequence students have been assigned to a design team, a team leader is designated based on the best qualified volunteer for that position. Cadets who work in the PRC are required to produce a physical system, either hardware or software, that is based on interdisciplinary principles drawn from courses throughout the four-year curriculum.

Over the past two-years, 29 students have participated in photonics-related engineering design projects through either the electrical engineering or computer science curriculums.

5 Academic Individual Advanced Development

Every cadet must pursue a summer activity that goes beyond the academic, physical, or military baseline requirements. Most students pursuing academic development beyond the classroom select a program related to their discipline of study. The Department of Electrical Engineering and Computer Science offers summer research opportunities at various government and related organizations throughout the country, with the most popular locations being Army Research Laboratory facilities. Students who prefer to remain at the Academy during the summer can select research topics offered by the Photonics Research Center. Summer projects are usually three to five weeks and can be continued during the fall semester in lieu of an academic course if all other qualifications are met. A three-week summer research project at 40 hours minimum per week will require 120 student hours.

6 Specific Projects for Academic Years 1999 and 2000

Projects discussed as optics education topics do not typically fit into any of the existing PRC experiments, although the mechanisms for recruiting and evaluating students are the same. Over the past two years, several projects have been completed that fall into this educational program.

Electrical Engineering Projects

Design and Construction of a Portable Laser Light Show.

The goal of this project is to design and construct a laser light show, which interfaces a computer with an electro-opto-mechanical system. This system allows a user to draw simple figures on the computer screen using a graphical user interface (GUI) interface which are then converted to files which are used to control an external electro-opto-mechanical system, accurately positioning several laser beams. The resulting system displays the drawn figures as a laser light show. Three different lasers are used to provide color representation for the displayed images.

Free-Space Multiple Channel Two-Way Optical Communication Link.

The goal of this project was to develop a two-way optical communications link capable of multichannel operation in either digital or analog mode. At each end of the communications link are monolithically integrated laser and photodiode arrays. Each 4 × 4 array consists of a vertical cavity surface emitting laser (VCSEL) and metal-semiconductor-metal (MSM) photodiode at each pixel. Collimating optics were used to establish the end-to-end link. The cadet team was responsible for performing comprehensive electrical and optical characterization of the VCSEL and MSM arrays. The project has resulted in the successful demonstration of a single analog channel link, and the ability to digitally interface to the arrays in order to demonstrate the digital transfer of information across the link. The cadet team is also working toward establishing a multiple channel link.

Computer Science Projects

CGSC Distance Learning Project.

The purpose of this project is to develop a distance learning capability to supplement and enhance the existing PRC short-course taught to students at the Command and General Staff Officer Course, Ft. Leavenworth, KS. The intent is to provide course material, including pre-tests, quizzes, post-tests, as well as all of the necessary instructional material in an on-line format. If successful, this could provide the mechanism to expand the influence of this particular course throughout the Army.

Qualitative Analysis of Halftone Image Quality Using the Internet.

This project is intended to provide support of the digital image halftoning research project by providing an automated method by which halftone image quality can be assessed over the internet. In the digital halftoning research project, we are developing a new method by which to halftone images which we believe to provide superior quality halftone images. One method of evaluating halftone image quality is to present various images halftoned by different algorithms to a population who then vote on what they believe to be the best images. This project will investigate the feasibility of conducting this through a web-based mechanism and develop the necessary software to present a series of halftoned images and collect data on the subject's preferences. This information is then compiled to provide a qualitative assessment of the performance of the digital halftoning algorithms being produced by researchers in the PRC.

A Financial Database and Accounting System for the PRC.

This project updated an existing financial accounting system which supported the financial management of the PRC budget. Under the previous system, which was developed by a PRC researcher in the mid-1980's, an antiquated, DOS-based database was used to manage the purchasing and fiscal records for the PRC. The updated accounting system was developed as a Microsoft Access-based program which provides the capability to more easily manage and provide oversight to the PRC resources.

Web-Based Publications Database

The goal of this project was to establish a web-based database for all scholarly research publications authored by members of the Photonics Research Center, and the Department of Electrical Engineering and Computer Science. The actual database was created using Sybase and Cold Fusion. The Web application consists of several pages that present historical data on research publications categorized in a variety of convenient formats. For example, an individual can access the Web page and choose to see a summary page that indicates total numbers of papers authored, during a given time period, categorized by type of publications (such as a journal paper or an invited conference presentation). In addition, one can view the publications of any given faculty member. Access is also provided for electronic copies of the actual publications. A search feature is included to allow for individuals accessing the database to quickly obtained desire information. In order to keep the database current, a very simple user input page is provided that allows new publications to be quickly added to the database by the author with minimal effort.

7 Observations and Future Directions

At this time, the optics education program in the Department of Electrical Engineering and Computer Science is a well-established program. The current program will continue to be expanded to involve more students and more projects.

References

Academic Program (Redbook) AY1996-1997, United States Military Academy (West Point, NY), August 1996.

Cadet Involvement:

Class of 1999

EE408, Spring 1999 *Portable Laser Light Show.*
      Cadet Andrew Jaskolski
      Cadet James L. Krueger
      Cadet Jason Mallory
      Cadet McRae Collins

CS407, Spring 1999, *A Financial Database and Accounting System for the PRC.*

Cadet David L. McLaughlin
Cadet Matthew Hargrove
Cadet Andrew Foss
Cadet Matthew Birck

Class of 2000

EE408, Spring 2000 *Portable Laser Light Show.*
Cadet Malaika Crowe
Cadet Robert Gillespie
Cadet Sean Barbaras
Cadet Mathhew Frosch
Cadet Christopher Morrell
Cadet Bort Bryson

EE408, Spring 2000 *Free-Space Multiple Channel Two-Way Optical Communication Link.*
CDT Jesse Altuna
CDT Eric Sigmon
CDT Jackson Huang

CS408, Spring 2000, *CGSC Distance Learning Project*
Cadet Clindon Phillips
Cadet Jonathan Ritz
Cadet Joseph Tyron
Cadet Bronston Clough

CS408, Spring 2000, *Qualitative Analysis of Halftone Image Quality Using the Internet.*
Cadet Patrick Sagebiel
Cadet Alexander Schneider
Cadet Allen Thompson
Cadet Andrew Whitford

CS408, Spring 2000, Web-Based Publications Database.
Cadet Brian Pearson
Cadet Jennifer McMinn
Cadet Nicholas Rengel
Cadet Thomas Stewart